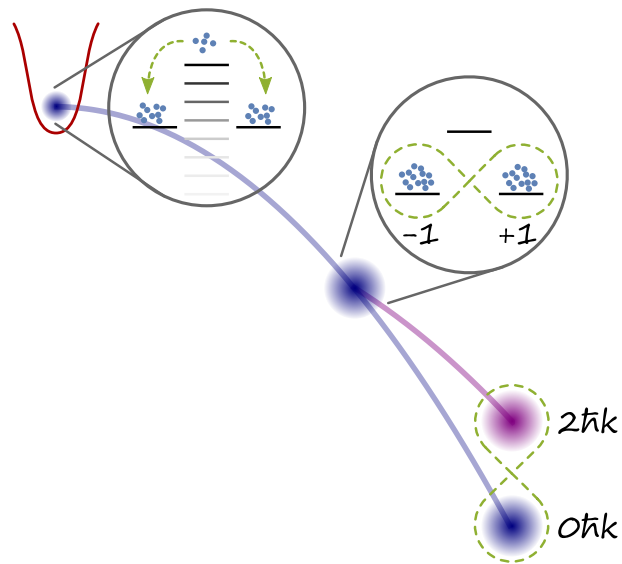


# ENTANGLED MOMENTUM MODES FOR ATOM INTERFEROMETRY



Von der QUEST-Leibniz-Forschungsschule der  
Gottfried Wilhelm Leibniz Universität Hannover

zur Erlangung des Grades

Doktor der Naturwissenschaften  
- Dr. rer. nat.-

genehmigte Dissertation von

**M.Sc. Fabian Anders**

2022

REFERENT

apl. Prof. Dr. Carsten Klempt  
Institut für Quantenoptik  
Leibniz Universität Hannover

KOREFERENT

Prof. Dr. Ernst M. Rasel  
Institut für Quantenoptik  
Leibniz Universität Hannover

KOREFERENT

Prof. Dr. Augusto Smerzi  
QSTAR, INO-CNR and LENS  
Firenze

TAG DER PROMOTION: 15. Juni 2022

Fabian Anders: *Entangled momentum modes*  
for atom interferometry, PHD Thesis, Leibniz Universität Hannover  
© 2022

## ABSTRACT

---

Entangled ensembles have been created in versatile atomic systems and find a promising application in entanglement-enhanced metrology. Here, entangled spin-states have been successfully applied within interferometers that allow to measure magnetic fields and frequencies with enhanced sensitivities. In contrast, atom interferometers for the measurement of inertial forces and gravitational fields are operated in external degrees of freedom and span an area in space-time. To make use of entangled states here, the entanglement has to be generated among momentum modes with suitable spatial extent and velocity width.

In this thesis, a source of momentum-entangled atoms that is compatible with present-day light-pulse atom interferometers is presented. Utilising a quasi-adiabatic ramp through a quantum phase transition, highly-entangled twin-Fock states are created in the internal spin-degree of freedom of a  $^{87}\text{Rb}$  Bose-Einstein condensate. Hereon, the entanglement is successfully transferred to distinct momentum-modes by a stimulated Raman coupling and verified by the direct measurement of an entanglement criterion. The observed mode quality and the residual expansion demonstrate that this entangled source is well-suited to the successive application in light-pulse atom interferometers and opens up a path to gravimetry beyond the standard quantum limit. Furthermore could the demonstrated techniques be employed to realise a scalable atomic Bell test. In the long run, similar entangled sources could specifically enhance the performance of gravity gradiometers, tests of the Einstein Equivalence Principle and future atomic gravitational wave detectors.

**KEYWORDS:** Bose-Einstein condensate, spin-changing collisions, twin-Fock state, entanglement, momentum-entanglement, atom interferometry, Raman coupling, Bell test

## ZUSAMMENFASSUNG

---

Verschränkte Zustände wurden in vielen atomaren Systemen erzeugt und finden eine aussichtsreiche Anwendung in der verschränkungsgestützten Metrologie. Hier wurden verschränkte Spinzustände erfolgreich in Interferometern eingesetzt, mit denen Magnetfelder und Frequenzen mit erhöhter Empfindlichkeit gemessen werden können. Im Gegensatz dazu werden Atominterferometer zur Messung von Beschleunigungen und Gravitationsfeldern in externen Freiheitsgraden betrieben und spannen eine Fläche in der Raumzeit auf. Um hier verschränkte Zustände nutzen zu können, muss die Verschränkung zwischen Impulszuständen mit geeigneter räumlicher Ausdehnung und Geschwindigkeitsbreite erzeugt werden.

In dieser Arbeit wird eine Quelle für impulsverschränkte Atome vorgestellt, die mit heutigen Atominterferometern kompatibel ist. Unter Verwendung einer quasi-adiabatischen Rampe durch einen Quantenphasenübergang werden hochverschränkte Zwillings-Fock-Zustände im inneren Spin-Freiheitsgrad eines  $^{87}\text{Rb}$  Bose-Einstein-Kondensats erzeugt. Die Verschränkung wird durch eine stimulierte Raman-Kopplung erfolgreich in den Impulsraum übertragen und durch die direkte Messung eines Verschränkungskriteriums verifiziert. Die beobachtete Modenqualität und die Restexpansion zeigen, dass sich diese verschränkte Quelle gut für die sukzessive Anwendung in Atominterferometern eignet und einen Weg zur Gravimetrie jenseits des Standard-Quantenlimits eröffnet. Darüber hinaus könnten die aufgezeigten Techniken zur Durchführung eines skalierbaren atomaren Bell Tests eingesetzt werden. Langfristig könnten ähnliche verschränkte Quellen insbesondere die Leistung von Gravitationsgradiometern, Tests des Einsteinschen Äquivalenzprinzips und zukünftigen atomaren Gravitationswellendetektoren verbessern.

SCHLAGWÖRTER: Bose-Einstein Kondensat, spinverändernde Stöße, Zwillings-Fock Zustand, Verschränkung, Impulsverschränkung, Atominterferometrie, Raman-Kopplung, Bell Test

# CONTENTS

---

1	INTRODUCTION	1
2	FUNDAMENTAL CONCEPTS AND STATE-OF-THE-ART EXPERIMENTS	5
2.1	Entanglement-enhanced interferometry	5
2.1.1	Collective qubits and visualisation on the Bloch sphere	5
2.1.2	Shot noise, the standard quantum limit and beyond	8
2.1.3	Number squeezing and useful entanglement	13
2.2	Entanglement in cold atom experiments	16
2.2.1	Realisations in spin space	16
2.2.2	Entanglement in external degrees of freedom	18
2.2.3	First steps and proposed routes towards entanglement-enhanced inertial sensing	18
3	SPINOR BOSE-EINSTEIN CONDENSATE	21
3.1	Our apparatus in a nutshell	21
3.2	Manipulating hyperfine levels	25
3.3	Spin dynamics	28
3.4	One Hamiltonian, various types of entangled states	30
3.4.1	Twin-Fock states	30
3.4.2	Spin-1 Dicke States	32
3.4.3	Squeezed states	32
3.4.4	Further applications in state engineering	34
4	PRECISE CONTROL OF SPIN DYNAMICS FOR THE GENERATION OF TWIN-FOCK STATES	37
4.1	Calibration of the effective quadratic Zeeman shift	37
4.2	Determining the spin-dynamics rate	39
4.3	Preparation of twin-Fock states by a quasi-adiabatic q-ramp	42
5	TRANSFER TO DISTINCT MOMENTUM MODES	47
5.1	Raman transfer	47
5.1.1	Optical setup	50
5.1.2	Differential AC-Stark shift	53
5.1.3	Shaped pulses	54
5.2	Collimation of atomic clouds, transfer efficiency and detection noise	57
5.3	Preparing entangled momentum modes	62
6	DISCUSSION AND OUTLOOK	69
6.1	Refining the entangled source	69
6.2	Towards entanglement-enhanced gravimetry	72
6.3	Sketch of a scalable atomic Bell test	77
A	APPENDIX	81

- A.1 Details on envisioned protocols 81
  - A.1.1 Alternative implementation of the gravimeter 81
  - A.1.2 Detailed protocol of the sketched Bell test 81
- A.2 Auxillary measurements 82
  - A.2.1 Effective quadratic Zeeman shift vs. set voltage 82
  - A.2.2 Detection noise vs. measured cloud size 84
- A.3 Details on simulations and calculations 85
  - A.3.1 Definition of the Wigner function on the Bloch sphere 85
  - A.3.2 Numerical simulation of spin dynamics 85
  - A.3.3 Calculating the AC-Stark shift 86
  - A.3.4 Velocity selection of Raman transfers 88

BIBLIOGRAPHY 91

## LIST OF FIGURES

---

Figure 1.1	Comparison of realised momentum-entangled states.	3
Figure 2.1	Schematic two-mode interferometer.	6
Figure 2.2	Many-body Bloch sphere.	7
Figure 2.3	Noisy interferometer signal.	10
Figure 2.4	Entangled states on the generalised Bloch sphere.	12
Figure 2.5	Number squeezing and spin length for different entanglement structures.	14
Figure 2.6	Metrological gain of pairwise entangled mixture.	16
Figure 3.1	Sketch of the experimental setup.	23
Figure 3.2	Sketch of hyperfine levels, couplings and spin dynamics.	26
Figure 3.3	Twin-Fock states by a rapid quench of $q$ .	31
Figure 4.1	Calibration of the effective $q$ .	38
Figure 4.2	Determining the spin-dynamics rate $\Omega$ .	40
Figure 4.3	Extracting $\Omega$ from a resonance scan.	41
Figure 4.4	Many-body ground state and energy gap.	43
Figure 4.5	Results of the implemented quasi-adiabatic $q$ ramp.	45
Figure 5.1	Sketch of the Raman coupling.	48
Figure 5.2	Co- and counter-propagating Raman transfers.	49
Figure 5.3	Optics and geometry of the Raman laser setup.	52
Figure 5.4	Differential AC-Stark shift.	54
Figure 5.5	Temporally shaped pulses.	55
Figure 5.6	Spectroscopy and Rabi measurement of the Raman transfer.	56
Figure 5.7	Expansion rates and trajectories of free-falling ensembles.	58
Figure 5.8	Detection noise for free-falling ensembles.	60
Figure 5.9	Setting and results of the implemented Raman transfer.	61
Figure 5.10	Predicted selectivity of the Raman transfer.	62
Figure 5.11	Sketch of the main idea.	63
Figure 5.12	Protocol to transfer twin-Fock states to distinct momentum modes.	64
Figure 5.13	Trajectories, expansion and absorption images of free-falling atomic clouds.	65
Figure 5.14	Realisation of entangled momentum modes suitable for atom interferometry.	66

Figure 6.1	Spin length as measure of the spatial fidelity of matter-waves.	71
Figure 6.2	Envisaged twin-Fock gravimeter.	74
Figure 6.3	Sketch of a Bell test.	78
Figure A.1	Detailed sketch of a Bell test.	83
Figure A.2	MW dressing power vs. voltage.	83
Figure A.3	Detection noise vs. mask size.	84
Figure A.4	Raman laser frequencies within the spectrum of Rubidium.	88

## ACRONYMS

---

BEC	Bose-Einstein condensate
SQL	standard quantum limit
MOT	magneto-optical trap
SMA	single-mode approximation
PBS	polarizing beam splitter
MW	microwave frequency
RF	radio frequency
EM	electromagnetic
RWA	rotating-wave approximation
OAT	one-axis twisting
TACT	two-axis countertwisting
FI	Fisher information
QFI	quantum Fisher information
CSS	coherent spin-state
QPT	quantum phase transition
AOM	acousto-optic modulator



## INTRODUCTION

---

Within the last century, the perception of entanglement matured from a disturbing artefact of quantum theory to a core recourse in quantum technology.

In 1935, physicist Erwin Schrödinger placed a cat into a steel box, together with a flask of poison that would be destroyed upon the random decay of a radioactive atom. As quantum mechanics does not predict the exact time of the decay, but only the chance for the decay to happen after some time, the quantum state of the combined atom-cat system would at some point describe the cat as dead and alive simultaneously. With this, as he said "burlesque" , gedankenexperiment, Schrödinger wanted to express what prevented him from accepting quantum mechanics to be an image of reality [1]. To this end, he actually constructed what later would be called an entangled state between the atom and the cat. In the same year, Einstein, Podolsky and Rosen (EPR) expressed a similar view on quantum theory in their famous paper titled "Can Quantum-Mechanical Description of Physical Reality be Considered Complete?" [2]. Here, they constructed a state of two entangled particles with correlated momentum and position. Given this state, the measurement of either momentum or position at one particle allows to predict with certainty the momentum or position of the other particle, i. e. the state of the untouched particle would change instantaneously upon the choice of the distant measurement. As such nonlocal effects are excluded by special relativity, argued Einstein, the actual state of the untouched particle cannot depend on the chosen measurement and thus the constructed quantum state cannot correspond to a state of reality. Therefore, quantum mechanics was regarded to be incomplete and only a proxy of an underlying theory that resolves the vagueness using so far hidden variables. In 1964, John Stewart Bell refined the state and the measurement envisaged by EPR and showed that the outcome predicted by quantum mechanics differs from the prediction of any classical hidden variable theory assuming locality and realism [3]. Thereby, the possibility of such an underlying classical theory became verifiable by conducting experiments — and has been experimentally negated since then [4–6]. This tells us that the world as we find it on the microscopic scale cannot obey locality and realism, but which of both assumptions fails, or if even both need to be dropped, remains unknown [7].

Moreover, entanglement seems not only to be a feature of some uncommon states, but also an omnipresent process. Entanglement between subsystems has been shown to drive thermalisation and clas-

sical dynamics on the level of the subsystems, i. e. a measurement of the subsystem reveals classical outcomes, whereas on the global scale, the system becomes more entangled [8, 9]. As we commonly observe some sort of subsystem, interacting with a larger environment which is not controlled or monitored completely (particularly true for macroscopic objects), we usually find states that characterise as classical while being invisibly entangled with the environment (known as decoherence). Hence, observing entanglement demands a well-isolated system, such that the entanglement of a specifically prepared state remains within the observable system and decoherence is suppressed.

As photons have less possibilities to interact with their environment compared to atoms, they were the natural system for first experimental observations of non-classical states [10, 11]. At this time, light interferometers have been around for nearly a century [12] and advanced towards the realm where the quantum properties of the probe state, i. e. the light that is sent through the interferometer, became relevant for possible limitations in precision [13]. The possibility to squeeze the quantum noise inherent to the probe state using correlated photons was formulated in 1981 [14] and was realised experimentally within the same decade [15, 16]. Since then, the so far insurmountable standard quantum limit (SQL) was overcome by using squeezed states in many optical interferometers, most prominently in the current gravitational wave detectors [17]. The necessity of entanglement for interferometry beyond the SQL was shown later in Ref. [18] and established the class of metrological useful entanglement.

The idea to prepare squeezed states in many-body atomic systems to enhance atom interferometric measurements formed in the early 1990s [19, 20]. It took nearly 20 years for the first spin-squeezed state to be prepared [21, 22] and to finally be applied to enhance the sensitivity of an interferometer [23, 24]. Since then, different types of many-body entangled states followed in Bose-Einstein condensates (BECs) as well as cold thermal clouds [25]. For the majority of realised states, the entanglement has been established among spin states, which allows for a metrological enhancement for magnetometers [26] or for atomic clocks [27, 28].

Also in the early 1990s the field of atom interferometry emerged, where similarly to the light beam in an optical interferometer, atoms should travel on distinct paths and recombine again for interference. The motivation to replace photons by atoms is the fundamental sensitivity enhancement due to the relatively small de Broglie wavelength associated with massive atoms. Furthermore, the mass ensures a natural ability to sense gravity and inertial forces. Different techniques have been realised simultaneously within one year: Atomic beams have been spatially split and recombined by deflection on microfabricated matter gratings [29] and double slit configurations [30] (later on also by deflec-

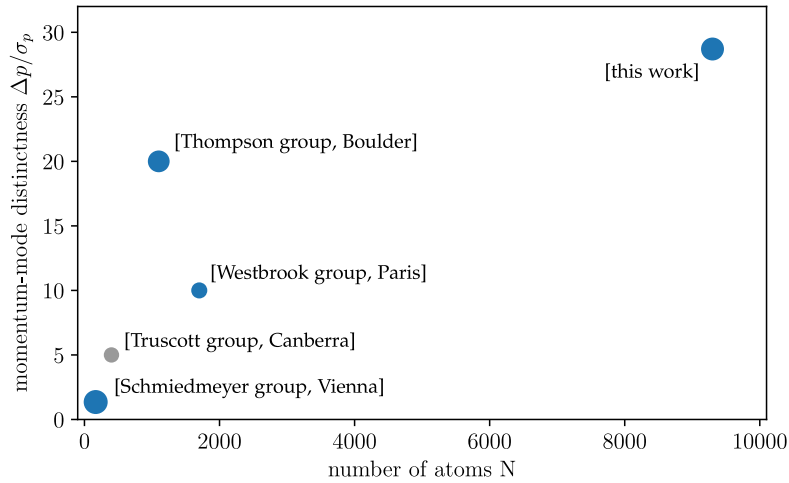


Figure 1.1: Comparison of realised momentum-entangled states regarding the ensemble size and the distinctness of the momentum modes, both relevant quantities for the application in interferometry. The size of the blue markers represents the inverse of the directly observed reduction of quantum fluctuations (number squeezing). In case of a grey marker, a value for the reduced fluctuations was not reported. Notable additional qualities are detected Bell correlations (Truscott group) and directly measured metrological gain (Thompson group). The graph is based on data reported in [41] (Schmiedmeyer), [42–44] (Westbrook), [45, 46] (Truscott), [47] (this work) and [48] (Thompson).

tion on standing light waves [31]). The photon recoil during the optical transition in Ramsey spectroscopy has been utilized to implement an atom interferometer that measures the Sagnac effect [32]. The first atom interferometer where atoms from a cold thermal ensemble are coherently separated and recombined by stimulated two-photon Raman transitions has been reported in the same year as well [33]. Based on this principle, many light-pulse atom interferometers followed and demonstrated the precise measurement of accelerations [34], Earth’s rotation and gravitational acceleration [35–37], gravity gradients [38] and the gravitational constant [39]. Naturally, it is desirable to operate such atom interferometers also with a sensitivity beyond the SQL, as it is possible in optical interferometry. Momentum-entangled ensembles, as required to provide a resource of metrological useful entanglement for this field, present a long-standing challenge [40].

So far realised momentum-entangled states are depicted in Figure 1.1. The results are compared regarding two relevant quantities for the application in atom interferometry. The ensemble size, as it determines the SQL-limited sensitivity to start with, and the distinctness of the momentum modes given by the mean momentum difference of the modes  $\Delta p$  in proportion to the momentum spread of each mode  $\sigma_p$ . A large momentum difference is beneficial to increase the absolute

phase signal for a given evolution time. The momentum spread determines for example the momentum transfer efficiencies and maximally feasible free-fall times. The physical systems employed to prepare momentum-entanglement are quite diverse. In the Schmiedmeyer group, BECs are used to provide correlated momentum pairs from collisional de-excitation of an excited trap mode. Two colliding BECs are the source for scattered atoms with correlated and Bell correlated momentum in the Westbrook and the Truscott group. In the Thompson group, a cavity-based atom-light interaction is employed to prepare an entangled thermal ensemble which is then partially accelerated by Raman light pulses and traverses a full interferometer within the cavity.

The momentum-entangled source presented in this work aims to demonstrate a viable path to provide useful entanglement for today's high-precision atom interferometers. Here, entanglement is generated in the spin-degree of freedom of a  $^{87}\text{Rb}$  BEC by spin-changing collisions. To prepare a major fraction of the ensemble in the entangled state, a quasi-adiabatic parameter ramp over a quantum phase transition (QPT) is employed. Thereon, the ensemble is released to free-fall and coherently transferred to distinct momentum modes by a stimulated Raman transition. The momentum separation of the entangled modes is a factor of 29(3) larger than the residual expansion of the ensemble, allowing for complete spatial separation within a few milliseconds of free fall, where the atomic clouds show a number squeezing of  $-3.9(6)$  dB beyond shot-noise. The measurement of a conjugate observable allows to infer a generalised squeezing parameter of  $-1.9(7)$  dB, which constitutes a direct proof of entanglement between the two momentum modes.

This thesis is organised as follows: In chapter 2, some basic theoretical concepts of entanglement-enhanced interferometry are presented and the experimental achievements in this field are discussed. In chapter 3, the apparatus and physical system of a spinor Bose-Einstein condensate is briefly introduced and the various entangled states that can be generated by spin dynamics are presented. How to precisely control spin dynamics is discussed in chapter 4, and applied to generate a large fraction of the condensate in an entangled spin-state. In the main part, chapter 5, the techniques implemented to realise a highly efficient transfer of photon momenta to the atoms are presented and applied to an entangled spin-state which then proves to be entangled in momentum space. The possible improvements of the presented entangled source are discussed in chapter 6. Based on the techniques utilised in this work, a possible extension to an entanglement-enhanced measurement of gravity is presented and a scalable atomic Bell test is sketched.

## FUNDAMENTAL CONCEPTS AND STATE-OF-THE-ART EXPERIMENTS

---

In this chapter, the basic theoretical concepts of entangled ensembles and their application in interferometry are introduced. A focus lies on the key features of a specific type of entangled states, the twin-Fock states. In addition, recent experimental achievements in cold atom experiments are summarised, focussing on the generation of entanglement in internal and external degrees of freedom, already realised entanglement-enhanced interferometers and finally the proposed routes towards the application of entanglement in inertial sensors.

### 2.1 ENTANGLEMENT-ENHANCED INTERFEROMETRY

A common interferometer employs two modes which can be coupled but otherwise evolve independently and can accumulate a relative phase. Whether the modes are realised by the photons in two laser paths of an optical interferometer or by atoms populating two different states in an atom interferometer is conceptually equivalent. Each particle traversing the interferometer can be described as a simple two-state quantum system — a qubit. In contrast to experiments working on the actual realisation of high-fidelity single qubits, in our system the many qubits are indistinguishable and cannot be individually addressed. Any manipulation is applied to an entire ensemble of qubits. These many-body states are best described in the occupation number representation, where the indistinguishability is incorporated and the particles statistics (bosonic or fermionic) is reflected in the commutation relation of annihilation and creation operators.

#### 2.1.1 *Collective qubits and visualisation on the Bloch sphere*

A single qubit  $\alpha |a\rangle + \beta |b\rangle$  may describe a single atom in a superposition of state  $|a\rangle$  and state  $|b\rangle$ . When measured, the atom would be found with a probability of  $|\alpha|^2$  in state  $|a\rangle$  and with  $|\beta|^2$  in state  $|b\rangle$ . The state can be visualised as a point on the surface of the well-

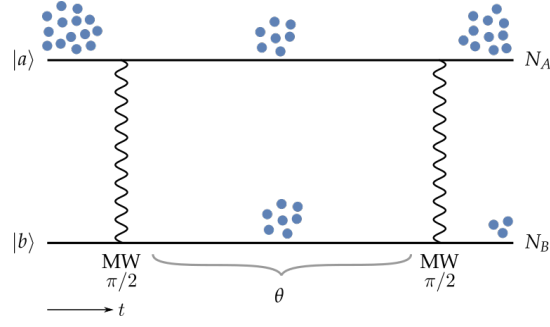


Figure 2.1: Depiction of a schematic two-mode interferometer. Here, all atoms initially populate mode  $a$ . A  $\pi/2$ -coupling, e.g. a microwave pulse, prepares the atoms in a 50/50 superposition of both modes and enables the accumulation of a relative phase  $\theta$ . The second  $\pi/2$ -coupling translates the relative phase shift into a population imbalance of the two modes. Finally, the number of atoms in each mode is counted and the phase shift estimated from the number difference  $N_- = N_A - N_B$ .

known three dimensional Bloch sphere. The axes that span this three-dimensional state space are given by

$$s_x = \frac{1}{2} (|b\rangle \langle a| + |a\rangle \langle b|) \quad (2.1)$$

$$s_y = \frac{1}{2i} (|b\rangle \langle a| - |a\rangle \langle b|) \quad (2.2)$$

$$s_z = \frac{1}{2} (|a\rangle \langle a| - |b\rangle \langle b|). \quad (2.3)$$

These operators are proportional to the Pauli matrices and satisfy the SU(2) spin algebra  $[s_l, s_m] = i\epsilon_{lmn}s_n$ . Since the states  $|a\rangle$  and  $|b\rangle$  do not necessarily represent a spin-1/2 system, one speaks about pseudo-spins here.

We can extend this description to a collection of  $N$  indistinguishable qubits by summing up the individual pseudo-spins and applying the formalism of second quantisation. The resulting operators

$$J_x = \sum_{i=1}^N s_x^{(i)} = \frac{a^\dagger b + b^\dagger a}{2} \quad (2.4)$$

$$J_y = \sum_{i=1}^N s_y^{(i)} = \frac{a^\dagger b - b^\dagger a}{2i} \quad (2.5)$$

$$J_z = \sum_{i=1}^N s_z^{(i)} = \frac{a^\dagger a - b^\dagger b}{2} \quad (2.6)$$

are expressed in terms of bosonic annihilation and creation operators and constitute a collective pseudo-spin  $\mathbf{J} = (J_x, J_y, J_z)$ , since the collective operators inherit the above commutation relation

$$[J_l, J_m] = i\epsilon_{lmn}J_n. \quad (2.7)$$

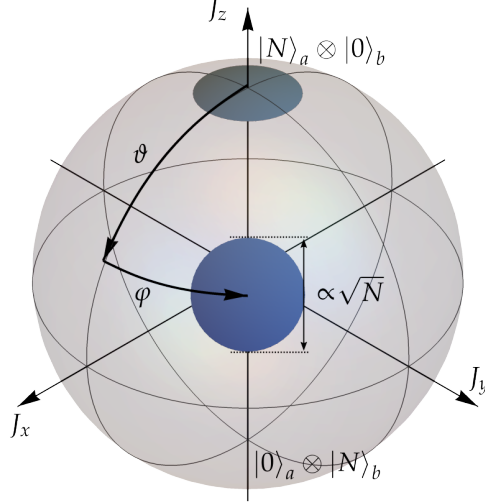


Figure 2.2: The many-body Bloch sphere. A coherent spin-state (CSS) of  $N$  pseudo-spins visualised on the generalised Bloch sphere with radius  $N/2$ . The width of the circle is connected to shot-noise and a projection onto the  $J_z$  axis gives the expected distribution of outcomes for a measurement of the population difference  $2J_z = N_A - N_B$ . The shape of the distribution characterising the state is retained under simple rotations, as for example due to an interferometric sequence.

For completeness, we also note that the identity  $s_0 = |a\rangle\langle a| + |b\rangle\langle b|$  becomes the operator of the total atom number

$$\hat{N} = \sum_{i=1}^N s_0^{(i)} = a^\dagger a + b^\dagger b, \quad (2.8)$$

and the conservation of probability  $\langle s_0 \rangle = |\alpha|^2 + |\beta|^2 = 1$  thereby corresponds to the conservation of the total atom number  $\langle \hat{N} \rangle = \sum_{i=1}^N 1 = N$ .

A state of indistinguishable qubits can be visualised on the surface of a Bloch sphere (see Figure 2.2), very similar to a single qubit. The basic operations that build up a two-mode interferometer as schematically shown in Figure 2.1, constitute rotations of the state on the Bloch sphere. Opening the interferometer by the generation of a 50/50 superposition of the modes  $a$  and  $b$  results in a  $\pi/2$ -rotation onto the equator, let's say around  $J_x$ . A subsequent acquirement of a relative phase rotates the state by  $\theta$  around the  $J_z$  axis. The two modes of the interferometer are chosen such that the relative phase depends on the quantity of interest, e. g. a magnetic field or a coupling frequency. Finally, the interferometer is closed by another  $\pi/2$ -rotation around the  $J_x$  axis. In total, the interferometer describes a rotation by  $\theta$  around the  $J_y$  axis.

At the north and south pole we find the states with all atoms in mode  $a$   $|N\rangle_a \otimes |0\rangle_b$  and all atoms in mode  $b$   $|0\rangle_a \otimes |N\rangle_b$ , respectively.

Superpositions with a 50/50 mean population of the modes are situated on the equator. A general coherent spin-state (CSS) can be attained by rotating the polarised state at the north pole  $|N, 0\rangle$  by  $\vartheta$  around the  $J_y$  axis and then by  $\varphi$  around the  $J_z$  axis

$$|\varphi, \vartheta, N\rangle_{\text{CSS}} = e^{-i\vartheta J_y} e^{-i\varphi J_z} |N, 0\rangle. \quad (2.9)$$

The fluctuations of these states in the plane orthogonal to their mean spin direction represent the minimal fluctuations that can be reached with uncorrelated atoms. As a consequence of the commutation relation in Equation 2.7, the standard deviation of orthogonal spin components obey the uncertainty relation

$$\Delta J_x \Delta J_y \geq \frac{1}{2} |\langle J_z \rangle| \quad (2.10)$$

where the bound on the right hand side evaluates to  $N/4$  for all CSS' because  $|\langle J_n \rangle|$  equals the radius  $N/2$  of the sphere. The fluctuations are equally distributed and easy to compute exemplarily in the  $J_x$ - $J_y$  plane for the state  $|N, 0\rangle$ , where

$$\Delta J_x = \Delta J_y = \sqrt{\langle J_y^2 \rangle} = \sqrt{N}/2. \quad (2.11)$$

Simply rotating the state according to Equation 2.9 does not change the fluctuations, therefore all CSS' saturate the uncertainty relation and are best visualised by a circle with a radius of  $\propto \sqrt{N}/2$ .

### 2.1.2 Shot noise, the standard quantum limit and beyond

A common observable at the end of an interferometer sequence is the number difference  $N_- = N_A - N_B$ . Quantum mechanics only predicts the probability distribution of outcomes for this observable. As it is the case for all stochastic processes, the outcome of a single measurement is not certain. If  $N$  independent atoms are employed, the outcome inherently fluctuates with the so-called shot-noise  $\sqrt{N}$  around the mean (for a 50/50 distribution). These quantum fluctuations impose a limit on the achievable precision in estimating the phase shift — the standard quantum limit (SQL). This limit can only be overcome by employing entangled states [18], i.e. many-particle states with quantum-mechanical inter-particle correlations. These non-classical correlations can affect the probability distribution of the measured outcomes of the interferometer in a way that the phase estimation is enhanced beyond the SQL and the physical quantity that is encoded in the phase shift, such as a magnetic field strength or an acceleration, can be measured more precisely.

Formally, an interferometer imprints a phase shift  $\theta$  onto an input state  $|\psi\rangle_{\text{in}} \rightarrow |\psi(\theta)\rangle$ . The observable  $M$  describing the measurement on the output state can be chosen at will and leads to a single



measurement outcome. Repeating the same measurement  $\nu$  times gives us a set of outcomes  $\mathbf{x} = \{x_1, x_2, \dots, x_\nu\}$ . We can predict the underlying probability distribution  $p_x(\theta) = \langle \psi(\theta) | x \rangle \langle x | \psi(\theta) \rangle$  where  $|x\rangle \langle x|$  is a projector onto all states that give the outcome  $x$  when measured by  $M$  (we can choose an arbitrary basis here). The whole set of projectors is given by the spectral decomposition  $M = \sum_x x |x\rangle \langle x|$ . As an example, we can write the population imbalance in terms of two-mode Fock states  $|N-x, x\rangle = |N-x\rangle_A \otimes |x\rangle_B$  and  $x = 0, 1, \dots, N-1, N$  as

$$N_A - N_B = \sum_x (N-x) |N-x, x\rangle \langle N-x, x|,$$

which determines the probability for each population imbalance  $p(\theta)_{N-x} = \langle \psi | N-x, x \rangle \langle N-x, x | \psi \rangle$  in the range  $N, N-1, \dots, -(N-1), -N$ .

In the experiment, full knowledge of the probability distribution would be ideal to estimate the phase shift. However, as experiments provide a limited set of outcomes, it is usually not feasible to fully reconstruct the underlying probability distribution and therefore global properties such as the mean

$$\langle M \rangle = \sum_x x p(x) \quad (2.12)$$

and the variance

$$(\Delta M)^2 = \sum_x p(x) (x - \langle M \rangle)^2 = \langle M^2 \rangle - \langle M \rangle^2 \quad (2.13)$$

are used. As we will see, it often turns out that phase estimation based on the mean and the variance of the number difference is already sufficient to reach optimal phase sensitivities.

Figure 2.3 visualises the calculation of the value and the uncertainty of the phase shift from the mean  $\langle N_- \rangle$  and the standard deviation  $\Delta N_-$  of the population imbalance for a fixed total number  $N$ . The fluctuations in the measured number difference translate to fluctuations in the phase estimation via the slope of the mean value. This simple error propagation gives rise to the method of moments formula for the phase uncertainty

$$\Delta \theta_{\text{MOM}} = \frac{\Delta N_-}{|\partial_\theta \langle N_- \rangle|}. \quad (2.14)$$

A similar approach also applies to higher moments, where for example the signal is given by the variance (instead of the mean) and the fluctuations by the variance thereof. This is used for the analysis of twin-Fock states and presented in more detail in the next section.

If technical noise can be neglected and we employ states of uncorrelated atoms only, the fluctuation that remains is the shot-noise  $\Delta N_- = \sqrt{N}$ , fundamental to the stochastic process of  $N$  independent atoms choosing output state  $A$  or state  $B$  with a probability of 50%

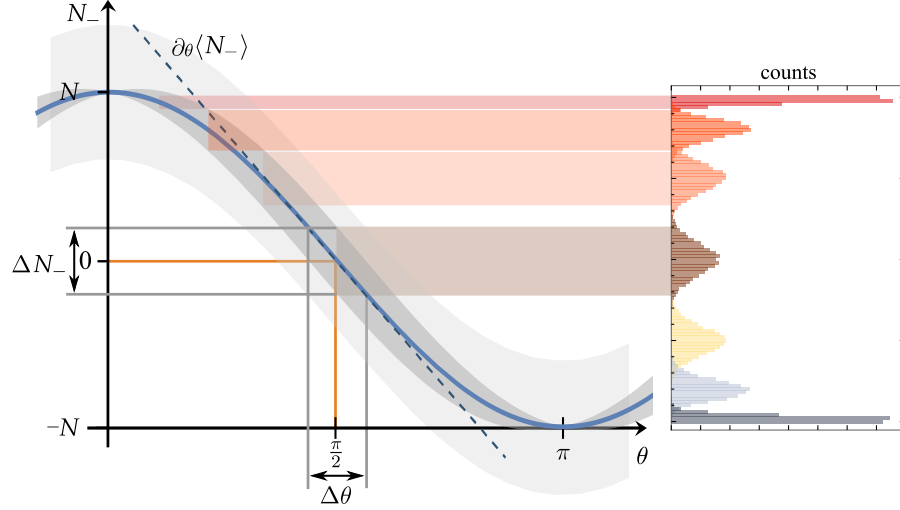


Figure 2.3: A noisy interferometer signal to illustrate the SQL. The phase shift is obtained from the measurement of the number difference  $N_-$  between the output ports of an interferometer. For each phase shift  $\theta$ , the mean  $\langle N_- \rangle$  (blue line) and the fluctuations of the measured distribution are shown. Its uncertainty can stem from quantum fluctuations (dark grey area), be of technical origin (light grey area), or a combination of both. The slope of the mean with respect to the phase is largest at  $\theta = \pi/2$  (so-called mid-fringe position, vertical orange line). The phase estimation uncertainty is proportional to the uncertainty in the number difference and anti-proportional to the slope of the signal. If the quantum fluctuations dominate (that is no light grey area), the reduced fluctuation towards the extreme points is exactly nullified by the decreasing slope and the phase estimation uncertainty becomes the phase independent SQL.

each. This scenario is equal to a CSS on the equator, where the uncertainty of  $J_z$  directly corresponds to the shot noise in the measurement of the population imbalance

$$\Delta N_- = \Delta(N_A - N_B) = 2\Delta J_z = \sqrt{N}. \quad (2.15)$$

In the case shown in Figure 2.3, the mean value  $\langle N_- \rangle$  follows the function  $N \cos(\theta)$  with maximum slope  $|\partial_\theta \langle N_- \rangle| = N$  at  $\theta = \pi/2$ . Hence, the above phase uncertainty  $\Delta\theta_{MOM}$  cannot go below the standard quantum limit (SQL) [49]

$$\Delta\theta_{SQL} = \frac{1}{\sqrt{\nu}\sqrt{N}}. \quad (2.16)$$

The assumption, that each atom ends up in one state or the other independently of all other atoms, is reflected by the equal influence of the number of atoms  $N$  and the number of trials  $\nu$  on the statistical uncertainty of the phase estimation. The phase uncertainty is the same, if the experiment is done once with  $N$  atoms or  $N$  times with one atom. This limit holds for standard two-mode interferometers (imprinting

the phase by a collective unitary rotation) and using separable states. The limit is independent of the phase and the chosen observable, and applies to ensembles with fluctuating total atom number [50]. Note that in the case of a relative phase imprint between more than two interferometric modes, the SQL generalises to [49, 51]

$$\Delta\theta_{\text{SQL}} = \frac{1}{\sqrt{\nu}\sqrt{N}(m-1)} \quad (2.17)$$

where  $m$  is the number of modes.

In a more general setting, the ideal phase uncertainty is attained by incorporating not just the slope of the mean but the rate of change of the whole distribution of outcomes. The quantity that does the job is the Fisher information (FI) [49]

$$F(\theta) = \sum_x \frac{1}{p_x(\theta)} \left( \frac{\partial p_x(\theta)}{\partial \theta} \right)^2. \quad (2.18)$$

It measures the rate of change of the probability of each outcome  $x$  upon a change of the phase  $\theta$ . It can be shown to be directly linked to the phase estimation uncertainty by the Cramér-Rao bound [49]

$$\Delta\theta_{\text{CR}} = \frac{1}{\sqrt{\nu}\sqrt{F(\theta)}}, \quad (2.19)$$

which constitutes a lower bound to the phase uncertainty that can be reached for a chosen input state and observable.

In the context of quantum mechanics, one can introduce an upper bound to the FI by maximizing over all possible measurements  $M$  such that the bound becomes independent from the chosen observable. For a general input state  $\rho_{\text{in}} = \sum_k p_k |k\rangle \langle k|$  (arbitrary basis) this results in the quantum Fisher information (QFI) [49]

$$F_{\text{Q}}[\rho_{\text{in}}, H_{\text{IF}}] = 2 \sum_{k,l} \frac{(p_k - p_l)^2}{p_k + p_l} |\langle k | \Delta H_{\text{IF}} | l \rangle|^2, \quad (2.20)$$

which for pure states simplifies to  $F_{\text{Q}}[|\psi\rangle_{\text{in}}, H_{\text{IF}}] = 4(\Delta H_{\text{IF}})^2$ . Here,  $H_{\text{IF}}$  is a Hamiltonian describing the unitary evolution due to the interferometer, e. g.  $H_{\text{IF}} = J_y$  in the case of the configuration of Figure 2.1, and the variance  $\Delta H_{\text{IF}}$  is calculated with respect to the input state  $\rho_{\text{in}}$ . The QFI does not depend on the phase or the observable anymore and therefore serves to characterise the input state. A QFI that exceeds the number of atoms  $F_{\text{Q}} > N$  quantifies inter-particle entanglement that is useful to enhance the phase estimation [18] and is a measure of the entanglement-depth [52]. Roughly speaking, the larger the QFI, the larger are the mutually entangled clusters of particles within the ensemble and the larger is the potential of the state for enhanced phase estimation. The ultimate potential for phase uncertainty is reached by the genuine N-particle entangled NOON-state  $(|N, 0\rangle + |0, N\rangle)/\sqrt{2}$

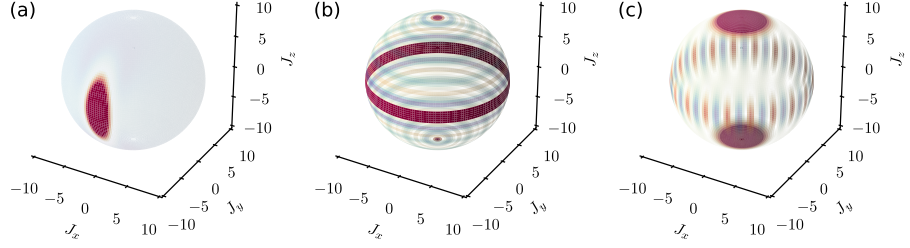


Figure 2.4: Entangled states on the many-body Bloch sphere visualised by their Wigner distribution (red is positive and blue negative values). (a) A spin-squeezed state shows reduced fluctuations in one direction and increased fluctuations in the orthogonal direction, in accordance with the uncertainty relation in Equation 2.10. (b) The twin-Fock state is depicted by a ring on the equator. From its vanishing number difference  $\Delta J_z = 0$  follows a completely undefined relative phase between the two modes. (c) The maximally entangled NOON state with small structures varying in sign on the equator that give rise to extreme sensitivity upon rotation around  $J_z$ . Here  $N = 20$ .

with a QFI of  $F_Q = N^2$  which leads to the ultimate Heisenberg limit in phase uncertainty

$$\Delta\theta_{\text{HL}} = \frac{1}{\sqrt{\nu N}}, \quad (2.21)$$

which shows an improved scaling with the number of employed atoms  $N$  compared to the number of trials  $\nu$ .

To intuitively explain the performance of highly-entangled states like the NOON-states, we employ quasi-probability distributions as a general way to depict many-body states on the surface of the Bloch sphere. One choice is the Wigner distribution  $W(\varphi, \vartheta)$ , which assigns a value to each point on the sphere's surface in a one-to-one correspondence to the states density matrix [25] (for details see Section A.3). The Wigner distribution can show negative values which are often connected to non-classical features and can lead to an intuitive understanding of the phase sensitivity of highly-entangled states.

In Figure 2.4, a spin-squeezed state, a twin-Fock state and a NOON-state are compared. A spin-squeezed state works exactly in the same manner as a CSS and simply reduces the phase uncertainty by sub-shot-noise fluctuations in the direction of the phase sensing. The use of the Wigner distribution becomes especially apparent in the case of the NOON-state. This state shows its extreme sensitivity not for a rotation around an axis in the equatorial plane, as the maximally stretched superposition of the states  $|N, 0\rangle$  and  $|0, N\rangle$  would suggest. The actual sensitivity is reached for a rotation around the  $J_z$  axis, where the states  $|N, 0\rangle$  and  $|0, N\rangle$  are unaffected but the small substructures on the equator (alternating in sign) move. In a final measurement these small structures manifest in an odd-even structure of the outcome distribution, where, depending on a tiny phase difference, either only

even or only odd number differences are measured. This performance is therefore easily ruined by technical noise in the final detection.

The twin-Fock state  $|N/2, N/2\rangle$  is a ring on the equator with ideally vanishing fluctuations in the number difference  $\Delta J_z = 0$ . Its Wigner distribution shows substructures as well and also the distribution of outcomes shows odd-even structures. However, in contrast to the NOON state, the performance of twin-Fock states can also be employed by observing only global properties of the distribution. Using the method of moments and the variance  $(\Delta J_z)^2$  instead of the mean as a signal actually allows to saturate the Cramér-Rao bound given by the QFI  $F_Q[|N/2, N/2\rangle, J_y] = N^2/2 + N$ . Some characteristics of twin-Fock states are presented in the following.

### 2.1.3 Number squeezing and useful entanglement

Twin-Fock states aligned on the equator of the Bloch-sphere ideally show a vanishing variance in the number difference  $\Delta N_- = 0$ . In the experiment of course some residual fluctuations are measured, mainly depending on the level of the noise in the detection of atom numbers. In our experiments, a reduction to less than 6 % of the usual shot-noise fluctuations in an ensemble of  $\langle N \rangle = 8000$  has been recorded [53]. This reduction of the fluctuations is referred to as number squeezing. However, the sole observation of number squeezing is only sufficient to verify entanglement if the state is symmetric, i. e. all atoms are indistinguishable, which is not guaranteed for in the experiments. Furthermore, number squeezing would be observed independently of the size of the twin-Fock states in the ensemble. It is only necessary that all, or at least a major fraction of the atoms, populate some kind of twin-Fock state. For example, if we somehow choose for pairwise entanglement only, the ensemble could be described by a product state of  $N/2$  two-particle twin-Fock states  $\otimes_{i=1}^{N/2} |1, 1\rangle^{(i)}$ . The collective measurement of the number difference in the ensemble is now identical to a (hypothetical) pairwise measurement of  $\langle 1, 1 | J_z | 1, 1 \rangle = 0$ , which still results in ideally vanishing fluctuations of the number difference (see Figure 2.5, second row). Therefore, by the measurement of number squeezing only, we cannot distinguish whether the atoms are all entangled with each other ( $N$ -partite entanglement) or within clusters of  $k$  or less atoms ( $k$ -partite entanglement). This entanglement depth, however, determines the phase sensitivity of the state.

The actual entanglement depth of the twin-Fock state is reflected in a measurement of an orthogonal component of the pseudo-spin. In the Bloch sphere picture, this measurement constitutes a rotation of the twin-Fock ring by  $\pi/2$  such that it stands upright before the measurement of the population imbalance. Projecting the ring onto the  $J_z$  axis gives a typical wing distribution with an accumulation of outcomes at the extreme points. Measuring the variance  $(\Delta J_\perp)^2 = \langle J_\perp^2 \rangle$  of this

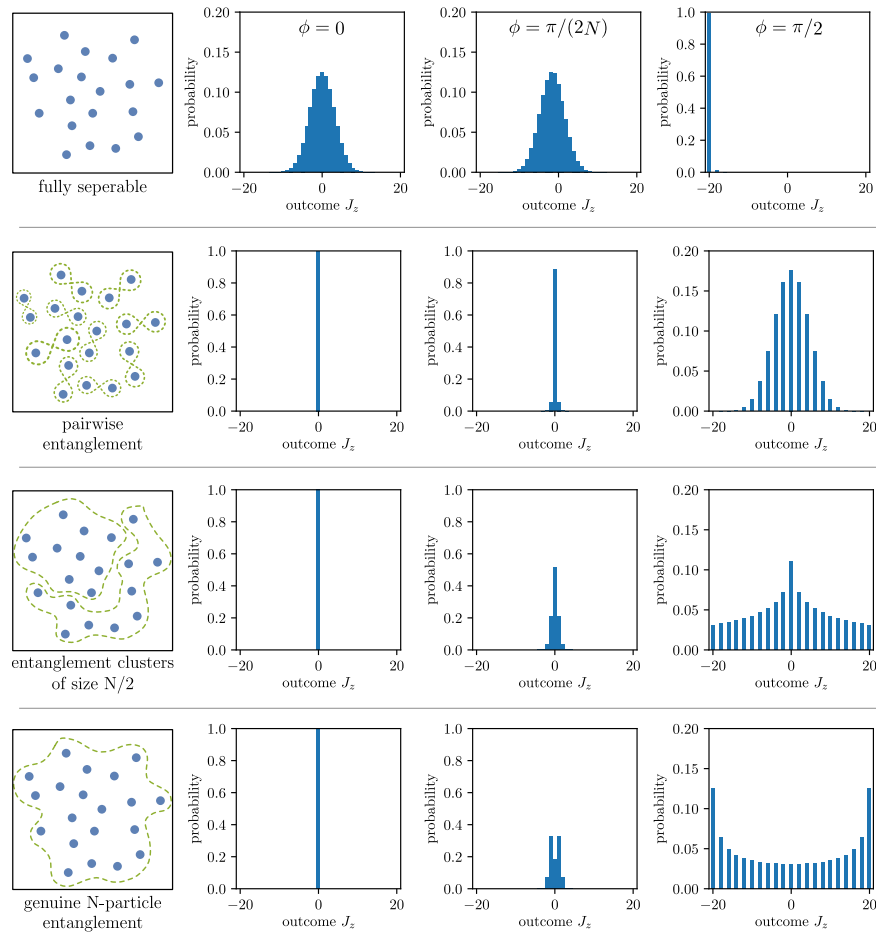


Figure 2.5: Number squeezing and orthogonal spin length for different entanglement structures. Each row shows a different entanglement depth. The outcome distributions depict the expected outcomes after a collective rotation by  $0$ ,  $\pi/(2N)$ ,  $\pi/2$  around the  $J_y$  axis respectively. The fully separable state (first row) shows a Gaussian distribution with a width connected to shot-noise. Upon a small rotation by  $\pi/(2N)$  the outcome distribution changes only slightly. The rotation by  $\pi/2$  turns the state onto the south pole. Despite the singular outcome at this point, this is still a simple CSS. The outcome distributions for the pairwise entangled twin-Fock states (second row) shows the mean pseudospin length of zero  $\langle J_x \rangle = \langle J_y \rangle = \langle J_z \rangle = 0$ , typical for twin-Fock states. However, the extreme values of  $\pm N/2$  are not reached (here  $N = 40$ ). If the ensemble is split into two entanglement clusters of size  $N/2$ , these extreme points are reached, but the outcomes do not accumulate at the extreme points. The  $N$ -particle entangled ensemble shows the typical wing distribution after a  $\pi/2$  rotation. Also note that for small phase shifts  $\pi/(2N)$  (third column) the distribution changes most in the case of the state  $|N/2, N/2\rangle$ . According to the FI and the Cramér-Rao bound, we expect the largest phase sensitivity here.

distribution characterises the pseudospin in the plane orthogonal to the number squeezing. If the twin-Fock state consists of less atoms, the ring has a smaller radius and the extreme points are less likely to be measured. In general, the distribution of outcomes is given by the convolution of the distributions of each sub-state. In the exemplary case of  $N/2$  two-particle twin-Fock states, the measurement of a single pair of atoms gives  $\pm 1$  as extreme points. Each two-particle twin-Fock state shows an outcome independently of the other twin-Fock states in the ensemble, which makes it very unlikely to collectively measure the extreme values  $\pm N/2$  as shown in [Figure 2.5](#) (second row). Also in the case of an  $N/2$ -partite entangled ensemble, the typical wing distribution is not established for a collective measurement. Therefore, the entanglement depth has to be relatively close to the  $N$ -particle entangled twin-Fock state for the typical wing distribution to emerge.

To characterise twin-Fock states in our experiment, we measure a generalised squeezing parameter [\[54, 55\]](#)

$$\xi^2 = (\langle \hat{N} \rangle - 1) \frac{(\Delta J_z)^2}{2 \langle J_\perp^2 \rangle - \langle \hat{N} \rangle / 2}, \quad (2.22)$$

a quantity that for the above reasoning combines the measured number squeezing  $(\Delta J_z)^2$  and the variance in the orthogonal plane  $\langle J_\perp^2 \rangle$ . It is formulated on the basis of uncertainty relations that predict  $\xi^2 \geq 1$  for separable states. Therefore, a measured squeezing parameter less than one  $\xi^2 < 1$ , verifies entanglement. Note that for ideal twin-Fock states the generalised squeezing parameter vanishes.

The potential of pure twin-Fock states for phase estimation can be fully utilised by recording the change of the variance  $\langle J_\perp^2 \rangle$  with an interferometric phase shift  $\theta$  and applying the method of moments ([Equation 2.14](#)) similarly to tracking the change of the mean in the case of using a [CSS](#). To see the transition from one observable to the other being favourable, [Figure 2.6](#) shows the metrological gain based on the two-particle mixture

$$\rho_2 = (1 - p) |0, \pi/2, 2\rangle \langle 0, \pi/2, 2|_{\text{CSS}} + p |1, 1\rangle \langle 1, 1|_{\text{TF}}, \quad (2.23)$$

of a [CSS](#) defined according to [Equation 2.9](#) and a twin-Fock state. As in the above example of an ensemble of  $N/2$  entangled pairs, this state is to be thought as describing the state of each pair in an ensemble of  $N$  atoms. In the case of  $p = 0$ , the ensemble is purely in a state of an  $N$ -particle [CSS](#), whereas for  $p = 1$  the ensemble is in the pure state of  $N/2$  pairwise entangled twin-Fock states. The metrological gain is defined as the enhancement factor of the phase sensitivity compared to the [SQL](#) in terms of variances

$$(\Delta\theta_{\text{SQL}})^2 / (\Delta\theta)^2. \quad (2.24)$$

For [Figure 2.6](#),  $(\Delta\theta)^2$  is computed by the method of moments with respect to the mean (blue) and the variance (orange), or in terms of



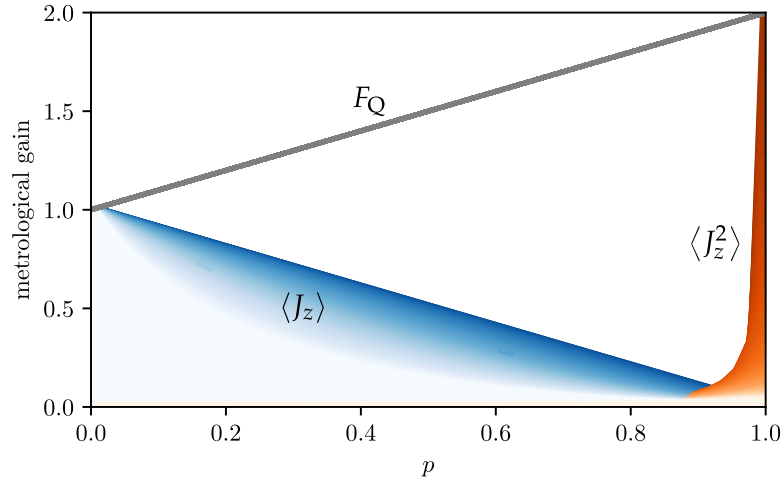


Figure 2.6: Metrological gain of an ensemble of  $N$  atoms in a mixed state of a CSS and pairwise entangled twin-Fock state. The metrological gain over the SQL  $(\Delta\theta_{\text{SQL}})^2 = (1/\sqrt{N})^2$  is shown in terms of a measurement of the mean  $\langle J_z \rangle$  (blue), the variance  $\langle J_z^2 \rangle$  (orange) and the QFI  $F_Q[\rho_2, J_y]$  (grey line). The gradient in the colour represents the dependence of the respective gain on the absolute phase shift from small (dark) to large (light). Here  $N = 100$ , i. e. a product state of 50 two-particle states of Equation 2.23.

the QFI (grey line). Using the signal in the mean or the variance only reaches the optimal metrological performance given by the QFI in the case of a pure CSS or pure twin-Fock states, respectively. The potential metrological performance of the mixture increases with the portion of twin-Fock states, but is not captured by tracking the mean neither the variance. Even if the ensemble shows only pairwise entanglement, the ideal phase estimation is a factor of 2 beyond the SQL. In the case of  $N = 100$  particles shown here, the other two exemplary entanglement structures of Figure 2.5 show a similar graph, but with reasonably higher maximum metrological gains of 26 and 51 in the case of a pure twin-Fock state. Here and in the following, the values for the metrological gain are expressed as the linear enhancement of the variances as given by Equation 2.24. The expression of squeezing values follows the common choice of using decibel, i. e.  $10 \log_{10}(\xi^2)$ .

## 2.2 ENTANGLEMENT IN COLD ATOM EXPERIMENTS

### 2.2.1 Realisations in spin space

Entangled many-body states have been realised in various cold atom experiments. In the vast majority of realisations, the entanglement was established among different spin states of the atomic ensemble.

To introduce entanglement, some form of interaction has to be established. Among the so far realised schemes to entangle spin states of



cold atomic ensembles, the interaction is either based on inter-atomic s-wave collisions in Bose-Einstein condensates or based on the atom-light interaction inside of cavities. A conceptually different approach are non-demolition measurements, where the state of the ensemble is measured by a weak interaction, which creates a conditional spin-squeezed states if the additional information of the non-demolition measurement is used.

In two-component BECs, spin-preserving collisions between atoms of the same spin state can be utilised for the generation of spin-squeezing. The interaction is usually too small and has to be enhanced either by tuning the difference of the scattering lengths using a Feshbach resonance [23] or by tuning the spatial overlap of the two components using state-dependent potentials [56]. Here, the BECs were captured in a one dimensional lattice or in a magnetic trap on an atom chip and reached  $-8.2$  dB and  $-3.7$  dB squeezing, respectively. Introducing an additional coupling between the two components, the modified twist-and-turn dynamics has been used to prepare  $-7.1$  dB spin-squeezed states [57]. On the atom chip, a scanning probe interferometer that measured microwave magnetic fields with a metrological gain of 2.5 has been demonstrated [26]. A magnetometer beyond the SQL has also been demonstrated in the experiment using an optical lattice [58], and here also non-Gaussian over-squeezed states proved to achieve sub-SQL performance [59].

Spin-changing collisions within Spin-1 BECs (three spin components), held in an optical dipole trap, have been used to generate either two-mode spin-squeezed states [27, 60–62] with up to  $-8.3$  dB squeezing or highly-entangled twin-Fock states [63, 64]. Using this physical system, a microwave atomic clock with a metrological gain of 1.6 has been demonstrated in our group [27], as well as a metrological gain of 1.5 using twin-Fock states [63]. More recently, employing the similar class of Spin-1 Dicke states, a metrological gain of 1.7 beyond the three-mode SQL and a gain of 7 beyond the usual two-mode SQL has been demonstrated [51].

The quantised atom-light interaction within cavities has been applied to generate spin-squeezed states and W states in gas cells [22, 65] and in laser-cooled ensembles [66–70]. Also the atom-light interactions in a cavity have been successfully used to generate spin-squeezing in Ytterbium, a species offering an optical clock transition [71]. Recently, along the same line of research, the first directly entanglement-enhanced optical clock was realised and showed a metrological gain of 2.8 [28]. The current record on squeezing ( $-20.1$  dB) has been obtained by exploiting the information from a weak coupling between the light field in a cavity and an atomic ensemble that is trapped inside the cavity, demonstrating a directly observed metrological gain of more than 70 [72]. Such cavity-based squeezing concepts have also been applied to improve an atomic clock beyond the SQL [73].

These results have all been attained in spin space. However, for the application of entangled ensembles in inertially sensitive atom interferometry, entanglement in external (motional) degrees of freedom is needed.

### 2.2.2 *Entanglement in external degrees of freedom*

The above-mentioned spin-preserving and spin-changing collisions also proved to generate entanglement between spatial regions and spatial modes of BECs [74–76]. Particle entanglement between two spatial modes of a double well potential has been generated using the repulsive interaction between two components of a BEC upon the splitting process. By this technique, squeezing between the spatially separated modes of an optical multi-well trap was created [21] and a number squeezed input state for an interferometer within a double-well potential on an atom chip was realised [77]. For the application in inertially sensitive atom interferometry, however, the challenge would be the individual addressing of these spatial modes to transfer them into the momentum modes of an interferometer.

Entanglement has already been directly created in momentum space. A one-dimensional degenerate Bose gas, prepared in an excited trap mode by non-adiabatic movement of the magnetic trapping potential, has been shown to create entangled beams of twin-atoms upon collisional de-excitation [41]. In another approach, two colliding BECs are the source for scattered atoms with correlated momenta [42, 45]. Here, the BECs are accelerated by Bragg or Raman light-pulses and upon the collision of the clouds, atoms are ejected in all spatial directions. Though entanglement witnessed by Bell correlations [45] and the ability to measure magnetic fields [78] have been demonstrated, the prepared momentum modes are not suitable for the integration in an inertially sensitive atom interferometer.

### 2.2.3 *First steps and proposed routes towards entanglement-enhanced inertial sensing*

The first experimental steps towards quantum-enhanced light-pulse atom interferometry have recently been made. An ensemble of thermal atoms, spin-squeezed by means of a cavity-based non-demolition measurement, was released to free space. Entanglement was preserved for free-fall times up to 8 ms and a microwave atomic clock sequence in free-fall showed a metrological gain of 2.4 [79]. Very recently, in a similar system, the first full light-pulse matter-wave interferometer using up to  $-3.4$  dB squeezed momentum modes has been realised. Here, the squeezed momentum modes were generated by two cavity-based methods, i. e. a non-demolition measurement and a spin-dependent interaction with the cavity light. Subsequently to the entangling pro-

cess, the thermal ensemble undergoes guided free fall and a sequence of three Raman light pulses span a Mach-Zehnder like interferometer in space-time. A metrological gain of 1.5 for  $N = 660$  atoms was measured regarding a variation of the phase of the closing light-pulse of the interferometer [48]. Here, the number of atoms was limited due to the need of velocity selection before the momentum transfer. In principle, the demonstrated configuration can be employed for inertial sensing. However, a sensitivity to, for example Earth's acceleration, has not been demonstrated.

The methods used in both experiments have so far only been demonstrated with thermal atomic ensembles. Using BECs instead, would make it less challenging to exploit large momentum transfer schemes with long free fall times as well as to suppress spatial dephasing during the interferometer. In the main work of this thesis, entangled momentum modes featuring the mode quality of BECs have been prepared [47]. This was achieved by creating twin-Fock states of about  $10^4$  atoms by spin-changing collisions and then coherently transfer one of the twin modes to a well-separated momentum mode. To this end, a stimulated Raman transition was used, which is an established technique in the field of light-pulse atom interferometry. The entanglement could be detected after 15 ms free-fall and persisted the transfer to momentum space. An inertially sensitive interferometer could be spanned by a sequence of Raman or Bragg pulses, subsequent to the demonstrated preparation of the entangled source.

Besides these promising experimental achievements, alternative approaches working with well-suited momentum modes have so far only been proposed theoretically. Some protocols aim for Raman- and Bragg-pulse interferometry and use the atom-light interaction in optical cavities to directly entangle momentum modes [80–82]. A recent proposal avoiding cavities suggested to use the interatomic collisional interactions that are triggered upon separation by Raman light pulses and the expansion of BECs to prepare squeezed momentum modes [83]. Interestingly, these interactions have been up to now usually regarded as a source of dephasing which has to be prevented. Along the same line of thought, further engineering of the interaction by an additional collimation of the clouds has been proposed [84]. The analysis was extended also to light-pulse atom interferometry using Bragg scattering and even added a non-linear readout to achieve detection-noise robustness. Recently, a detailed review of the prospects and challenges of implementing entanglement-enhanced inertial sensors with cold atoms has been published [40], expressing the pursuit of employing entanglement.



When a gas of bosonic atoms is cooled down close to absolute zero, the atoms collectively populate the lowest possible quantum state and form a state of matter called a Bose-Einstein condensate (BEC). Spinor BECs additionally offer the possibility to manipulate their internal spin degree of freedom, in our case by trapping a BEC independently of its spin state in an optical dipole trap. Therefore, we are interested in the distribution among the different spin states, the dynamics that changes this distribution in time and the specific many-body quantum states that emerge from this dynamics. To this end, we usually simplify our system regarding the external degrees of freedom by assuming complete condensation, i. e. no thermal background, and identical spatial and motional modes for all atoms. The BEC can in principle populate several excited modes of the trap, which has been studied extensively in our group [74, 85]. In the course of this thesis, it is sufficient to confine the description to the lowest trap mode and treat the population of higher spatial modes simply as a loss of atoms. Within this single-mode approximation (SMA), the quantum dynamics of the spin states is described by a straightforward Hamiltonian depending on one main experimental parameter only. By properly tuning this parameter, various dynamics can be realised, ranging from the original schemes to prepare spin-squeezed states proposed in the early 90s [20, 61] to more recent protocols utilizing a quasi-adiabatic change of this parameter to generate highly entangled twin-Fock states [64, 86–88]. Spin dynamics is our tool to prepare various entangled states in the lab, all interesting by themselves and many of use to enhance the precision of interferometric measurements.

### 3.1 OUR APPARATUS IN A NUTSHELL

At first, the apparatus utilised to prepare and study  $^{87}\text{Rb}$  spinor BECs will shortly be introduced. A detailed presentation can be found in earlier theses [54, 89, 90]. The main techniques used at our experiment are elucidated by chronologically following a typical experimental sequence.

The vacuum system of the apparatus divides into two glass chambers connected by a differential pumping stage. On one side, a 3D magneto-optical trap (MOT) is loaded with atoms from the background gas by the aid of light-induced atom desorption [91]. The MOT is loaded with around  $10^9$  atoms in 10 s. After cooling further with an optical molasses for 5 ms, the atoms are pumped to the state

$|F = 2, m_F = 2\rangle$  by circularly polarised light to enable pure magnetic trapping. The coils for this magnetic trap are mounted on a mechanical sledge which allows to move the magnetic potential horizontally for about 0.4 m. The atoms follow the potential through a small tube (differential pumping stage) into the second glass cell, where the atoms find ultra-high vacuum with a pressure in the range of  $10^{-11}$  mbar. A stationary magnetic trap takes over the trapping and the ensemble is cooled further by radio-frequency assisted evaporative cooling [92]. Now, the remaining kinetic energy of the atoms is low enough to allow for optical trapping. A red-detuned optical dipole trap formed by two crossed laser beams with 1064 nm wavelength is switched on. Within the dipole trap, the atoms are cooled below the critical temperature by another evaporative cooling procedure, where the trapping potential is gradually lowered to expel the hottest atoms from the ensemble [93]. Finally, at a certain trapping potential, a large fraction of the ensemble undergoes the transition to a BEC. Reducing the potential further expels the remaining thermal atoms, leaving a pure BEC with up to  $1.5 \times 10^5$  atoms. Usual ensemble sizes for our experiments range from  $5 \times 10^3$  to  $8 \times 10^4$  atoms which is chosen by setting the lowest trapping potential.

To hold the atoms for the subsequent experiments, the optical trapping potential is ramped up to a fixed value again which determines the stiffness of the trap. Higher trapping frequencies as well as higher atom numbers increase the density of the ensemble, thereby increasing atomic interactions which in turn reduce the life time of the BEC. A detailed discussion of the dipole trap can be found in [90]. Commonly, we work at trap frequencies of  $2\pi \times (150 - 250)$  Hz, reaching half-life times for condensates with  $10^4$  atoms of about 5 s (caused mainly by three-body losses) and reasonable interaction strength for spin-changing collisions ranging from  $2\pi \times (5 - 15)$  Hz. The interaction strength can be adjusted by the total atom number and the stiffness of the trap. The spin-changing collisions produce correlated pairs of atomic spins and allow us to prepare various entangled many-body states. Details of this spin dynamics are discussed in Section 3.3.

To lift the degeneracy within each hyperfine manifold, a homogeneous magnetic field is switched on. The field amplitude is set to around 1 G (to be precise 0.73 G for the experiments presented later on) and actively stabilised to fluctuations down to 40  $\mu$ G (one standard deviation, directly measured with the atoms). The active magnetic field stabilisation has been thoroughly studied and details can be found in Ref. [94]. For the experiments presented in this thesis, the magnetic field needed to be aligned along the direction of the Raman laser beams (direction of gravity and orthogonal to original setting) to enable the interaction of  $\sigma_{\pm}$  polarised Raman light with the free-falling atoms. To this end, another pair of coils in Helmholtz configuration has been installed on top and below the science glass chamber. Due

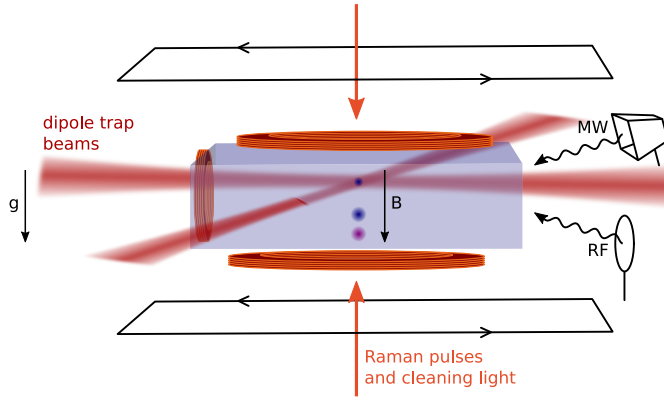


Figure 3.1: Sketch of the key elements of the experimental setting. The BEC is held in a red-detuned optical dipole trap within a static and homogeneous magnetic field of around 1 G. To manipulate the hyperfine levels, microwave frequency (MW) and radio frequency (RF) pulses are used to drive transitions and apply dressing fields. When released from the optical trap, the free-falling ensemble can take up momentum from stimulated Raman transitions and finally be detected by absorption imaging. Momentum modes spatially separate in vertical direction after sufficient time-of-flight, whereas different spin components separate horizontally due to an inhomogeneous magnetic field prior detection. Elements are not to scale.

to unconventional size and distance of the coils, the stabilised field in vertical direction fluctuates with  $170 \mu\text{G}$ .

To prepare the atoms in a spin state at will, we need the ability to coherently transfer the atoms from one spin state to the other. This is done by irradiating the atoms with resonant microwave frequencies MW (for transitions between the hyperfine manifolds) or radio frequencies RF (within one hyperfine manifold) to initiate Rabi oscillations between the addressed states. In addition, MWs are utilised to non-resonantly couple two hyperfine levels and thereby shift their potential energy in dependence on the detuning and the intensity of the MW radiation. This technique is called microwave dressing and can be understood in terms of the dressed state model [53, 95].

For typical experiments, the atomic ensemble is transferred from the state  $|F = 2, m_F = 2\rangle$  to the state  $|F = 1, m_F = 0\rangle$  by three resonant MW pulses. To ensure the sole population of this state, residual atoms in the  $F = 2$  manifold are removed from the ensemble by light pulses resonant to  $F = 2$  states only. Any remaining atoms in the states  $|F = 1, m_F = \pm 1\rangle$  are removed by resonant MW  $\pi$ -pulses to  $|F = 2, m_F = \pm 2\rangle$  prior to another cleaning light pulse. At this stage of the state preparation, the ensemble represents a polarised CSS in  $|F = 1, m_F = 0\rangle$  and can be applied as input state of an interferometric measurement limited by the SQL. A subsequent preparation of a superposition of atoms in the two clock states  $|F = 1, m_F = 0\rangle$  and



$|F = 2, m_F = 0\rangle$ , for example, opens an interferometer sensitive to the detuning of the MW coupling pulse with respect to the clock transition. After another coupling, the final population of the clock states encodes the detuning and can serve as a frequency reference, realising an atomic microwave clock.

Entanglement can be introduced by initiating spin-changing collisions, which produce correlated pairs of atoms in the levels  $|1, \pm 1\rangle$ . At a magnetic field of about 1 G and in  $F = 1$ , the dynamics is suppressed since the energy of a pair of atoms in the levels  $|1, \pm 1\rangle$  is much higher than the energy of a pair of atoms in  $|1, 0\rangle$ . In other words, the present state of the ensemble represents the ground state of the system. To initiate spin dynamics, the energy of the atoms in  $|1, 0\rangle$  is raised by the aforementioned MW dressing technique such that the population of the levels  $|1, \pm 1\rangle$  is favoured. Already a mean transfer of less than one atom to  $|1, \pm 1\rangle$  represents a two-mode squeezed vacuum state. At our experiment, this squeezed state was used as second input state to the abovementioned atomic microwave clock sequence to enable a sensitivity beyond the SQL [27]. Details about the various ways to prepare entangled states using spin dynamics in  $F = 1$  are presented in Section 3.3 and Section 4.3.

Subsequent to the in-trap operations, the BEC is released into free space by switching off the optical trapping potential. The mean-field energy of the ensemble (the atoms repel each other) drives an accelerated expansion that turns into a ballistic expansion within a millisecond of free fall. The rate of the ballistic expansion can be reduced in two ways. Either the trapping potential is slowly ramped down to reduce the mean-field energy in the first place, or the atoms are shortly exposed to a potential that converts the kinetic energy of the expanding cloud to potential energy, which vanishes when the potential is switched off quickly again. The first technique comes with two problems. Long holding times are necessary to avoid excitations to higher trap modes and along the way the varying trap leads to varying spin-dynamics conditions that alters the many-body state in a hardly controllable way. Both effects would especially deteriorate the usefulness of entangled states. Therefore, we choose to reduce the ensembles expansion rate by flashing on the optical trapping potential after a short free fall time of 1 ms. This technique is called delta-kick collimation and is discussed in detail in Section 5.2.

At the present geometry, the apparatus allows for about 20 ms collimated free fall before the clouds leave the region of the absorption detection. Before taking images of the atomic cloud, the spin components of the ensemble are spatially separated by a magnetic field gradient (as the spins in the famous Stern-Gerlach experiment). The orientation of the magnetic field gradient causes a horizontal separation of the spin components, that is perpendicular to the direction of the momentum transfer needed to implement a matter-wave in-



terferometer sensitive to Earth's gravity. An in-depth discussion of the final absorption detection can be found in Ref. [54]. The detection system allows to determine the atom number in each component of the ensemble with an uncertainty of 15 atoms. The actual performance depends on the final size of the atomic clouds, which in turn depends on the number of atoms, expansion rate and free-fall time. To analyse the ability to count atom numbers with sub-shot noise performance after substantial free fall was central to the main results of this thesis and is further discussed in Section 5.2.

The possible experiments are of course much broader than sketched by this exemplary sequence. Various initial spin populations can be realised, holding times in the dipole trap may range from less than a millisecond to seconds and various combinations of coupling pulses allow to implement a variety of measurement protocols.

### 3.2 MANIPULATING HYPERFINE LEVELS

Coherent transfers between the hyperfine levels can be driven by irradiating the atomic ensemble with electromagnetic (EM) waves of suitable frequency and polarisation. In the vicinity of a homogeneous magnetic field in the range of a few Gauss, the employed frequencies range from 500 MHz to 6.835 GHz equivalent with a wavelength of more than half a meter down to about 40 cm. Since usual ensemble sizes of several  $\mu\text{m}$  are much smaller, the EM field can be regarded homogeneous over the extent of the ensemble, which is necessary to preserve coherence between all atoms after the interaction.

Since the electronic ground state  $5^2\text{S}_{1/2}$  has an orbital angular momentum of  $l = 0$ , the dipolar interaction with the electric field component vanishes. Therefore the relevant interaction of the atoms with the EM field is given by the coupling to the magnetic field component. When formally describing the MW interaction, it is usually sufficient to reduce the atomic system to those two levels which are resonantly coupled. If the frequency selectivity is not adequate, the approximation to two levels in principle can be met by confining the radiation to the required polarisation only. In the case of mixed polarisations, the fraction of the magnetic field which is  $\sigma_{\pm}$  polarised drives transitions with  $\Delta m_F = \pm 1$  and the  $\pi$  polarised fraction drives the  $\Delta m_F = 0$  transitions, since the combined angular momentum of atomic hyperfine level and the photons of the EM field needs to be conserved. Thus, by aligning the oscillating magnetic field with the static magnetic field properly, this polarisation-dependent selectivity could be employed to address a specific transition only, without relying on the mere selectivity by the frequency. polarisation-selective MW transitions have been realised by using antenna designs emitting mainly circular polarisation and additional alignment of the static magnetic field [96]. Implementation of this technique would be in particular useful to prevent cross-couplings

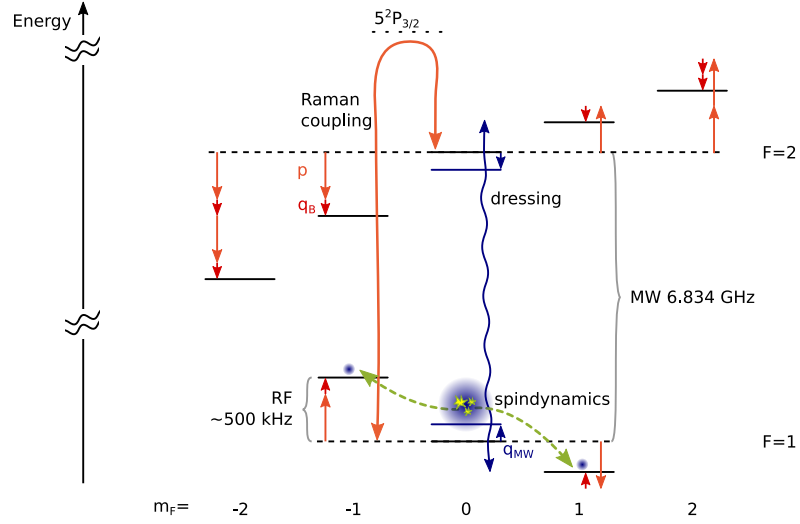


Figure 3.2: Energy of hyperfine levels of the electronic ground state in  $^{87}\text{Rb}$  at a few Gauss magnetic field. The small orange and red arrows depict the linear ( $p$ ) and quadratic ( $q_B$ ) portion of the Zeeman shift. The energetic separation within a spin manifold is in the RF range, whereas distance between  $F = 1$  and  $F = 2$  corresponds to MW. The Raman light (orange arch) couples the two clock states by a two-photon process via the higher electronic level, enabling a coherent transfer of substantial photon momenta to the atoms (details see Section 5.1). A blue detuned dressing MW (blue wavy line) is used to shift the lower clock state by  $q_{MW}$ , which causes an effective shift of  $q = q_B + q_{MW}$  and is used to initiate spin dynamics in  $F = 1$ . The spin-changing collisions of atoms prepared in  $|F = 1, m_F = 0\rangle$  populate the levels  $|F = 1, m_F = \pm 1\rangle$  with correlated pairs of atoms (green arrows). Depending on the fine-tuning of the dressing and the initial state, various entangled many-body states can be prepared.

which occur for the transitions  $|1(2), 0\rangle \leftrightarrow |2(1), \pm 1\rangle$ , since here the typical frequency width of the MW pulses is too broad to sufficiently suppress the unwanted transition.

Reduced to two hyperfine levels  $a$  in  $F = 2$  and  $b$  in  $F = 1$  with energy difference  $E_a - E_b = \omega_0$ , the Hamiltonian describing the evolution of the atoms while radiated by a MW pulse with frequency  $\omega$  reads

$$H_{MW} = -\delta a^\dagger a + \frac{\Omega_{MW}}{2} \left( e^{-i\phi} b^\dagger a + e^{i\phi} a^\dagger b \right) \quad (3.1)$$

where  $\delta = \omega - \omega_0$  is the detuning,  $\Omega_{MW}$  the Rabi frequency and  $\phi$  the phase of the MW. Throughout this section we set  $\hbar = 1$ . The hats commonly used to note operators are only used in cases where operators could be confused with scalars, as for example in the case of the number operator  $\hat{N}$  and the total atom number  $N$ . Transferring the atoms back and forth between the two levels can also be used to imprint an arbitrary relative phase. As suggested by the Hamiltonian

in Equation 3.1, a relative phase can be imprinted either by changing the phase of the MW field  $\phi$  or by using non-resonant pulses.

The transition frequencies within one hyperfine manifold only differ by the quadratic portion  $q$  of the Zeeman shift, which is much smaller than typical frequency widths. Also the energy separations in both hyperfine manifolds are very similar and only differ slightly due to the value of the  $g$ -factors. Therefore, RF transitions are usually driven in  $F = 1$  and  $F = 2$  simultaneously, if both manifolds are populated. However, one can make use of the opposite sign of the  $g$ -factors and restrict the coupling to one manifold by controlling the rotation direction of the polarisation. This has already been achieved in a similar system, using two orthogonal antennas emitting mainly linear polarisation. Their radiation was matched in amplitude and combined to circular polarisation [97]. Proper adjustment of the relative phase between the linear constituents results either in  $\sigma_+$  or  $\sigma_-$  polarisation and allows to selectively drive transitions in  $F = 1$  or  $F = 2$  only. Restricting the interaction to the  $F = 1$  manifold, the RF coupling can be described by

$$H_{RF} = (q + \delta)a_1^\dagger a_1 + (q - \delta)a_{-1}^\dagger a_{-1} \quad (3.2)$$

$$+ \frac{\Omega_{RF}}{2\sqrt{2}} \left( e^{i\phi} a_0^\dagger a_1 + e^{-i\phi} a_0^\dagger a_{-1} + e^{-i\phi} a_1^\dagger a_0 + e^{-i\phi} a_{-1}^\dagger a_0 \right)$$

where  $\delta$  is again the detuning with respect to the linear Zeeman shift  $p$ ,  $\Omega_{RF}$  the Rabi frequency and  $\phi$  the phase of the RF. The derivation of the above Hamiltonians assumes the rotating-wave approximation (RWA) and is thoroughly presented in [98].

The energy difference of two coupled hyperfine levels can be increased or decreased by red- and blue-detuned coupling, respectively. This MW dressing is used to counteract the asymmetry caused by the quadratic Zeeman shift as depicted by the blue wavy line in Figure 3.2. The shift in the energy is thoroughly explained in references [54, 99] and given by the eigenstates of the coupled system (i. e. dressed states) describing the interaction of a two-level atom and the photons. The effective shift results from the combination of the shift due to the static magnetic field and a shift due to the dressing  $q = q_B + q_{MW}$  with  $q_B = (g\mu_B B)^2 / \Delta E_{hfs}$  [100] and  $q_{MW} = \Omega_{MW}^2 / (2\pi \cdot 4\delta)$  [95] for dressing the clock states.

Unwanted population of spin levels can be removed by light pulses resonant to the  $F = 2$  manifold only. These pulses leave the atoms in  $F = 1$  untouched (as long as a relatively small fraction of atoms is expelled from the ensemble) and are in particular necessary to clean spin levels that should resemble the vacuum state prior to spin dynamics. Also a two-photon light coupling can be employed for a coherent transfer between distinct spin levels. These so-called stimulated Raman processes do not just change the internal spin state but also transfer the atoms to a distinct momentum mode if the laser

beam geometry is chosen accordingly. The stimulated Raman transfers are subject of [Section 5.1](#).

### 3.3 SPIN DYNAMICS

Though ultra-cold and barely moving, the extended wave-function of the atoms in the BEC facilitates occasional collisions. The elastic collisions can either contribute to an effective potential (collisional shift) or, which is the interesting part, also change the spin state of the atoms. Due to the low energy, only s-wave collisions are possible and the orbital angular momentum of the atoms is untouched. Therefore, the conservation of total angular momentum determines the conservation of the spin projection  $\sum m_F^{\text{in}} = \sum m_F^{\text{out}}$ . We focus the discussion of spin dynamics to the  $F = 1$  manifold. Analogue dynamics in  $F = 2$  has been employed in our group to study higher spatial trap modes [90] and to prepare twin-Fock states [54], but will not be covered here.

Within the SMA, incorporating the potential energy due to a static magnetic field, the Hamiltonian describing our BEC in the  $F = 1$  manifold is given by [25, 100, 101]

$$H_{\text{SD}} = -p (\hat{N}_1 - \hat{N}_{-1}) \quad \text{linear Zeeman shift} \quad (3.3a)$$

$$+ q (\hat{N}_1 + \hat{N}_{-1}) \quad \text{quadratic Zeeman shift} \quad (3.3b)$$

$$+ \lambda (\hat{N}_1 - \hat{N}_{-1})^2 \quad \text{collisional shift} \quad (3.3c)$$

$$+ \lambda (2\hat{N}_0 - 1) (\hat{N}_1 + \hat{N}_{-1}) \quad \text{collisional shift} \quad (3.3d)$$

$$+ 2\lambda (a_0^\dagger a_0^\dagger a_1 a_{-1} + a_1^\dagger a_{-1}^\dagger a_0 a_0). \quad \text{spin-changing coll} \quad (3.3e)$$

Here,  $p$  and  $q$  are the linear and the effective quadratic Zeeman shift and  $\lambda$  is an interaction parameter that contains the scattering lengths and the overlap integral of the spatial modes and has, in the case of  $^{87}\text{Rb}$ , negative sign  $\lambda < 0$  [102]. Its scaling with the total atom number is given by  $\lambda \propto N^{-3/5}$  assuming a 3D harmonic trap and the approximate Thomas-Fermi density profile [103]. For completeness, we indicate terms proportional to the so-called magnetisation  $N_1 - N_{-1}$  here. However, for most applications these terms vanish, as the Hamiltonian conserves the magnetisation and the initial states are usually prepared magnetisation-free.

Let us for example prepare a coherent state with all atoms in  $|F = 1, m_F = 0\rangle$  and expose the ensemble to a typical magnetic field of 1 G. The spin-changing collisions will not occur without any additional effort. To initiate the dynamics, the hyperfine levels have to be shifted

by either reducing the magnetic field to less than 300 mG [61] or by employing MW dressing [95]. Let the effective quadratic Zeeman shift be tuned to  $q = -\lambda(2N - 1)$  by either of the methods. In this case, all but the last term 3.3e of the above Hamiltonian vanish initially and the spin dynamics starts off unhindered. This setpoint of  $q$  is called the spin-dynamics resonance. If we restrict the dynamics to large ensembles  $N \gg 1$  and short evolution times, the macroscopic population of the level  $|1, 0\rangle$  is barely changed and we can approximate its population to be fixed such that  $\hat{N}_0 = a_0^\dagger a_0 \approx N$ . The residual Hamiltonian is

$$H_{\text{SD, resonant}} \approx \Omega \left( a_1 a_{-1} + a_1^\dagger a_{-1}^\dagger \right) \quad (3.4)$$

with the spin-dynamics rate  $\Omega = 2\lambda N \propto N^{2/5}$ . Note that the resonant value of  $q$  is  $-\lambda(2N - 1) \approx -2\lambda N = |\Omega|$ . Dynamics under  $H_{\text{SD, resonant}}$  populates  $|1, \pm 1\rangle$  with correlated pairs of atoms and generates the two-mode squeezed vacuum [99]

$$|\psi(t)\rangle = \sum_{n=0}^{\infty} \frac{(-\tanh \Omega t)^n}{\cosh \Omega t} |n\rangle_1 \otimes |n\rangle_{-1}. \quad (3.5)$$

The states  $|n, n\rangle = |n\rangle_1 \otimes |n\rangle_{-1}$  represent Fock states in the modes  $m_F \pm 1$  respectively. Since the occupation number of both modes is perfectly correlated, these states are called twin-Fock states. Within the low-depletion limit, the mean population of the twin-Fock modes grows exponentially,  $\langle N_1 + N_{-1} \rangle = 2 \sinh^2(\Omega t)$ . Off-resonant spin dynamics is slower and possible as long as the energy balance of the spin-changing process is in the boundaries of  $\pm|\Omega|$ .

As typical for quantum dynamics, the spin-changing collisions occur even if they do not seem to strictly obey the energy conservation. The uncertainty in the time scale of the dynamics  $\propto 1/|\Omega|$  sets a limit to the uncertainty of the energy conservation  $\propto |\Omega|$  and explains the width of the resonance. In the middle of the resonance, the dynamics starts fastest with an exponential growth of the population, whereas on the edge of the resonance the damping of the spin dynamics caused by the non-vanishing extra terms in the Hamiltonian becomes apparent. In  $^{87}\text{Rb}$  BECs in our configuration, the spin-dynamics rate  $\Omega$  is usually in the range of  $2\pi \times 10$  Hz, whereas at 1 G magnetic field, the energy of a pair of atoms in the levels  $|1, \pm 1\rangle$  is  $2\pi \times 72$  Hz higher as if the pair sits in the level  $|1, 0\rangle$ , which is much more than  $|\Omega|$  away from the resonance at  $2\pi \times 10$  Hz. Since relevant values of the effective quadratic Zeeman shift are to be found at multiples of  $|\Omega|$  (see Figure 4.1), the value of  $q$  is usually given in units of  $|\Omega|$ . How to determine the spin-dynamics rate  $\Omega$  from measurements and how to calibrate the effective shift  $q$  in the lab is presented in Chapter 4.

## 3.4 ONE HAMILTONIAN, VARIOUS TYPES OF ENTANGLED STATES

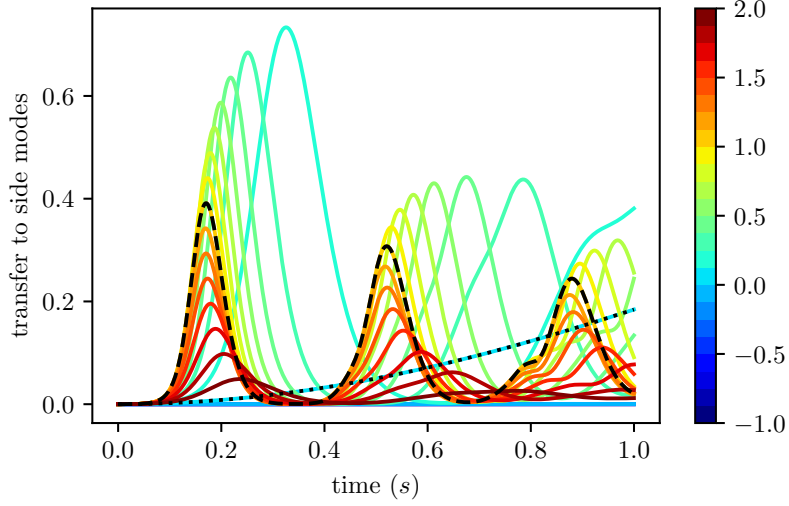
The main feature of spin-changing collisions is not that they coherently transfer atoms from one spin state to the other, this can much faster be done by MW and RF pulses, but that they introduce non-classical correlations among the altered spins. The type of entangled state prepared depends on the spin-dynamics time, the initial spin configuration, the regime of the effective shift  $q$  and the chosen modes to look at.

3.4.1 *Twin-Fock states*

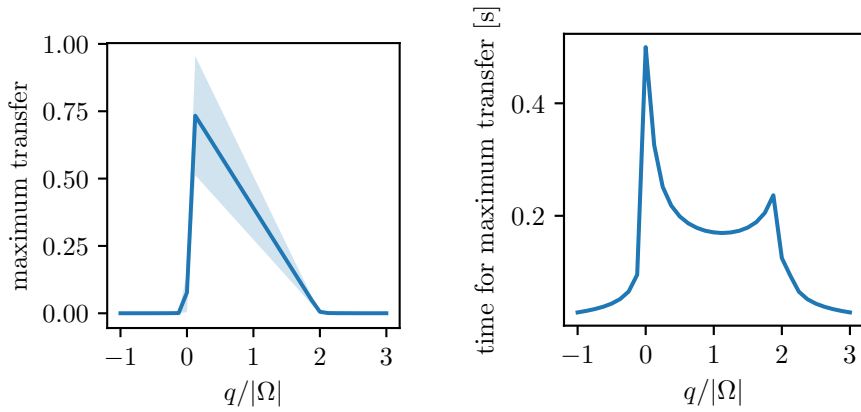
If an atom is created in  $|1, +1\rangle$ , another atom pops up in  $|1, -1\rangle$  (both coming from the infinite reservoir in  $m_F = 0$ ), that is dynamics populates the levels  $|1, \pm 1\rangle$  with correlated pairs of atoms, as one can directly see in Equation 3.4. As the atoms are indistinguishable, it is impossible to predestine which of the atoms possesses which spin. But what is for sure is that if we measure one atom with  $m_F = +1$ , there has to be another atoms with  $m_F = -1$  or vice versa. This twin-Fock state of two atoms is a standard example of an entangled state and resembles the photonic state that has been used in the famous Hong–Ou–Mandel experiment. Depending on the spin-dynamics time, superpositions of such twin-Fock states with different sizes are prepared.

The population of the levels  $|1, \pm 1\rangle$ , i. e. the fraction of atom populating the twin-Fock state, due to evolution under the Hamiltonian 3.3 is shown in Figure 3.3. For the computation, the Schrödinger equation is solved for the exact Hamiltonian matrix form (details see Section A.3.2). As it is shown in Figure 3.3b, the parameter  $q$  affects the maximal fraction of atoms possible to be transferred to the twin-Fock state. The maximal mean transfer by a rapid quench of the value  $q$  is reached close to the edge of the resonance at  $q/|\Omega| \gtrsim 0$ . However, here the spin dynamics is relatively slow and the evolution time that maximises the transfer is very sensitive on  $q$  (see Figure 3.3c). The preparation of twin-Fock states close to  $q = 0$  is experimentally not feasible, since small fluctuations in the magnetic field or the total atom number, and even the typical atom losses during the dynamics, strongly influence the outcome. Working points in the vicinity of the resonance  $q = 1$  are less prone to experimental noise. But even here, the transferred fraction to the twin-Fock modes typically fluctuates uniformly within 0-80% (see Figure 4.5 and Ref. [64]) and further application would require heavy post-selection.

Regarding the application of the twin-Fock state in an interferometer, a large total atom number is favourable to increase the sensitivity limit given by quantum noise. The enhancement due to entanglement comes on top. That is the size of the twin-Fock state for a given size of the BEC should be as large as possible. The transferred fraction to the twin-



(a) Transfer to the twin-Fock modes in time, initiated by a jump to different values of  $q$  (indicated by the different colors). For clarity, the dynamics at  $q = 1$  (dashed line) and at  $q = 0$  (dotted line) are highlighted.



(b) The maximum transfer possible, as a function of the fixed value of  $q$ . The blue shaded area represents the quantum fluctuations (one standard deviation). (c) The evolution time needed to achieve the maximum transfer as a function of  $q$ .

Figure 3.3: Preparation of twin-Fock states by jumping with  $q$  into the vicinity of the spin-dynamics resonance. Simulations executed with  $N = 10^4$  atoms and  $\Omega = 2\pi \cdot 5.1$  Hz, for details see [Section A.3.2](#).



Fock modes can be increased beyond what is shown in [Figure 3.3b](#) by employing a quasi-adiabatic ramp of  $q$  [[64](#)]. This technique was applied within the work of this thesis and is discussed in [Section 4.3](#).

### 3.4.2 Spin-1 Dicke States

The spin-dynamics Hamiltonian can be reformulated with the focus on the Spin-1 character of the system. To this end, the collective spin-1 operator  $\mathbf{L}$  with components

$$L_x = \frac{a_0^\dagger a_1 + a_0^\dagger a_{-1} + a_1^\dagger a_0 + a_{-1}^\dagger a_0}{\sqrt{2}} \quad (3.6)$$

$$L_y = \frac{a_0^\dagger a_1 - a_0^\dagger a_{-1} - a_1^\dagger a_0 + a_{-1}^\dagger a_0}{i\sqrt{2}} \quad (3.7)$$

$$L_z = a_{-1}^\dagger a_{-1} - a_1^\dagger a_1 \quad (3.8)$$

is introduced. The components obey the defining commutation relation for angular momentum operators  $[L_a, L_b] = i\epsilon_{abc}L_c$ . Using the spin-1 operator, the Hamiltonian [3.3](#) can be rephrased as [[101](#)]

$$H = -p(N_1 - N_{-1}) + q(N_1 + N_{-1}) + 2\lambda\mathbf{L}^2 \quad (3.9)$$

with the squared length of the Spin-1 vector  $\mathbf{L}^2 = L_x^2 + L_y^2 + L_z^2$ .

For  $\lambda < 0$  the ground state of the spinor BEC maximises the spin length  $\sqrt{\mathbf{L}^2}$ , that is the single atomic spins tend to align, motivating to call a  $^{87}\text{Rb}$  spinor BEC in  $F = 1$  ferromagnetic. If prepared in  $|F = 2, m_F = 0\rangle$  we have a spin-1 BEC as well (neglecting the  $m_F = \pm 2$  levels due to two orders of magnitude slower spin dynamics), only is the interaction about seven times larger and has opposite sign  $\lambda > 0$  [[54](#)].

Spin-1 Dicke state have been realised experimentally by a quasi-adiabatic ramp of  $q$ . Upon imprinting a phase shift by coupling the three  $m_F$  states with an RF-pulse, these states proved sensitivity beyond the three-mode SQL [[51](#)].

### 3.4.3 Squeezed states

The state shown in [Equation 3.5](#) consists of twin-Fock states, although it is called two-mode squeezed vacuum. Where is the squeezing here? Besides the number squeezing between the modes with  $m_F = \pm 1$ , there is also spin squeezing generated, which can be regarded as a two-mode version of quadrature squeezing. The squeezing action can be seen when changing the basis to symmetric and antisymmetric combinations of the  $m_F = \pm 1$  levels:

$$a_s = \frac{a_{+1} + a_{-1}}{\sqrt{2}} \quad \text{and} \quad a_a = \frac{a_{+1} - a_{-1}}{\sqrt{2}}. \quad (3.10)$$



In this basis, the Hamiltonian 3.4 becomes

$$H_{\text{SD}} \approx \lambda N \left[ \left( a_s^\dagger a_s^\dagger + a_s a_s \right) - \left( a_a^\dagger a_a^\dagger + a_a a_a \right) \right], \quad (3.11)$$

which represents a sum of two textbook squeezing operators. Here, spin squeezing is generated in the symmetric and antisymmetric mode respectively. Within the low-depletion limit, where the level  $|1, 0\rangle$  is not relevantly depopulated, both modes are squeezed independently and with orthogonal squeezing angle. For relatively short evolution times, the preferred view on the state is two-mode squeezed vacuum in the basis  $|\cdot\rangle_s \otimes |\cdot\rangle_a$ , whereas for longer evolution times, the simple squeezing regime is left and one might think of the state as a superposition of twin-Fock states in the basis  $|\cdot\rangle_1 \otimes |\cdot\rangle_{-1}$ .

In principle, squeezed states prepared in the symmetric mode can be transferred to the level  $|1, 0\rangle$  by using a RF  $\pi$ -pulse (which only couples to the symmetric mode and therefore leaves the antisymmetric state behind). Prior to this, the remaining atoms in the  $|1, 0\rangle$  need to be moved, for example to the state  $|F = 2, m_F = 0\rangle$ .

A direct implementation of single-mode squeezing in the clock state could be achieved by choosing the initial state  $|\sim N/2\rangle_1 \otimes |0\rangle_0 \otimes |\sim N/2\rangle_{-1}$ , where the ensemble is coherently split up equally on the levels  $|1, \pm 1\rangle$  by a RF pulse, leaving the vacuum in  $|1, 0\rangle$ . In contrast to the dynamics starting with all atoms in  $|1, 0\rangle$ , here the resonance is found at  $q/|\Omega| = -1$ . For this initial state, the Hamiltonian within the low-depletion limit reduces to a term  $\propto a_0^\dagger a_0^\dagger + a_0 a_0$  and directly resembles the generator of single-mode squeezing.

Retaining the view of the symmetric and antisymmetric mode, we can break up the physical spin-1 system and describe it approximately as two collective pseudospin-1/2 systems. In this way, the squeezed states generated by spin dynamics can be visualised on two generalised Bloch spheres in the basis  $|\cdot\rangle_s \otimes |\cdot\rangle_0$  and  $|\cdot\rangle_a \otimes |\cdot\rangle_0$ , respectively. By using the pseudospin-1/2 operators

$$\begin{aligned} S_x &= \frac{a_0^\dagger a_s + a_s^\dagger a_0}{2}, & A_x &= \frac{a_0^\dagger a_a + a_a^\dagger a_0}{2}, \\ S_y &= \frac{a_0^\dagger a_s - a_s^\dagger a_0}{2i}, & A_y &= \frac{a_0^\dagger a_a - a_a^\dagger a_0}{2i}, \\ S_z &= \frac{a_0^\dagger a_0 - a_s^\dagger a_s}{2}, & A_z &= \frac{a_0^\dagger a_0 - a_a^\dagger a_a}{2}. \end{aligned} \quad (3.12)$$

and omitting the terms proportional to the magnetisation  $N_1 - N_{-1}$ , the Hamiltonian 3.3 rephrases to [25]

$$H_{\text{SD}} = \left( 4\lambda S_x^2 - \frac{2}{3}q S_z \right) + \left( 4\lambda A_y^2 - \frac{2}{3}q A_z \right). \quad (3.13)$$

Here, the dynamics can be understood as an interplay of shearing around the  $x$  ( $y$ ) axis and a  $q$ -dependent rotation around the  $z$  axis

on the symmetric (antisymmetric) Bloch sphere. Note that the symmetric and the antisymmetric subspaces are not independent, i. e. the respective spin operators  $S$  and  $A$  do not commute with each other. Furthermore, these two subspaces are the only that exhibit squeezing [61, 98]. A similar Hamiltonian was realised in a two-component BEC and named twist-and-turn squeezing. For  $q/|\Omega| = 0$ , the rotations around  $z$  vanish and only the nonlinear spin terms  $\propto S_x^2$  and  $\propto A_y^2$  remain. This resembles the one-axis twisting (OAT) Hamiltonian, proposed in the early 90s as one of two Hamiltonians to generate spin squeezing [20].

As we discussed in Section 3.3, the generation of entangled pairs of atoms in  $|1, \pm 1\rangle$  starts fastest at  $q/|\Omega| = 1$ . With  $q$  set to this resonance, the Hamiltonian 3.3 rewrites as

$$H_{\text{SD}} = 2\lambda \left[ (S_x^2 - S_y^2) - (A_x^2 - A_y^2) \right] \quad (3.14)$$

which resembles two-axis countertwisting (TACT), the second way to prepare spin-squeezed states originally proposed. Similar to OAT, the squeezing in the two subspaces is orthogonally aligned. TACT is well known to establish substantial squeezing faster compared to the OAT dynamics. The twist-and-turn dynamics can be understood as the intermediate regime. Another characteristic of TACT is that the direction of squeezing is stable during the dynamics, whereas the squeezing ellipse rotates in the case of OAT and twist-and-turn dynamics.

#### 3.4.4 Further applications in state engineering

Spin dynamics can also be utilised to prepare states beyond the squeezing regime and other than Dicke states.

The twist-and-turn dynamics has been employed to realise non-gaussian states beyond the squeezing regime [59, 97]. If the regime of Gaussian states is left, observing the mean population imbalance at the output of an interferometer is not sufficient anymore to make use of the full entanglement-enhanced sensitivity. In fact, highly over-squeezed states eventually are less sensitive compared to CSS' when only incorporated in terms of the standard squeezing parameter. Therefore, the direct application of non-Gaussian states in entanglement-enhanced interferometry demands well-suited and experimentally feasible observables, as it was found to be the variance for the twin-Fock state [63].

So far, we examined cases where all atoms are initially prepared in the level  $m_F = 0$  and the levels  $m_F = \pm 1$  are empty (vacuum) or vice versa. A coherent transfer of a few atoms to  $|1, \pm 1\rangle$  before the spin dynamics does alter the generated states. A few of such seed atoms cause the states in the basis  $|\cdot\rangle_1 \otimes |\cdot\rangle_{-1}$  to deviate from clean twin-Fock states, since the levels  $m_F = \pm 1$  are not solely populated by

correlated pairs anymore. The prepared states can be regarded as in-between a twin-Fock and a squeezed state. These intermediate states are more robust regarding detection-noise than the twin-Fock state and can show an improved metrological gain compared to squeezed states [104].

Spin dynamics can also be used to implement protocols that employ effectively reversed dynamics to increase the noise-robustness of an entanglement-enhanced interferometer [105]. Here, spin dynamics is not only used to prepare a squeezed input state, but also to unsqueeze the state after the interferometric phase imprint while simultaneously amplifying the phase signal. The ideal entanglement-enhanced sensitivity is retained, because the signal-to-(quantum)noise ratio is kept constant during the unsqueezing process. In the case of technical noise in the detection, the sensitivity is improved since the final state resembles a CSS or even an anti-squeezed state which provides outcome distributions much less prone to detection noise. An equivalent protocol was proposed in the notion of so-called SU(1,1)-interferometers [106], which extended an existing time-reversal protocol [107] to increase absolute sensitivity and achieve detection-noise robustness. Furthermore, protocols along this line of thought allow to harness the metrological gain of non-Gaussian states [108] and have been realised without the need to measure more complex observables than the mean population and variances [109].

In relatively recent approaches, the parameter  $q$  is not rapidly quenched to a fixed value but changed during spin dynamics. This can either be done adiabatically [110] or, as mentioned above and discussed in Chapter 4, quasi-adiabatically [47, 64, 111]. The latter was implemented to prepare a major fraction of the ensemble in a twin-Fock state. Depending on the final value of  $q$ , different ground states of the system could be prepared, which include a superposition of highly entangled NOON-states at  $q/|\Omega| = 0$  [88]. The value of  $q$  can also be changed in a staircase-like manner to prepare squeezed states that, for a specific value of  $q$ , represent the ground state of the system and will therefore be stationary in time [112, 113].

It seems experimentally feasible that even more exotic and highly entangled atomic states will be prepared within spin-1 BECs in the near future. Their actual application to interferometry will demand protocols that are robust to typical experimental noise and probably will be optimised to the specific use case.



## PRECISE CONTROL OF SPIN DYNAMICS FOR THE GENERATION OF TWIN-FOCK STATES

---

The Hamiltonian of our quantum system contains three parameters which can all be adjusted in the lab, namely the total atom number  $N$ , the effective quadratic Zeeman shift  $q$ , and the spin-dynamics rate  $\Omega$ . The total atom number is set by tuning the minimum potential of the dipole trap during the evaporation as described in [Section 3.1](#) and typically shows relative fluctuations of 10 %. Within this chapter, the experimental methods to precisely determine the effective quadratic Zeeman shift  $q$  and the spin-dynamics rate  $\Omega$  are presented. The control of  $q$  is then applied to realise a quasi-adiabatic preparation of twin-Fock states.

### 4.1 CALIBRATION OF THE EFFECTIVE QUADRATIC ZEEMAN SHIFT

The effective quadratic Zeeman shift  $q = q_B + q_{MW}$  is varied by changing the power of the [MW](#) dressing field working at a fixed magnetic field of 0.73 G. The power of the [MW](#) source is controlled using a frequency mixer and feeding the second input with a variable DC voltage (details about the [MW](#) source in Ref. [\[54\]](#)). This DC voltage is the output signal of a proportional-integral (PI) controller that realises a power stabilisation. The setpoint voltage of the PI controller is adjusted by the experiment computer to allow for temporal control of the [MW](#) power.

Compared to earlier work [\[64\]](#), the experimental method to calibrate the parameter  $q/|\Omega|$  is extended. We measure the voltage for the five characteristic values  $q/|\Omega| = \{-2, -1, 0, 1, 2\}$  and then fit the resulting points to get  $q/|\Omega|$  as a function of the voltage that sets the [MW](#) power.

[Figure 4.1](#) shows the single measurements from which the calibration is obtained. All measurements follow a similar scheme. An initial spin configuration in  $F = 1$  is prepared and then the [MW](#) dressing field is switched on with a variable power for a fixed duration. During this time, spin dynamics might be enabled to transfer atoms between the levels  $|1, 0\rangle$  and  $|1, \pm 1\rangle$ . After the dynamics, the population of the three spin levels is measured. For a determination of  $q/|\Omega| = 2$ , the [BEC](#) is prepared in the level  $|1, 0\rangle$  and the [MW](#) dressing is applied for 90 ms. A certain set voltage marks the threshold where spin dynamics starts, and corresponds to the [QPT](#) from the polar phase to the phase of broken axisymmetry [\[87\]](#). For the initial population in  $|1, 0\rangle$ , the resonance  $q/|\Omega| = 1$  is marked by a maximal transfer to  $|1, \pm 1\rangle$ , here

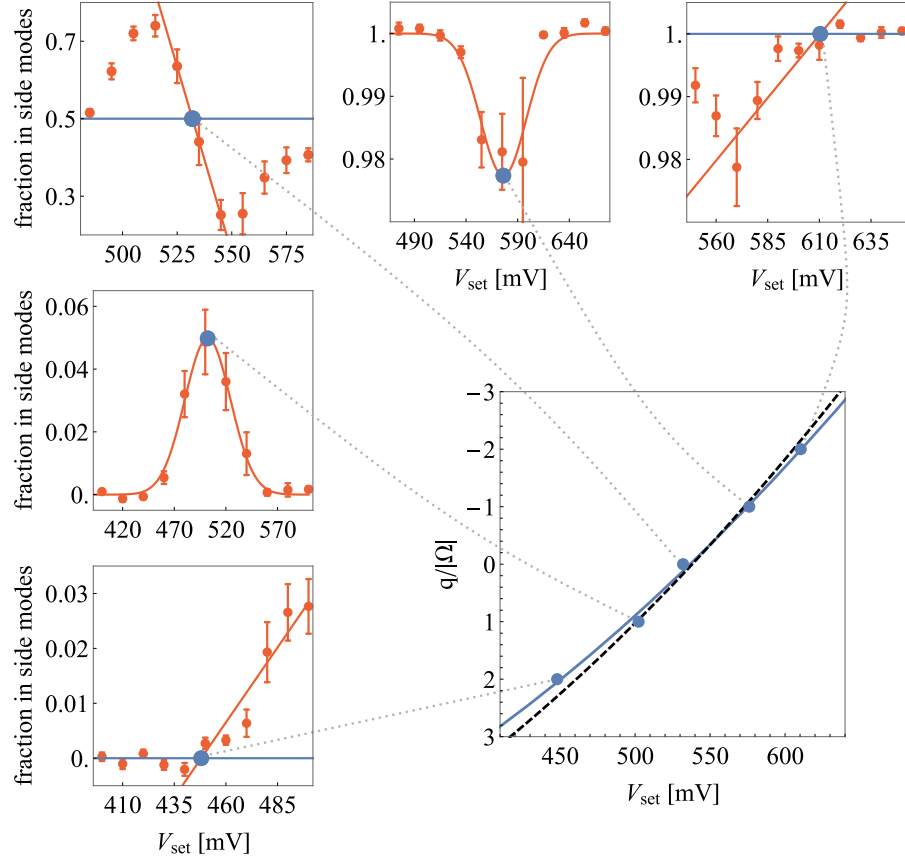


Figure 4.1: Calibration of the effective quadratic Zeeman shift  $q$ . For the calibration of  $q$ , five independent measurements determine the position of characteristic  $q/|\Omega|$  values (details see text). From these,  $q/|\Omega|$  as a function of the voltage which sets the dressing MW power is obtained by a fit. The fit can also be used to determine the value of the spin-dynamics rate, which gives  $\Omega = 2\pi \times 5.6(2)$  Hz (blue solid line). If the value of  $|\Omega|$  is for example extracted from the  $q/|\Omega| = 1$  resonance scan, the calibration changes slightly (black dashed line). For this calibration, the data was post-selected to a mean atom number of  $\langle N \rangle = 10^4$ . Figure has been partially published in Ref. [47].

after a fixed duration of 110 ms. For this measurement to be particularly precise, an initial seed population should be avoided and the mean transfer to  $|1, \pm 1\rangle$  should not exceed 10%. To determine the set voltage that corresponds to  $q/|\Omega| = 0$ , the condensate is prepared with 50% of the atoms in  $|1, 0\rangle$  and 25% in each level  $|1, \pm 1\rangle$  via a resonant RF coupling. For  $q/|\Omega| \gtrsim 0$ , the atoms tend to be predominantly transferred to  $|1, \pm 1\rangle$ , whereas for  $q/|\Omega| \lesssim 0$  the population evolves towards  $|1, 0\rangle$ . Directly at  $q/|\Omega| = 0$ , the population remains stationary. Here, the chosen evolution time is 60 ms. The signal for the  $q = 0$  measurement strongly depends on the chosen evolution time, as here the spin dynamics causes relatively fast oscillations of the state population. The negative values  $q/|\Omega| = -2$  and  $q/|\Omega| = -1$  are

investigated equivalently to their positive counterparts, but with the initial condensate prepared symmetrically in  $|1, \pm 1\rangle$  and an empty level  $|1, 0\rangle$ .

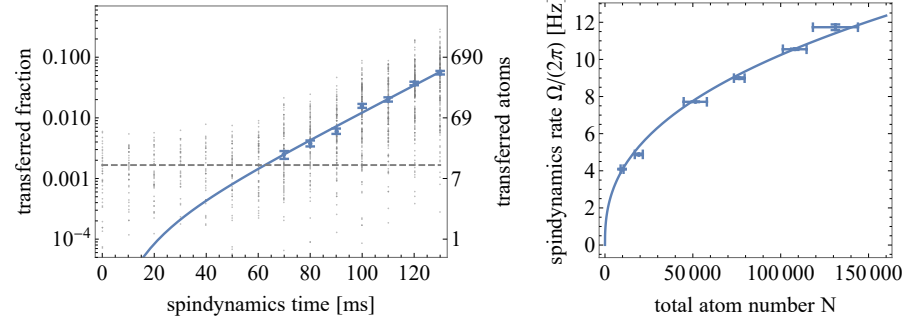
The five measured points are then fitted with the expected functional dependence on the set voltage (details see [Section A.2](#)). Here,  $\Omega$  can be a free parameter determined by the fit, which leads to the calibration  $q/|\Omega| = 6.8 - 23.5 \cdot V_{\text{set}}^2/[V^2]$  with  $\Omega = 5.6(2)$  Hz (blue solid line in [Figure 4.1](#)). If  $\Omega$  is determined independently, for example by extracting it from the  $q/|\Omega| = 1$  resonance scan, the calibration results into  $q/|\Omega| = 7.5 - 25.9 \cdot V_{\text{set}}^2/[V^2]$  with  $\Omega = 5.07(3)$  Hz. The given errors are only statistical errors from the respective fit. As discussed in the following section, alternative (and more convenient) methods to determine the spin-dynamics rate  $\Omega$  can be more precise but less accurate, as they tend to slightly underestimate the absolute value. Therefore, extracting the spin-dynamics rate from the fit that is used to calibrate  $q$  (blue line in [Figure 4.1](#)) is the preferable method. If the  $\pi$ -pulse time of the dressing MW field is precisely characterised, the spin-dynamics rate is the only remaining fit parameter and thus a useful by-product from the calibration of  $q$ .

#### 4.2 DETERMINING THE SPIN-DYNAMICS RATE

In [Section 3.3](#), the spin-dynamics rate  $\Omega$  was defined in the context of the low-depletion approximation  $\hat{N}_0 \approx N$  and for resonant dynamics  $q/|\Omega| = 1$ . In this setting, the spin-dynamics rate  $\Omega$  determines the initial exponential growth of the population in  $|1, \pm 1\rangle$  as  $\langle N_1 + N_{-1} \rangle = 2 \sinh^2(\Omega t)$ .

[Figure 4.2a](#) shows an exemplary measurement of the growing population in  $|1, \pm 1\rangle$ . The spin-dynamics rate is extracted by a fit of the mean transferred fraction which in this case for  $\langle N \rangle = 9700$  atoms gives  $\Omega = 2\pi \times 4.09(2)$  Hz. To avoid an underestimation of the spin-dynamics rate, the mean transfers used for the fit are cut at both ends. A threshold set by the detection noise sets a lower limit. Also mean relative transfers beyond  $\sim 5\%$  are discarded, because at this point the dynamics generally starts to leave the low-depletion approximation.

Still, this method tends to slightly underestimate the spin-dynamics rate due to fluctuations in the total atom number and the magnetic field. Fluctuations in the MW dressing power or frequency have a similar effect as magnetic field fluctuations and are relatively small. A fluctuating atom number directly causes fluctuations of  $\Omega$ , which are in first order symmetric. But also, the atom number affects the collisional shift  $\propto 2\lambda N$  which has to be compensated for resonant spin dynamics. Here, atom number fluctuations to either side cause a deviation from the resonance and thereby a slower initial growth of the population in  $|1, \pm 1\rangle$ . Magnetic field fluctuations show the same effect by directly varying the value of  $q$ .



(a) Determining the spin-dynamics rate  $\Omega$  from a fit of the initial exponential growth of the population in  $|1, \pm 1\rangle$ . Here,  $\Omega = 2\pi \cdot 4.09(2)$  Hz for a mean atom number of  $\langle N \rangle = 9700$  with 8% relative fluctuations. Mean transfers below a threshold set by the detection noise (grey dashed line) and beyond  $\sim 0.05$  are discarded.

(b) Spin-dynamics rate  $\Omega$  as a function of the total atom number complies with the expected scaling, here  $\Omega(N)/(2\pi) = 0.1021 \cdot N^{2/5}$ .

Figure 4.2: Measurement of the spin-dynamics rate  $\Omega$  and verification of  $\Omega \propto N^{2/5}$ . On resonance, that is at  $q/|\Omega| = 1$ ,  $\Omega$  can be determined from fitting the initial exponential growth of the population of the twin-Fock modes with  $f(\Omega, t) = 2 \sinh^2(\Omega t) / \langle N \rangle$ . Repeating this measurement for larger ensemble sizes shows the expected scaling. Here, large total atom numbers must be corrected for a nonlinearity in the detection, which otherwise causes a relevant underestimation of the ensemble size for atom numbers exceeding  $N \approx 2 \cdot 10^4$ .

The data in [Figure 4.2b](#) verifies the expected scaling of the spin-dynamics rate with the total atom number. Here, the different measurements have been recorded over several weeks, demonstrating a reasonable stability of the interaction parameter  $\lambda$  (see [Section 3.3](#)) in our experiment. This means the dipole trap is relatively stable and does not cause major drifts of the spatial modes or trap frequencies.

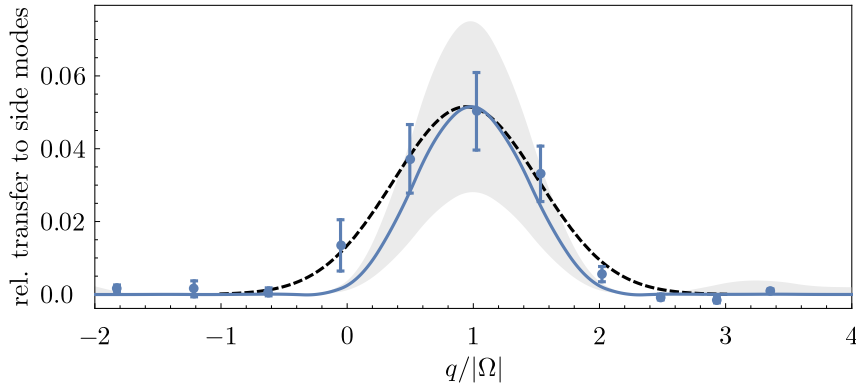
Alternatively, the value of the spin-dynamics rate can already be extracted from a resonance scan, which is a measurement that has to be done previous to an experiment that involves spin dynamics anyway. Here, the spin-dynamics rate can be calculated from the maximum mean transfer to  $|1, \pm 1\rangle$ , which is obtained by a Gaussian fit to the measured data (dashed black line in [Figure 4.3a](#)). For relatively small transfers,  $\Omega$  can be simply calculated by the analytic formula

$$\Omega = \operatorname{arcsinh} \left( \sqrt{\langle N_1 + N_{-1} \rangle_{\max} / 2} \right) / t_{\text{sd}} \quad (4.1)$$

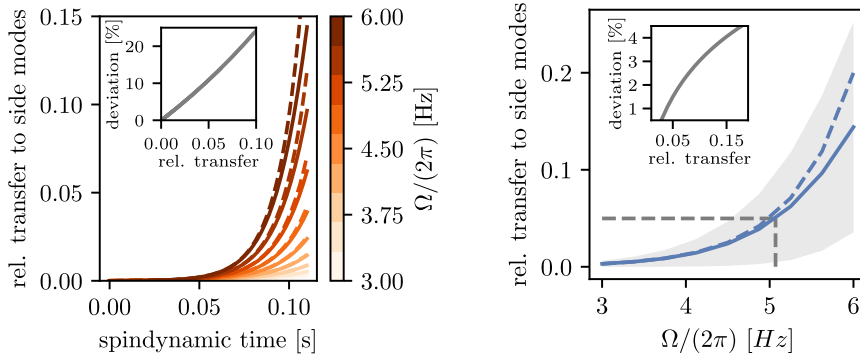
which gives  $\Omega = 2\pi \cdot 5.0(1)$  Hz. Here, the error is mainly due to error propagation of the fluctuations of the total atom number.

[Figure 4.3b](#) depicts the initial exponential growth and the deviation of the full quantum simulation (solid lines) from the analytical results within the low-depletion limit. The inset shows the relative deviation





(a) Resonance scan with  $t_{\text{SD}} = 110$  ms post-selected for a mean atom number of  $\langle N \rangle = 10^4$  with 10 % relative fluctuations. A parameter-free simulation (mean and quantum fluctuations as solid blue line and grey area) predicts a slightly narrower resonance. The deviation is explained by the fluctuations of the total atom number. The maximum transfer obtained from a Gaussian fit (black dashed line) can be used to estimate the spin-dynamics rate  $\Omega$ .



(b) Exponential growth of the transferred fraction for different  $\Omega$ . The analytical low-depletion limit (dashed lines) and the full quantum simulation (solid lines) is shown. The relative deviation between both grows roughly linearly with the transfer to  $|1, \pm 1\rangle$ .

(c) Transfer at  $t_{\text{SD}} = 110$  ms as a function of  $\Omega$ . The maximum transfer obtained in (a) can be used to estimate  $\Omega$  either by using the analytical formula (dashed blue line) or by comparison with the simulation (solid blue line). The inset shows the deviation of both procedures.

Figure 4.3: Extracting  $\Omega$  from the mean maximum transfer of a resonance scan. The data is fitted with a Gaussian to extract the maximum mean transfer which is used to estimate  $\Omega$ . Using the analytical formula, the extracted spin-dynamics rate is  $\Omega = 2\pi \times 5.00(3)$  Hz, whereas comparison with the simulation gives  $\Omega = 2\pi \times 5.07(3)$  Hz (uncertainty given by error propagation starting with the statistical error of the Gaussian fit).

between the analytic approximation and the simulation. The estimation of  $\Omega$  is visualised in Figure 4.3c. The maximum transfer obtained from the Gaussian fit in Figure 4.3a is mapped onto a value for  $\Omega$  (grey dashed lines). The inset shows the relative deviation of the extracted spin-dynamics rate if the analytic formula in Equation 4.1 is used

compared to the full quantum simulation. For the data evaluated here, the results differ by 1.5%. For a deviation below 1%, the maximum relative transfer to  $|1, \pm 1\rangle$  must not exceed 0.04.

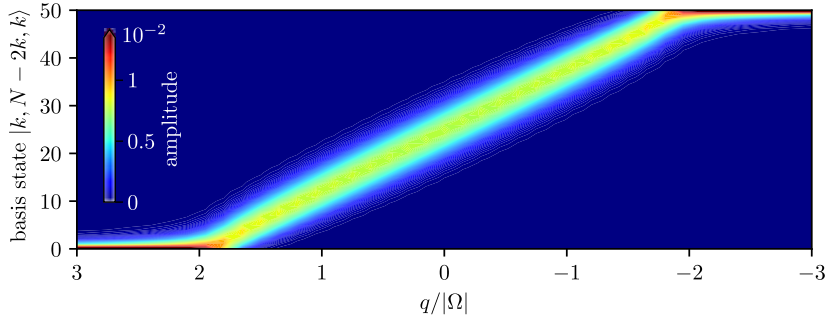
Both methods presented here to measure  $\Omega$  tend to systematically underestimate the spin-dynamics rate. Using the full  $q$  calibration in [Figure 4.1](#) to determine  $\Omega$  is expected to achieve a better accuracy, since the position of the characteristic  $q/|\Omega|$  values is expected to fluctuate symmetrically under fluctuations in the total atom number or in the magnetic field. Therefore it seems reasonable, that the value extracted from the full calibration of  $q/|\Omega|$  is larger than the value extracted from the resonance scan only (both use the same data set and are directly comparable). Alternatively, the spin-dynamics rate has also been extracted from a comparison of the measurement that determines  $q/|\Omega| = 2$  (see [Figure 4.1](#)) with parameter-free simulations [[110](#)]. In our case, this would involve a thorough characterisation of the [MW](#) dressing. However, the achieved accuracy in determining  $q$  and  $\Omega$  is sufficient for the desired level of control over the system and allows to adequately predict the outcome for evolution times up to seconds as presented in the following section.

### 4.3 PREPARATION OF TWIN-FOCK STATES BY A QUASI-ADIABATIC Q-RAMP

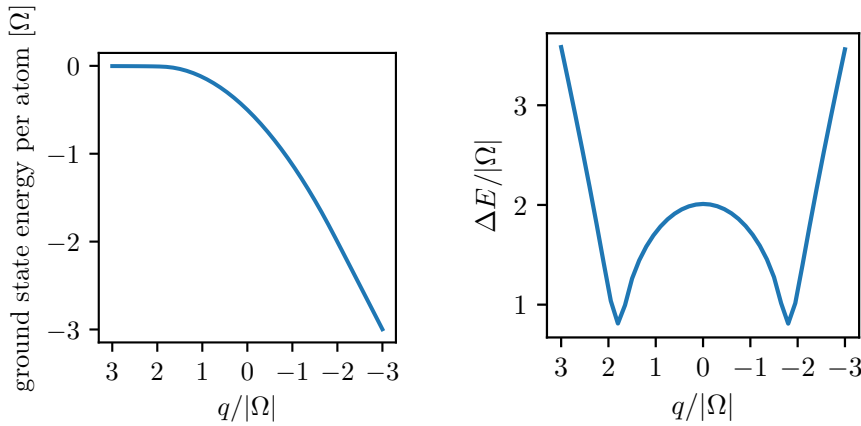
The experimental control over  $q$  is utilised to implement a quasi-adiabatic preparation of twin-Fock states as proposed by Zhang and Duan [[86](#)]. In contrast to initiating the spin dynamics by rapidly setting a fixed  $q$  in the vicinity of the resonance, here,  $q$  is changed slowly, such that the many-body state unexcitedly follows the ground state of the system. From the system's Hamiltonian in [Equation 3.3](#), one can read that  $q$  affects the energy of atoms in the levels  $|1, \pm 1\rangle$ . At large positive  $q$ , atoms that populate  $|1, \pm 1\rangle$  contribute to a higher energy, therefore the initial preparation of all atoms in the level  $|1, 0\rangle$  represents the ground state. For large negative  $q$ , however, a population of the levels  $|1, \pm 1\rangle$  decreases the energy and the ground state therefore completely populates these. Since the interaction that transfers the atoms back and forth is symmetric in  $m_F = \pm 1$ , only a symmetric population of the levels  $|1, \pm 1\rangle$  can be reached (assuming initial zero magnetisation).

[Figure 4.4a](#) visualises the system's ground state as a function of  $q/|\Omega|$ . The colorscale represents the composition of the ground states in terms of the basis states  $|k, N - 2k, k\rangle = |k\rangle_{-1} \otimes |N - 2k\rangle_0 \otimes |k\rangle_1$ . For  $q/|\Omega| \geq 2$ , the ground state mainly populates the level  $|1, 0\rangle$ , and the energy thus becomes independent of the effective quadratic Zeeman shift (see [Figure 4.4b](#)). In the range  $2 \geq q/|\Omega| \geq -2$ , the population of levels  $|1, \pm 1\rangle$  increases linearly towards the state  $|N/2, 0, N/2\rangle$ .

The adiabatic theorem states that a quantum system will remain in its many-body ground state upon a very slow change of an external



(a) Population of the twin-Fock modes for the many-body ground state at different values of  $q$ . If the state  $|0, N, 0\rangle$  is prepared at a large positive  $q$ , the state  $|N/2, 0, N/2\rangle$  can be reached by adiabatically ramping  $q$  towards negative values.



(b) The energy per atom in the many-body ground state. For large positive  $q$ , the ground-state energy becomes stationary.

(c) The energy gap between the ground state and the first excited state closes around  $q = \pm 2$ , which mark the ground-state QPTs of the system.

Figure 4.4: Characteristic of the system's many-body ground state as a function of  $q/|\Omega|$ . Here  $N = 100$ . The energy gaps decrease with the total number of atoms as  $\Delta E \propto N^{-1/3}$  [86].

parameter like  $q$  [114]. Therefore, if the BEC is prepared in  $|0, N, 0\rangle$  and  $q$  is adiabatically changed from positive to negative values, all atoms could be prepared in a twin-Fock state. As a measure of adiabaticity, one can use the probability to find the final state still in the ground state of the system  $|\langle \psi_{ground} | \psi_{final} \rangle|^2$ . The smaller this quantity, the less adiabatic was the procedure. Figure 4.4c shows why adiabaticity is hard to fulfil on the way from positive to negative  $q/|\Omega|$ . The energy gap between the ground state and the first excited state  $\Delta E$  becomes small at  $q/|\Omega| = \pm 2$ , and therefore the time interval of a change in  $q$  must be large if adiabaticity should hold. In other words, the rate of change of  $q$  must be particularly small around the closing energy gaps. These two characteristic points are recognised as ground-state QPTs of the system, which come along with a high density of states, i. e. the

energy gaps to higher excited state become small as well. Thus, rapidly crossing a QPT typically causes a population of a large spectrum of excited states. For an adiabatic procedure, no excited states should be populated at the end of the ramp. To meet this condition with an ensemble of  $N = 10^4$  atoms, a ramp over the range  $2 \gtrsim q/|\Omega| \gtrsim -2$  must at least be 20 s long. This exceeds the measured lifetime of our BEC,  $\tau = 6.3$  s, by a factor of more than three and would cause the  $N = 10^4$  atoms to be reduced to only  $4 \times 10^3$  at the end of the procedure. Even though an adiabatic crossing that exceeds the ensemble's lifetime by a factor of two has been successfully demonstrated [110], the loss of such a large fraction of atoms strongly reduces the entanglement, and should be avoided regarding an application of the state for entanglement-enhanced interferometry.

Therefore, a quasi-adiabatic parameter ramp was implemented, where only about the lowest 20 % of excited states are populated (compare [64]). Figure 4.5 (a) shows the employed combination of four linear ramps in  $q/|\Omega|$  to allow for a particularly slow rate of change in the vicinity of the QPTs. Within 120 ms,  $q$  is ramped quickly to  $q/|\Omega| = 2.2$  and then the QPT at  $q/|\Omega| = 2$  is passed slowly within 350 ms. In between the two phase transitions, the ramp speed is slightly increased again. A simulation using the experimental parameters shows that during the quasi-adiabatic ramp, the state of the system oscillates around the ground state (compare Figure 4.4 (a) and Figure 4.5 (b)). This causes an oscillation of the mean transferred fraction which reaches values close to its maximum already before crossing the second QPT at about  $q/|\Omega| = -1.8$ . The amplitude and period of the oscillation can be regarded as a measure of how adiabatic the first QPT was crossed. The slower the rate of change of  $q$ , the smaller becomes the amplitude and the oscillation period, until the system directly follows the ground state at perfect adiabatic conditions.

The distribution of the final fraction of atoms transferred into the twin-Fock state is shown in Figure 4.5 and yields a transfer of 93(5) % (blue histogram in (c)). The mean and the fluctuations of the transfer are adequately predicted by solving the full quantum evolution using experimentally determined parameters only (details see Section A.3.2). However, the predicted distribution (cyan curve in Figure 4.5 (c)) shows a sharp peak at a fraction of about 0.85, which is much less distinct in the measured data. This could be explained by the fluctuating total atom number, which is not incorporated into the simulation, but causes the distinct peak to move and thereby to smear out.

With longer ramping durations, even higher transfer efficiencies can be achieved. However, in this case also the final number of atoms is further reduced by the typical atom loss. Additionally, we observe decoherence of the prepared twin-Fock states after extended holding times, resulting in weaker entanglement detection. The overall preparation yields a total of  $\langle N \rangle = 9300$  atoms with only 10 % relative

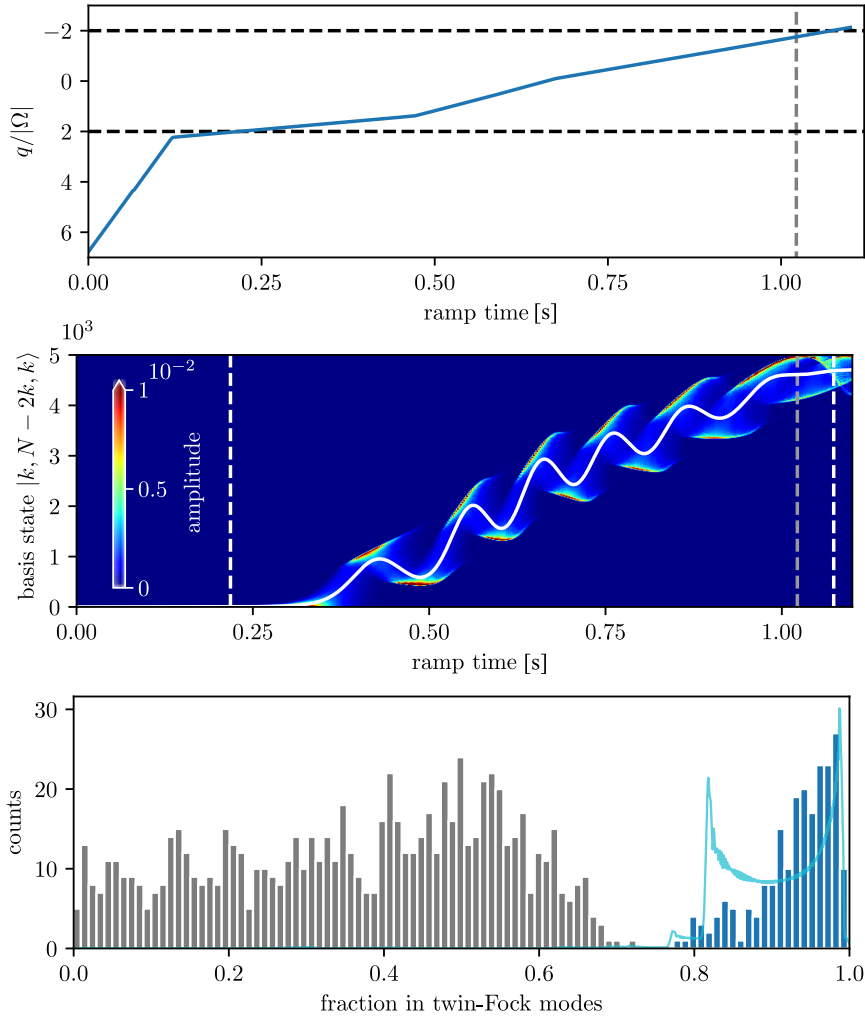


Figure 4.5: Results of the implemented quasi-adiabatic  $q$  ramp. The quasi-adiabatic parameter ramp (see (a), blue line) was experimentally optimised to achieve a stable population of the twin-Fock modes well above 70%. In (b) the QPTs are marked by the white dashed lines. Stopping just before the second QPT at  $q \approx -1.7$  (grey dashed line) reduces the total ramp time without significantly decreasing the transfer efficiency. The simulation based on the actual experimental parameters shows which basis states  $|k, N - 2k, k\rangle$  comprise the many-body state during the evolution. The mean population of the twin-Fock modes (white solid line) oscillates towards a maximum of 94(5)%. For the end of the implemented ramp, the simulation predicts a transfer of 92(6)%. In (c), the measured population of the twin-Fock modes (blue histogram) reaches 93(5)%, which agrees fairly well with the prediction (cyan curve) regarding the mean and the fluctuations. The details of the outcome distributions, however, deviate. For comparison, the measured population of the twin-Fock modes after a quench to  $q/|\Omega| \approx 1$  is shown (grey histogram).

fluctuations, which are predetermined by the typical fluctuations of the initial size of the BEC in our apparatus. For comparison, a typical measurement outcome after a rapid quench into the vicinity of the resonance  $q/|\Omega| \approx 1$  is shown. The quasi-adiabatic procedure clearly overcomes the limited transfer to the twin-Fock modes by the usual rapid quench. For the successive application of momentum kicks by stimulated Raman transitions, the remaining atoms in  $|F = 1, m_F = 0\rangle$  can be transferred to  $|F = 2, m_F = 0\rangle$  and be removed by resonant light. After this cleaning procedure, we observe no major degradation of the remaining twin-Fock states if less than 30% of the atoms are expelled. This requirement is fulfilled by the quasi-adiabatic state preparation without the need of post-selection. Hence, this method provides a clean twin-Fock state in two spin levels, well-suited for the subsequent transfer to momentum space.

## TRANSFER TO DISTINCT MOMENTUM MODES

The application of entangled states in inertially sensitive light-pulse atom interferometers demands entanglement between two distinct momentum modes. To employ the twin-Fock states  $|N/2\rangle_{+1} \otimes |N/2\rangle_{-1}$  as presented in [Section 4.3](#), a transfer of the entanglement from the internal spin degree of freedom to the external motional degree of freedom has to be realised. To this end, highly effective stimulated Raman transitions have been implemented to achieve a spin-dependent momentum transfer to the free-falling BEC. The reduction of the ensemble's free expansion ensures a stable momentum transfer and enables a final detection beyond the atomic shot-noise. Finally, the measurement of a generalised squeezing parameter verifies entanglement between the atoms in the distinct momentum modes. As atom loss is decremental for entangled states and technical noise easily dominates the sub-shot-noise fluctuations, the protocol demands a low-noise Raman transition with near 100 % transfer efficiency. The main results presented in [Section 5.2](#) and [Section 5.3](#) have been published in Ref. [47].

## 5.1 RAMAN TRANSFER

In Rubidium, one-photon transitions between stable states that do not spontaneously decay are only available in the MW regime. As the photon momentum transferred by a MW transition is three orders of magnitude smaller than the typical velocity distributions of the freely expanding BECs, and thus negligible, an optical transition has to be used to transfer substantial momentum.

The population of short-lived states can be avoided by employing a two-photon light coupling of two hyperfine levels in the electronic ground state  $5^2S_{1/2}$  via a detuned intermediate level of the excited electronic state  $5^2P_{3/2}$ . For this process, the atoms interact with the light from two lasers with different but phase-locked frequencies. Assuming a transfer of the atom from one hyperfine level  $|g\rangle$  to another hyperfine level  $|e\rangle$ , a photon with frequency  $\omega_1$  is absorbed, followed by stimulated emission of a photon with frequency  $\omega_2$ . Due to a large detuning  $\Delta$  to the hyperfine levels in  $5^2P_{3/2}$ , no intermediate state is populated and the transfer does not suffer from spontaneous decay<sup>1</sup>. Such a stimulated Raman transition is schematically depicted in [Figure 5.1](#).

<sup>1</sup> With ensembles of  $N = 10^4$  atoms and laser parameters as used for the experiments presented here, we estimate about 10 photons to be spontaneously emitted during a Raman  $\pi$ -pulse.

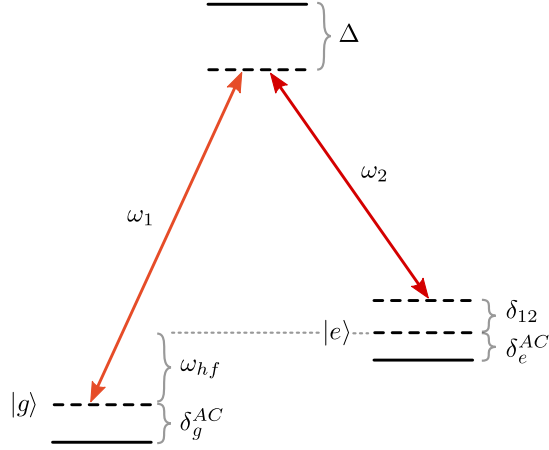


Figure 5.1: Sketch of the Raman coupling scheme. Two phase-locked laser frequencies  $\omega_1$  and  $\omega_2$  drive a stimulated two-photon transition between two hyperfine levels. A large detuning  $\Delta$  suppresses a population of the intermediate level. The difference of both laser frequencies  $\omega_1 - \omega_2$  might be detuned by  $\delta_{12}$  with respect to the hyperfine transition  $\omega_{\text{hf}}$ . The AC-stark effect shifts both levels and causes additional detunings  $\delta_g^{\text{AC}}$  and  $\delta_e^{\text{AC}}$ . In our specific realisation in  $^{87}\text{Rb}$ ,  $|g\rangle = |5^2S_{1/2}; F = 1, m_F = 0\rangle$ ,  $|e\rangle = |5^2S_{1/2}; F = 2, m_F = 0\rangle$ , and the intermediate level is  $|5^2P_{3/2}; F' = 1\rangle$ .

The Raman transfer is implemented on the clock states of  $^{87}\text{Rb}$ , i. e.  $|g\rangle = |F = 1, m_F = 0\rangle$  and  $|e\rangle = |F = 2, m_F = 0\rangle$ . In addition to the desired detuning  $\Delta \approx 1 \text{ GHz}$  to the intermediate level, the transfer is affected by a common detuning of the laser frequencies  $\delta_{12}$  and the AC-Stark shifts of the states  $\delta_g^{\text{AC}}$  and  $\delta_e^{\text{AC}}$  respectively. Neglecting a change of the momentum state for now, the detuning  $\delta_{12} = (\omega_1 - \omega_2) - \omega_{\text{hf}}$  is the combined detuning of the laser frequencies from the hyperfine splitting  $\omega_{\text{hf}} \approx 2\pi \cdot 6.834 \text{ GHz}$ . The AC-Stark shift is caused by the red-detuned one-photon coupling of the intermediate state with the states  $|g\rangle$  and  $|e\rangle$  with the frequencies  $\omega_1$  and  $\omega_2$  respectively. The compensation of the relative AC-Stark shift  $\Delta^{\text{AC}} = \delta_e^{\text{AC}} - \delta_g^{\text{AC}}$  is crucial for a robust Raman transfer and discussed in [Section 5.1.2](#).

The two-photon coupling results in a coherent oscillation of the population of the two states  $|e\rangle$  and  $|g\rangle$ , similar to the one-photon coupling of a two-level system. The population of the state  $|e\rangle$  is given by

$$P_e = \frac{\Omega_0^2}{\Omega_{\text{eff}}^2} \sin^2 \left( \frac{\tau \Omega_{\text{eff}}}{2} \right) \quad (5.1)$$

where  $\tau$  is the Raman pulse duration and

$$\Omega_{\text{eff}} = \sqrt{\Omega_0^2 + (\delta_{12} - \Delta^{\text{AC}})^2} \quad (5.2)$$

an effective Rabi frequency that determines the period and the amplitude of the oscillation. In the resonant case, the Rabi frequency



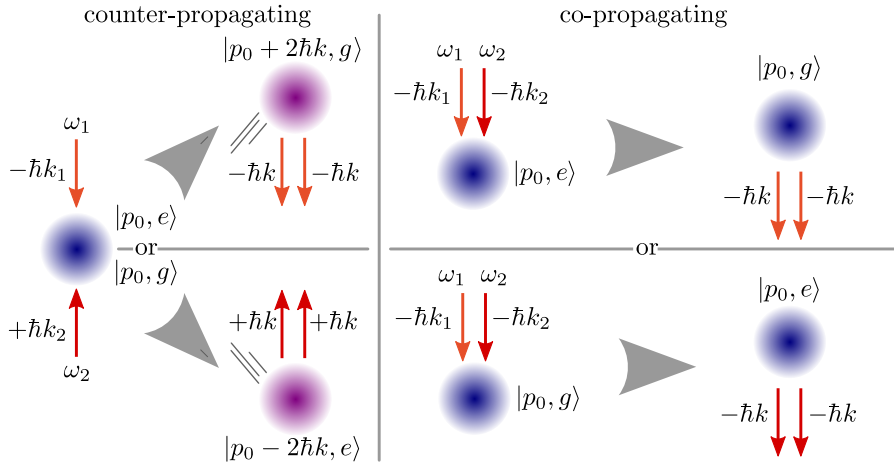


Figure 5.2: Counter- and co-propagating Raman transfers. The transferred momentum depends on the geometry of the Raman lasers beams. The typical momentum transfer of  $\pm 2\hbar k$  is only achieved for counter-propagating Raman lasers and the direction of the momentum is determined by the initial spin state. Here, accelerated clouds are depicted violet, whereas clouds at rest (in the free-falling frame) are blue. In the co-propagating case, the momentum-state of the atoms remain unchanged. In both cases, the combined momentum of the atom and the photons is conserved before and after the transfer.

reduces to a simple combination of the single Rabi frequencies  $\Omega_0 = (\Omega_1 \Omega_2^*) / (2\Delta)$  [115, 116], which are proportional to the respective laser intensities  $\Omega_{1/2} \propto \sqrt{I_{1/2}}$ .

In contrast to MW photons, the light coupling can also transfer substantial photon momenta to the atoms. The amount of momentum depends on the geometry of the laser beams and is largest for counter-propagating beams and vanishes for co-propagating beams. These two cases are visualised in Figure 5.2. As the process of absorption and emission is stimulated by the lasers, the momentum transferred as a result of absorption is parallel to the beam direction whereas the momentum kick due to emission is antiparallel to the respective beam. Also, the combined momentum of the atom and the photons has to be conserved. Therefore, the counter-propagating geometry transfers both photon momenta into the same direction. In our case of vertical alignment, this causes an upwards or downwards acceleration depending on the initial spin state of the atoms. The attained momentum is  $\pm \hbar(k_1 - k_2) \approx \pm 2\hbar k$  where the approximation  $k_1 \approx -k_2$  holds as the lasers' frequency difference is much smaller than their absolute frequency,  $\nu_{\text{hf}} = \omega_{\text{hf}} / (2\pi) \ll 384 \text{ THz}$ . In the co-propagating case, the two photon momenta are transferred with opposite direction and cancel each other, i. e. the co-propagating Raman transfer only changes the internal state.

If the atoms undergo a momentum kick, the attained movement causes an additional detuning due to the Doppler effect and the photon recoil. Both effects add to the detuning of the Raman transition such that in general

$$\delta_{12} = (\omega_1 - \omega_2) - \omega_{\text{hf}} - \frac{\vec{p}_0 \vec{k}_{\text{eff}}}{m} - \frac{\hbar |\vec{k}_{\text{eff}}|^2}{2m} \quad (5.3)$$

with  $\vec{k}_{\text{eff}}$  the transferred momentum ( $k_{\text{eff}} \approx 2k$  for counter-propagating geometry) and  $m$  the mass of the atom. As the Raman light interacts with free-falling and freely expanding ensembles, the momentum of an atom in the lab frame is

$$\vec{p}_0 = \frac{m}{2} \vec{g} t_{\text{tof}}^2 + m \vec{v}_{\text{exp}}, \quad (5.4)$$

i. e. a function of the time of flight  $t_{\text{tof}}$  and some velocity  $\vec{v}_{\text{exp}}$  due to the expansion of the ensemble. The acceleration by gravity  $g$  is global whereas the velocity  $\vec{v}_{\text{exp}}$  differs for each atom in the ensemble and points in all spatial directions. It is characterised by a velocity distribution that has to be narrow compared to the frequency width of the Raman light pulse to achieve a high overall transfer efficiency (details in [Section 5.2](#)). Similarly, also the spatial extent of the ensemble has to be much smaller than the waist of the beams to ensure equal light intensities for all atoms. This is on one hand achieved by proper adjustment of the laser path and the choice of the beam width, and on the other hand by reducing the spatial extent of the atomic clouds.

To approach a 100 % transfer, the overall detuning  $\delta_{12} - \Delta^{\text{AC}}$  must be sufficiently small (see [Equation 5.2](#)). The single AC-Stark shifts cannot be avoided, but the relative AC-Stark shift  $\Delta^{\text{AC}}$  can vanish, which reduces the influence of common intensity noise compared to simple counteracting with the detuning  $\delta_{12}$ . In general, technical noise in the laser intensities or geometry should be avoided as much as possible by the design of the optical system.

### 5.1.1 Optical setup

The optical setup consists of a Raman laser system that provides the two phase-locked frequencies, some optics and RF supplies that allow to shape light pulses and a small optical setup around the experiment chamber to illuminate the free-falling BEC. The overall setup is chosen to ensure high relative phase stability of both laser beams and to allow for future measurements of gravity by alignment with the gravitational acceleration  $g$ .

The Raman laser system including the phase-lock electronics was provided by the group of Ernst Rasel and jointly installed at our experiment. A detailed presentation of this system can be found in Ref. [\[117\]](#). The electronics of the phase lock including future modifications are also presented in Ref. [\[118\]](#). The Raman laser system consists

of two diode lasers which are each amplified by a tapered amplifier and then superposed on a fast photodiode. The beat signal, ideally at the frequency of the hyperfine splitting  $\nu_{\text{hf}} = 6.834$  GHz, is mixed with 7 GHz to obtain a difference frequency of 166 MHz. This signal is then compared to a source with variable frequency  $\sim 166$  MHz by an electronic phase detector. The output voltage of the phase detector is used to control the laser frequency via two paths. The voltage from the phase detector serves as error signal for a proportional-integral-differential (PID) controller that drives a piezo actuator to regulate the cavity length of laser 1. Additionally, the signal from the phase detector is filtered and amplitude matched and then used to directly modulate the laser diode current of laser 1, thereby realising the phase lock onto the laser 2. All frequency sources (including the MW and RF systems) are referenced to a common source of 100 MHz to ensure a stable phase relation between all pulses used in an experimental sequence. The frequency difference between both Raman lasers can be adjusted by changing the frequency the beat signal is compared to within the phase detector.

The superposed, orthogonally-polarised and phase-locked lasers then pass through a small setup to gain the ability of forming light pulses by using an AOM. This setup uses a minimum number of components to reduce the optical path for a relatively high stability of the final fibre coupling. The beam from the Raman laser system is mode cleaned by a short optical fibre and then passes the AOM which is fed by a RF that is sourced from a versatile frequency generator (*VFG-150*). This allows to temporally change the amplitude of the RF that drives the AOM and thereby enables us to shape the light pulses as shown in Section 5.1.3. The intensity of both lasers is monitored by detecting the small amount of transmitted light behind two mirrors. The transmission shows a slight dependence on the polarisation of the light. This allows to measure predominantly laser 1 behind the first mirror, and, by rotating the polarisation with a  $\lambda/2$  plate, predominantly laser 2 behind the second mirror. From both signals, the individual intensity drifts are recorded and also have been used to implement a slow intensity stabilisation via the current of the tapered amplifiers. However, drifts in intensity and polarisation due to the final fibre towards the experimental chamber cannot be stabilised in this way. To reduce these drifts, the final fibre coupling is frequently adjusted and carefully optimised to hit the polarisation-conserving axes of the optical fibre.

With this setup, the polarisation of the beams cannot be changed, such that the geometry (laser 1 and 2 from above, only laser 2 from below) is fixed. Therefore, the direction of the momentum kick can dynamically be reversed by changing the internal state before the Raman coupling. Besides the reduction of the optical setup, another reason to change the internal state rather the polarisation is the AC-

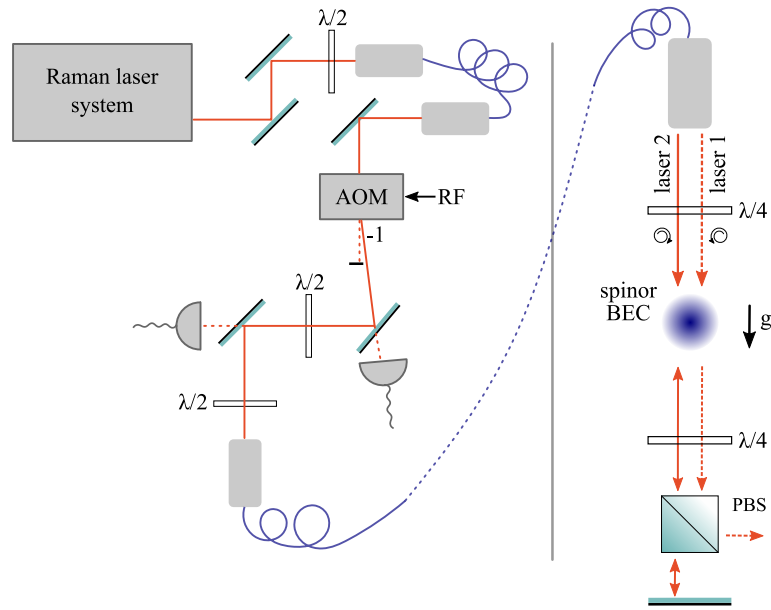


Figure 5.3: Optics and geometry of the Raman laser setup. The Raman laser system generates two phase-locked laser frequencies that are superposed in one beam with crossed linear polarisation, which passes an acousto-optic modulator (AOM) fed by a RF with variable amplitude to form light pulses. The Raman light is directed to the experiment by an optical fibre, the light is turned to oppositely circular-polarised components and then passes the free falling atomic ensemble from above. Due to selection by a polarizing beam splitter (PBS), only laser 2 is retro-reflected. Thereby processes other than the counter- and co-propagating light coupling as shown in Figure 5.2 are suppressed. The laser beams are aligned into the direction of earths gravitational acceleration  $g$  to allow to span an interferometer that is maximally sensitive. Figure has been partially published in Ref. [47].

Stark shift. As changing to opposite polarisations leads to swapped lasers in the asymmetric geometry, the AC-Stark shift compensation points would differ.

Finally, the Raman light is directed to the experiment by an optical fibre. The outcoupled, collimated laser beam has a  $1/e^2$  width of 1.5 mm and typically less than 1 mW power. The frequency components attain opposite circular polarisation by a  $\lambda/4$  plate and pass the free falling ensemble from above. After re-establishing the orthogonal linear polarisation below the ensemble, the component of laser 1 is selected by a PBS and leaves the system. The light of Raman laser 2 is retro-reflected and also illuminates the ensemble from below. Using this laser geometry suppresses unwanted light couplings and reduces the major processes to the counter- and co-propagating Raman transfers as depicted in Figure 5.2.

### 5.1.2 Differential AC-Stark shift

A one-photon coupling of two states generally causes an energetic shift of the states which depends on the detuning and the Rabi frequency, i. e. the intensity. The coupled energy levels approach each other when coupled by a blue-detuned frequency and separate for a red-detuned coupling. The latter is the case for the Raman light, thus the states  $|e\rangle$  and  $|g\rangle$  are lowered in energy. This so-called AC-Stark effect (also Autler-Townes effect) is exactly what causes the shift of the MW dressing employed to initiate spin dynamics. Only that in the case of the Raman light, the coupling to several states in  $5^2P_{3/2}$  has to be considered to properly predict the shift.

The single AC-stark shifts  $\delta_g^{\text{AC}}$  and  $\delta_e^{\text{AC}}$  cannot be avoided. But, as can be seen from Equation 5.2, only the differential shift  $\Delta^{\text{AC}}$  has a direct influence on the transition probability. To simply compensate  $\Delta^{\text{AC}}$  by the detuning  $\delta_{12}$  is not optimal in the presence of noise in the intensities of the Raman lasers. To achieve optimal robustness, a working point where the differential AC-Stark shift vanishes is chosen by adjusting the intensity ratio  $I_2/I_1$  of both Raman lasers.

In the lab, this working point is determined by observing the relative shift of the clock states with a MW coupling. To this end, the resonance frequency and  $\pi$ -pulse time of the clock transition is measured as it is. The ensemble then undergoes the same MW transition while being illuminated by the Raman light. If the intensity ratio is not at the value of a vanishing differential shift, the MW transfer will be reduced. Now, the intensity ratio of the Raman lasers is changed such that the MW transfer is at its maximum, i. e. resonant again. For this calibration, the Raman light is reduced in intensity to decrease the absolute shift to several kHz and also slightly detuned to avoid actual Raman transfer during this measurement. By this method, the intensity ratio that leads to a vanishing differential shift was measured to be  $I_2/I_1 = 0.93$ .

The calibration agrees with the theoretical prediction as shown in Figure 5.4. Often the beam geometry is chosen to be symmetric, that is either both Raman light fields illuminate the ensemble from the top and from below or only laser 1 comes from above and only laser 2 from below. This scenario is shown by the dashed lines. For this work, the light of frequency  $\omega_1$  leaves via the PBS as depicted in Figure 5.3, such that the ensemble is only illuminated by laser 2 from below. Thereby, the effective intensity of laser 1 is halved, which in turn also halves the intensity ratio needed to compensate the differential light shift (because of the Clebsch-Gordan coefficients being symmetric for opposite circular polarisation of the light). The calculation shown by the solid lines in Figure 5.4 predicts the desired intensity ratio to be  $I_2/I_1 = 0.86$  at a detuning of  $\Delta = -1.1 \text{ GHz} + \Delta_{F'=3} + \nu_{\text{AOM}} = -0.756 \text{ GHz}$  with respect to the transition  $|5^2S_{1/2}; F=2, m_F=2\rangle \leftrightarrow |5^2P_{3/2}; F'=1\rangle$ . This corresponds to a detuning of  $\Delta = -1.1 \text{ GHz}$

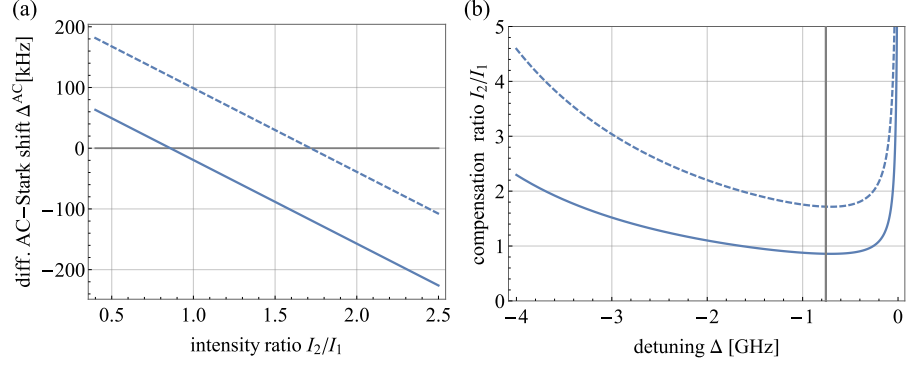


Figure 5.4: The differential AC-Stark shift for the symmetric configuration (dashed line), i. e. both lasers illuminate the ensemble from top and below, and the asymmetric configuration (solid line), as shown in Figure 5.3 and used for the experiments in this work. At a detuning of  $\Delta = -0.756$  GHz the differential shift  $\Delta^{\text{AC}}$  vanishes at  $I_2/I_1 = 0.86$  in the asymmetric and at  $I_2/I_1 = 1.72$  in the symmetric case. The intensity ratio that compensates  $\Delta^{\text{AC}}$  grows for a larger or smaller detuning  $\Delta$ . The grey line in (b) marks the working point  $\Delta = -0.756$  GHz for the experiments in this work, which is chosen to be in the range where the ideal intensity ratio is the least affected by the detuning.

with respect to the transition  $|5^2S_{1/2}; F = 2\rangle \leftrightarrow |5^2P_{3/2}; F' = 3\rangle$ , i. e. the frequency of the MOT cooling laser that serves as absolute reference for the Raman laser system. Also the common frequency shift of the Raman light by the switching AOM of  $\nu_{\text{AOM}} = -80$  MHz has to be taken into account here. Details on the calculation of the light shift are shown in Section A.3.3.

It is reasonable that the measured value is slightly higher than the prediction, as the computation does not account for reflections on the surfaces of the glass chamber. The intensity of laser 2 was measured below the glass chamber to be reduced to 84 % of the intensity above the chamber, which could be explained by a loss of 4 % at each air-to-glass or glass-to-air transition. From this assumption, the actual intensities that illuminate the atoms originate from the beam intensities  $I_2 = I_0(0.93 \cdot 0.96^2 + 0.93 \cdot 0.96^6)/2$  and  $I_1 = I_0 \cdot 0.96^2$ , which leads exactly to the predicted ratio of  $I_2/I_1 = 0.86$ .

As the optimal intensity ratio to minimise the differential AC-Stark shift is achieved, the next step is to implement temporal control of the common intensity of the Raman light.

### 5.1.3 Shaped pulses

The intensity of the Raman light pulses is temporally shaped to decrease frequency components with large offset from the carrier frequency. The ideal frequency distribution of a pulse is generally given by the Fourier transform from the time to the frequency domain.

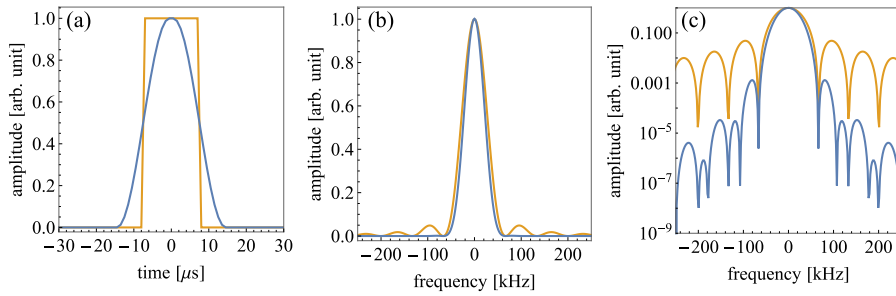


Figure 5.5: Comparison of a box pulse (orange) and a  $\sin^2$  pulse (blue) of equal area. Here the total pulse durations are  $15\ \mu\text{s}$  and  $30\ \mu\text{s}$  respectively. The temporal shape (a) of the coupling pulses determines their distribution in frequency space. In the predicted signal of a pulse spectroscopy measurement (b-c), the side peaks at larger offset from the carrier frequency are strongly suppressed for the  $\sin^2$  pulse.

Therefore, the longer a pulse is in the time domain, the narrower it becomes in the frequency domain.

For a box pulse, i. e. simply switching the Raman light on and off instantaneously, the frequency distribution is a  $\text{sinc}^2$  function, which shows characteristic side peaks at larger frequency offsets from the carrier. In the experiment, pulses with  $\sin^2$  slopes are employed as these feature a suppression of the side peaks. Figure 5.5 compares a box pulse and a  $\sin^2$  pulse of equal area, i. e. equal ability to drive a transfer. The box pulse shows frequency components with about 1% relative amplitude at more than 200 kHz distance from the carrier, even though the width of the carrier is only about 100 kHz. In the case of the  $\sin^2$  pulse, the relevant frequency components are within the centre peak around the carrier frequency, which allows for a better separation of the desired counter-propagating Raman transfer to other possible couplings, e. g. to the co-propagating transfer as depicted in Figure 5.6.

A typical spectroscopy of the Raman transfer after 8 ms free fall time is depicted in Figure 5.6. The major peak shows the transferred fraction of atoms that gained  $2\hbar k$  momentum and changed the internal spin state, i. e. the result of the desired counter-propagating transfer. The resonance frequency of this transfer is shifted from the actual hyperfine splitting  $\nu_{\text{hf}} = 6834.682\ \text{MHz}$  by the Doppler shift, as described in Equation 5.3. To be precise, the shift is two times the Doppler shift with respect to each involved Raman laser. The atoms fall towards laser 1 and move away from laser 2, that is the overall detuning becomes  $\delta_{12} \propto (\omega_1 - \omega_D) - (\omega_2 - \omega_D) = (\omega_1 - \omega_2) - 2\omega_D$ . In the case of the transfer driven by co-propagating light fields, no relative shift is caused, and the resonance frequency is independent of the ensembles centre-of-mass velocity, i. e. the free-fall time, in this case. However, here the detuning  $\Delta$  to the intermediate level is shifted by the Doppler



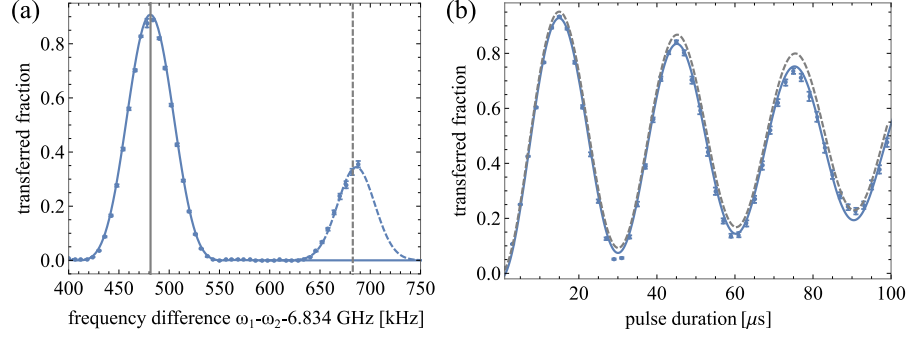


Figure 5.6: Determining the resonance frequency and the Rabi frequency of the Raman pulse. (a) Spectroscopy of the counter-propagating transfer subsequent to 8 ms free-fall. The peak transfer is shifted by  $\nu_{Doppler} = -201$  kHz from co-propagating resonance, which is close to the frequency of the hyperfine splitting (grey dashed line). (b) Rabi oscillation of the counter-propagating Raman transfer. The oscillation is fitted with a damped sin function (grey dashed line) and a damped oscillation modified by the velocity selectivity (blue line), which becomes relevant for the larger pulse durations.

effect which according to Equation 5.2 alters the Rabi frequency and thereby causes a reduced transferred fraction.

A Rabi oscillation for the counter-propagating transfer shows a damping that follows the fit function

$$P(\tau) \approx \frac{1}{2} (P_{\max}(\tau, \sigma_v) + \cos(\tau\Omega_{\text{eff}})e^{-\gamma\tau}) \quad (5.5)$$

where the ideal result of Equation 5.1 is extended by a general damping term  $e^{-\gamma\tau}$  and the maximum transfer probability  $P_{\max}(\tau, \sigma_v)$  for a pulse of time  $\tau$  and a given velocity width  $\sigma_v$  of the ensemble. The additional term  $P_{\max}(\tau, \sigma_v)$  is motivated by a formula stated in Ref. [119], and here represents the slightly decreasing fraction of atoms participating in the Raman processes due to the increasing velocity selectivity of the pulse. Details on the computation of  $P_{\max}$  are shown in Section A.3.4. This extra term is needed to describe the slight asymmetric damping observed in the data, which is not captured by a fit with only a general damping as depicted in Figure 5.6. Here, the damping is only phenomenologically described by the factor  $\gamma$ , but is likely to be caused by a combination of spontaneous decay and Doppler shift. Both effects increase with the pulse duration and could be mitigated by implementing a larger detuning  $\Delta$  and a frequency chirp. However, the first maximum of the transfer, i. e. the  $\pi$ -pulse, is only slightly affected by the damping, especially if pulse durations are further decreased. Also the velocity selectivity should not affect the transfer efficiency at this point as it is shown below in Figure 5.10.

Generally, the optimisation of the Raman transfer involves a trade-off between several effects. The effect of the mentioned damping and the velocity selectivity can be reduced by increasing the laser power



and thereby decreasing the required pulse time. As a side effect, the short pulses become broad in frequency, which could cause near-resonance to undesired transfers as the co-propagating transfer. Also it becomes more likely to drive transitions that are suppressed by the geometry or polarisation, or by light from unwanted reflections on the glass cell. At least the co-propagating transfer can be avoided by extending the free-fall time before the Raman coupling. For shaped pulses of about  $15\ \mu\text{s}$ , the resonances are sufficiently separated after about 5 ms. The necessary free-fall time could be reduced by the use of shorter pulses. For  $\pi$ -pulse times less than  $10\ \mu\text{s}$ , however, slight transfer to momentum modes without a change in spin state have been observed in our system, which we assign to Bragg transfers on standing light waves as these were driven by only a single Raman frequency from one direction. For Bragg transfers on standing waves, the atoms have to move with a non-vanishing angle towards the light-wave, which is the reason we assign unwanted reflections to be involved here. A concise overview of the different types of momentum transfers available by atom-light interaction can be found in Ref. [120]. On the other hand, working with much less power where  $\pi$ -pulse times become long, the pulses are narrow in frequency and become velocity selective regarding the residual expansion of the ensemble. Here we observed that spatial patterns occur, such that for example only the centre part of the cloud is effectively transferred by the velocity-selective Raman pulse. Therefore, finding an optimal working point for the Raman transfer also involves to modify the expansion of the ensemble.

## 5.2 COLLIMATION OF ATOMIC CLOUDS, TRANSFER EFFICIENCY AND DETECTION NOISE

After releasing the BEC from the dipole trap, the mean field energy drives an accelerated expansion that turns into a constant expansion within  $\sim 1\ \text{ms}$ , which is characterised by the growing width of the atomic cloud. One way to reduce the expansion is to slowly ramp down the dipole trap, such that the trap is less confining when being switched off. A disadvantage of this procedure is an extended holding time, which can harm the previously entangled states by decoherence, losses and heating or by uncontrolled spin dynamics, as the ramp also causes a variation of the spin dynamic resonance condition. Therefore, in this work, a pulsed potential is applied after 1 ms free fall to reduce the momentum distribution of the cloud [121], a technique also called delta-kick collimation.

The collimation pulse is implemented using the optical dipole trap. During the initial free fall of 1 ms the atomic cloud moves by less than  $5\ \mu\text{m}$  and therefore is still sufficiently well within the focus of the original dipole trap. The collimation procedure affects the centre-of-

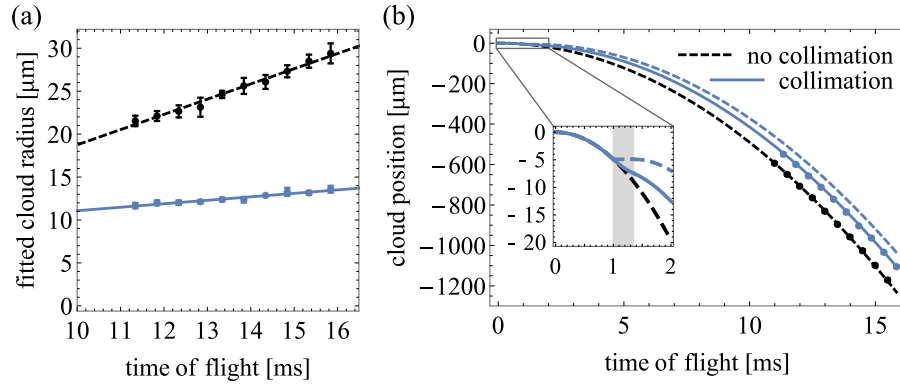


Figure 5.7: Expansion rates and trajectories of free-falling ensembles. The un-collimated case (black data points, dashed lines) is compared to the collimated ensemble (blue data points, solid lines) which experienced a collimation pulse of  $350 \mu\text{s}$  length. The expansion of the atomic cloud in (a) is measured by fitting a Gaussian to the density distribution of the atomic cloud after various free-fall times and calculating the rate of change of the standard deviation. Here, the expansion is reduced by 78 % from  $1.86(8) \mu\text{m}/\text{ms}$  to  $0.41(3) \mu\text{m}/\text{ms}$ . The trajectories in (b) show that the clouds clearly follow the respective free-fall trajectory with  $g = 9.81 \text{ m/s}^2$ . To fit the collimated data well, the effect of the collimation pulse on the centre-of-mass movement is modelled by an upwards acceleration of  $2.5g$  during the time of the collimation pulse. For comparison, the case of a resting cloud during the collimation is also shown (blue dashed line).

mass trajectory of the atomic ensemble (small upwards acceleration) and reduces the radial expansion. The cloud remains in a round shape after extended time of flight, from which we conclude a sufficiently homogeneous collimation. The size of the clouds at the point of the detection affects the precision in counting the atom numbers, as a larger area on the absorption images has to be evaluated for larger clouds. As the characterisation and application of highly entangled states is usually limited by detection noise [63, 64], the effect of a reduced final extent of the atomic clouds is the major benefit from the collimation.

The reduction of the constant expansion is shown in Figure 5.7, where the width of a Gaussian fit to the density profile of the freely falling and expanding clouds is recorded. The slope of this signal gives the constant expansion rate. Here, the initial expansion of  $\sigma_v = 1.86(8) \mu\text{m}/\text{ms}$  is reduced to  $0.41(3) \mu\text{m}/\text{ms}$  by flashing the optical dipole trap with its original laser powers for  $350 \mu\text{s}$ . The residual expansion corresponds to an effective temperature of  $1.7(3) \text{ nK}$ .

The position of the centre of mass of the clouds is also extracted from the absorption images and clearly follows the free-fall trajectory  $s(t) = -gt^2/2$  if no collimation is applied. With collimation, the clouds are still in free fall when being detected, but are slightly retarded. The

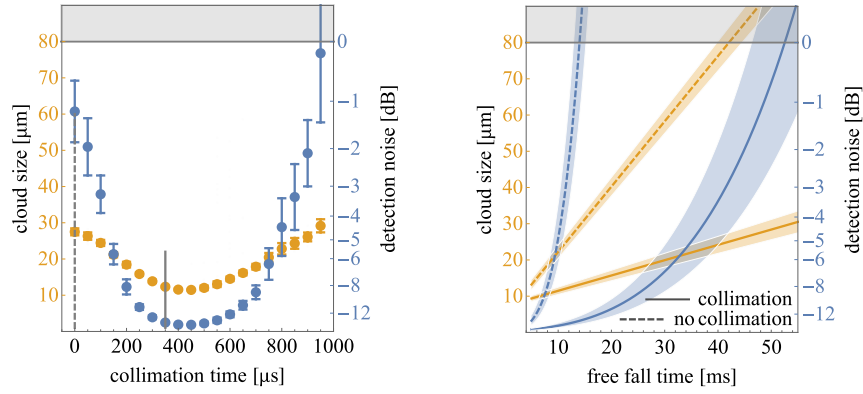
trajectory of the collimated ensemble is well described by modelling the effect of the collimation pulse on the centre of mass motion by an upwards acceleration of  $2.5g$  during the time of the pulse.

The residual expansion rate depends on the length of the collimation pulse. To determine a good working point, the size of the atomic cloud is measured at a fixed free-fall time for a varying collimation-pulse length. [Figure 5.8](#) shows that the cloud size is reduced up to about  $400 \mu\text{s}$  collimation time and then increases again to even larger extent as without collimation. At this point, the atoms are actually accelerated such that the clouds inflect, similar to a focussed laser beam that diverges behind its focus. Each measured mean cloud size corresponds to a minimal number of relevant pixels on the absorption images. As each additional pixel adds noise to the detected number of atoms in the cloud, a minimal cloud size here also corresponds to a minimal final detection noise<sup>2</sup>. For details on the mapping from the measured cloud size to the inferred detection noise see [Section A.2.2](#).

Based on the expansion rates shown in [Figure 5.7](#), the size of the clouds and the respective minimal detection noise is extrapolated to longer free-fall times. For the working point chosen in the following, i. e. ensembles of  $N \approx 10^4$  atoms and a free-fall time of  $15 \text{ ms}$ , the collimation reduces the detection noise from  $1 \text{ dB}$  to  $-13.4 \text{ dB}$  with respect to the ensemble's shot noise. As the verification of entanglement usually demands a detection of atom numbers below shot noise, the collimation here actually enables the detection of entangled ensembles after extended free fall. The residual expansion limits the ability of sub-shot-noise detection of our ensembles to  $50 \text{ ms}$ . The practical limit for now, however, is at  $\sim 20 \text{ ms}$  as in our apparatus the atoms then leave the range of the detection optics. Prior to this work, the detection of entanglement after substantial free fall has been reported once for squeezed thermal ensembles after a maximal free-fall time of  $8 \text{ ms}$  [79].

In [Figure 5.9](#) the frequency width of the counter-propagating Raman transfer is compared to the spread of Doppler shifts caused by the velocity width of the ensemble. The Doppler spread of the collimated cloud has a width of only  $\sigma_D = k\sigma_v / (2\pi) = 0.52(5) \text{ kHz}$  which is less than  $1\%$  of the Fourier width of the Raman pulse. Within this setting, highly efficient counter-propagating Raman transfers are achieved, as shown by the transferred fraction for two consecutive Raman  $\pi$ -pulses. The first Raman pulse transfers  $97.2(6)\%$  of the atoms in the ensemble from  $|0\hbar k; 2, 0\rangle$  to  $|2\hbar k; 1, 0\rangle$ . The attained momentum points upwards. After a minimal waiting time of  $40 \mu\text{s}$  to remove the remaining atoms in  $|2, 0\rangle$ , a second Raman pulse with equal frequency and time decelerates the atoms back to  $|0\hbar k; 2, 0\rangle$ . The second transfer yields an even higher efficiency of  $98.5(6)\%$ . Calculations based on

<sup>2</sup> Minimal clouds sizes are optimal as long as the cloud is relatively dilute. If the ensemble is larger or the extent of the cloud even smaller, e. g. when detecting directly after releasing from the dipole trap, the detection becomes less accurate.



- (a) Effect of the collimation pulse length on cloud size and detection noise. The size of the atomic cloud is measured at a fixed free-fall time of 13 ms after the collimation for a varying collimation-pulse duration. The cloud size determines the minimal number of relevant pixels on the CCD camera which in turn corresponds to a minimal detection noise. The resulting detection noise is compared to the shot-noise (grey area) of an ensemble of  $N = 9300$  atoms (which corresponds to the ensemble size prepared for the main measurement in Figure 5.14).
- (b) Extrapolation to longer free-fall times based on expansion rates measured for the collimated (solid lines) and the un-collimated (dashed lines) case. The corresponding collimation-pulse durations are marked by vertical lines in (a). The shaded areas represent the uncertainty of the extrapolation. The maximal free-fall time that technically allows for sub-shot-noise detection of the entangled ensemble presented in this section is increased by a factor of 3.7 to about 50 ms.

Figure 5.8: The cloud size (orange data, left scales) and the resulting detection noise (blue data, right scales) for free-falling ensembles. The detection noise shown here refers to the detection of two atomic clouds with the respective size each, as usually the atom numbers of two modes have to be measured.

the measured residual expansion rate suggest, that this discrepancy cannot be explained by the velocity selection (see Figure 5.10). Also the Doppler shift due to the small extra free-fall time is too small to explain the difference. Therefore, we attribute the reduced efficiency of the first transfer to a small fraction of atoms with larger velocities, which are not captured by the analysis of the mere expansion rate. These atoms could stem from a small thermal fraction within the initial BEC or from the collimation procedure. In this sense, the first Raman pulse would indeed be velocity selective, and leave a cleaner ensemble for the successive transfer. Therefore, all successive Raman couplings are assumed to show equal transfer efficiency to the second  $\pi$ -pulse. The fluctuations are equal for both transfer pulses, which supports the assumption, that there is a small fraction of atoms in the initial ensemble that simply does not interact with the Raman light.

The expected velocity selectivity can be calculated from the Raman spectroscopy signal and the residual Doppler spread of the ensemble as depicted in Figure 5.9. The predicted decrease of the Doppler

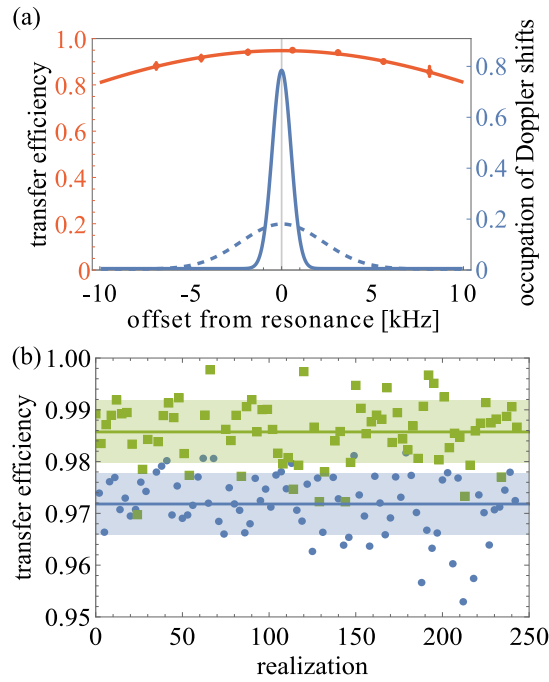


Figure 5.9: Setting and results of the implemented counter-propagating Raman transfer. (a) The Raman spectroscopy for the implemented pulse time of  $\sim 15 \mu\text{s}$  (orange data points and fit) is compared to the distributions of Doppler shifts due to the velocity spread without collimation (dashed blue line) and with a collimation pulse of  $350 \mu\text{s}$  (solid blue line). The collimation reduces the Doppler spread by 77 % to  $0.52(5) \text{ kHz}$ . This is less than 1 % of the bandwidth of the Raman pulse. In (b), the transfer efficiencies for two consecutive Raman pulses are shown. The second Raman transfer yields a mean efficiency of  $98.5(6) \%$ , slightly higher than the first transfer with  $97.2(6) \%$ . The fluctuations remain similar.

spread and the potentially increased efficiency of the second transfer are shown in [Figure 5.10](#). The improved transfer efficiency of the second Raman pulse cannot be explained by the residual Doppler spread as for the collimated ensemble no reduction of the spread is predicted. Even for the uncollimated ensemble, the reduction of the initial Doppler spread is small and could not explain the observed difference of 1.3 % in the transfer efficiency.

The nevertheless observed selection by the first Raman pulse can always be regarded as a mere reduction of the ensemble size if an ensemble of uncorrelated atoms is transferred. In the case of entangled states, however, a loss of a small fraction of atoms can partially destroy the entanglement. The actual contribution of the non-selected fraction of atoms to an entangled state remains unclear. If these atoms stem from a thermal background they do not participate in the entangled state from the beginning, and the selection by the first Raman transfer does not harm the entanglement. However, the remaining imperfections as inherent to the second Raman transfer, do have a

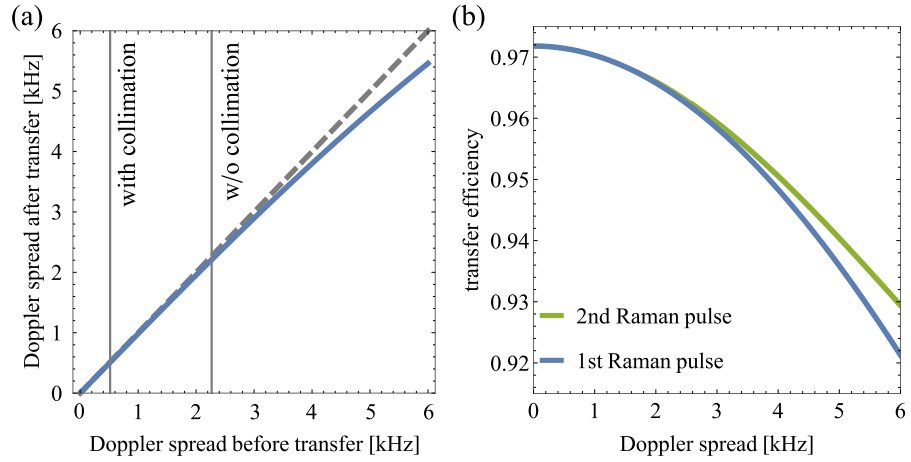


Figure 5.10: Predicted selectivity of the Raman transfer based on the measured expansion rate. In (a) the Doppler spread before and after the Raman transfer are compared. A large initial Doppler spread is reduced by the selectivity of the Raman transfer. The grey dashed line corresponds to a unchanged spread. In (b) the effect of the selectivity on the expected Raman transfer efficiency is shown. For the collimated ensemble, neither the Doppler spread nor the transfer efficiency change for successive application of Raman pulses. Even without collimation, the velocity-selection by the Raman pulse is predicted to be small.

strong influence on the entangled state, as here entangled atoms are definitely lost and the fluctuations of the transfer deteriorates a potential sub-shot-noise signal. Anyhow, the realised momentum transfer belongs to the best reported Raman transfers regarding efficiency and fluctuations [122–124]. The numbers have to be compared to the second Raman transfer, as usually the ensembles are velocity-selected before evaluating the transfer efficiency and are usually given in terms of efficiency per  $\hbar k$ , which in our case is 99.3(3) %.

### 5.3 PREPARING ENTANGLED MOMENTUM MODES

The techniques to prepare a large fraction of the ensemble in a twin-Fock state and the realised highly efficient Raman transfer are combined to prepare entangled momentum modes. The main idea of the protocol is visualised in Figure 5.11. The BEC is held in the dipole trap and undergoes a quasi-adiabatic passage through a quantum-phase transition as discussed in Section 4.3 to prepare a twin-Fock state in spin space. The ensemble is then released to free fall and a spin-dependent momentum transfer prepares one of the twin modes in a distinct momentum mode. To this end, the ensemble’s free expansion is reduced and the relatively small fraction of atoms that do not populate the twin-Fock state are removed prior to the transfer. The final detection of the clouds by absorption imaging allows to count

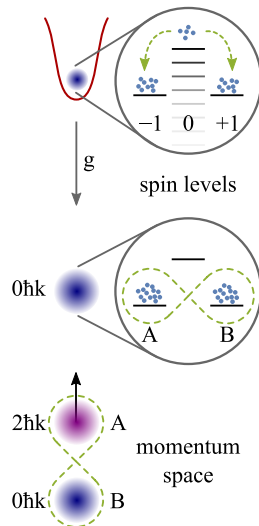


Figure 5.11: Summarising sketch of the main idea. Entanglement is created between spin states of a BEC by spin-changing collisions in an optical dipole trap. Subsequently, the trap is switched off and the entangled ensemble undergoes a spin-dependent, coherent momentum transfer during free fall. Spin- and momentum-state-selective detection allows to verify particle entanglement between the distinct momentum modes.

the population of the different spin and momentum states and the characterisation of the remaining particle entanglement between the prepared momentum modes.

The detailed experimental protocol is depicted in Figure 5.12. During about 1 s holding time in the optical dipole trap, the twin-Fock state is prepared in the spin modes  $|1, \pm 1\rangle$ . The trap is switched off instantaneously to release the ensemble to free space where mean field energy is converted into a constant width in momentum space. After 1 ms of free fall, the trap is flashed on again for 350  $\mu\text{s}$  to realise a reduction of the width in momentum space as explained above. The remaining atoms in  $|1, 0\rangle$  can be expelled from the relatively dilute ensemble by a MW transfer to  $|2, 0\rangle$  and a subsequent illumination with light resonant only to the  $F = 2$  manifold. This cleaning process is actually enabled by the initial quasi-adiabatic preparation of the twin-Fock state, since removing more than  $\sim 30\%$  of the ensemble by this technique has been shown to reduce the number squeezing. For the usual preparation by a rapid quench, a strong post selection would be required, as here rarely more than 70% of the atoms populate the twin-Fock state.

Another resonant MW pulse transfers one of the twin modes from  $|1, -1\rangle$  to  $|2, 0\rangle$ , where, after a total free-fall time of 7.7 ms, the atoms finally undergo a counter-propagating Raman transfer to  $|1, 0; 2\hbar k\rangle$ . The amount of transferred momentum is a factor of 29(3) larger than the residual width in momentum space and therefore constitutes a



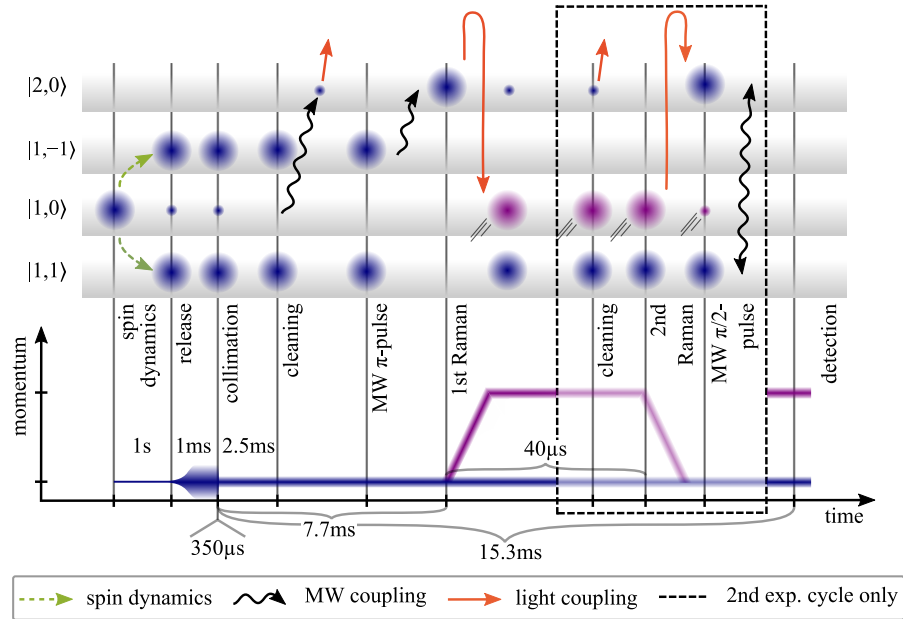


Figure 5.12: Visualisation of the experimental sequence implemented to transfer twin-Fock states from the spin degree of freedom to momentum space. The transfers and couplings between the various involved spin states are depicted on the top. The type of coupling is indicated by different arrows (see legend) and involves resonant MW pulses, cleaning light pulses and two-photon stimulated Raman transitions. To characterise the entanglement of the two momentum modes, two conjugate observables  $J_z$  and  $J_\perp$  are measured in two alternating experimental cycles. Operations enclosed by the dashed rectangle only take place in the second cycle to measure  $J_\perp$ . The time-momentum diagram at the bottom depicts the effect on the momentum mode of the atomic cloud in the free-falling reference frame (axes not to scale).

clear separation into distinct momentum modes. In the first experimental cycle, the atoms then fall freely for another 7.76 ms such that the separation in momentum space also manifests in a spatial separation of the two twin-Fock modes. The trajectories and the spatial separation of the two clouds are depicted in Figure 5.13. Within the first experimental cycle, the centre of mass of both atomic clouds separate by  $80(1) \mu\text{m}$  which constitutes a full spatial separation of the modes. A magnetic field gradient prior to the final detection also separates the different spin states spatially on the final absorption images. In this way, the small fraction of atoms that remains in  $|2,0\rangle$  after the first Raman transfer can also be detected and used for the analysis of the entangled state.

From the resulting mode population after this first experimental cycle, the number squeezing given by the reduced fluctuations of  $\langle J_z \rangle$  can be extracted. As a reference, a similar protocol without any Raman transfer has been conducted, which yields the result of an equally prepared twin-Fock state in free fall. Thereby, three scenarios



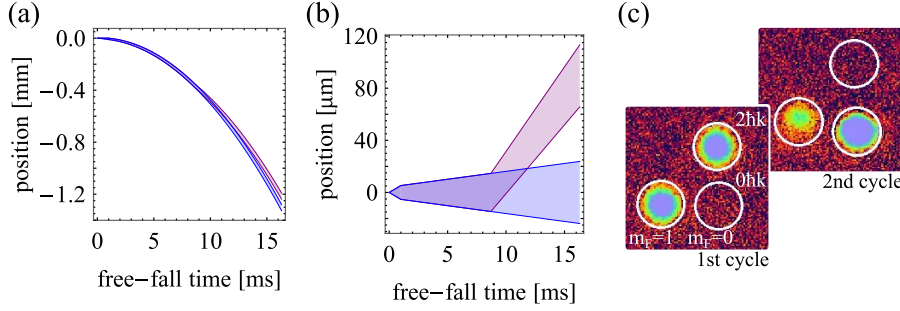


Figure 5.13: The two twin-Fock modes freely fall for about 1.2 mm as depicted by the trajectories in (a). At the end of the 1st experimental cycle, the two twin modes are completely separated by  $80(1) \mu\text{m}$  (center of mass) as visualised by the same trajectories in the free free-falling frame (b) and on the final absorption images (c). On the absorption images, different momentum modes separate vertically and different spin components horizontally. The white circles around the atomic clouds depict the detection masks, within which the images are evaluated. The density distribution in (a) and (b) is modelled as an expanding Gaussian and the shaded areas correspond to a  $3\sigma$  width. Note that the clouds on the absorption images seem to be less separated (vertical direction) due to the logarithmic depiction of the density.

can be directly compared: (i) The twin-Fock state in spin space after free-fall only, (ii) the twin-Fock state in momentum space directly measured and (iii) the conditional result in momentum space by using the additional information of the atoms not transferred by the first Raman pulse. The measured number squeezing for each scenario is shown with respect to shot noise of the ensemble's mean total atom number  $\langle N \rangle = 9300$  in Figure 5.14 and amounts to (i)  $-5.4(6)$  dB, (ii)  $-3.9(6)$  dB and (iii)  $-5.2(7)$  dB. The number squeezing after free fall (i) differs only by  $\sim 0.5$  dB compared to similarly produced twin-Fock states measured directly after release from the dipole trap, which can be explain by the small change in the detection noise. The classical bound at 0 dB was verified by measuring the shot-noise fluctuations of a coherent spin state prepared by a RF pulse (instead of using spin dynamics) and otherwise undergoing the same sequence as the twin-Fock state.

As discussed in Section 2.1.3, the detection of number squeezing is not sufficient to verify entanglement. To actually prove that the two momentum modes are entangled, an orthogonal pseudo-spin direction has to be measured. Therefore, in the second experimental cycle, an additional  $\pi/2$ -coupling between the modes is realised. This coupling rotates the twin-Fock state on the Bloch sphere such that the ring stands upright and goes through the poles instead of being situated on the equator. After the coupling, the measured fluctuations are large and the outcome distribution shows the characteristic cumulation at extreme values. The evaluation of the variance of this

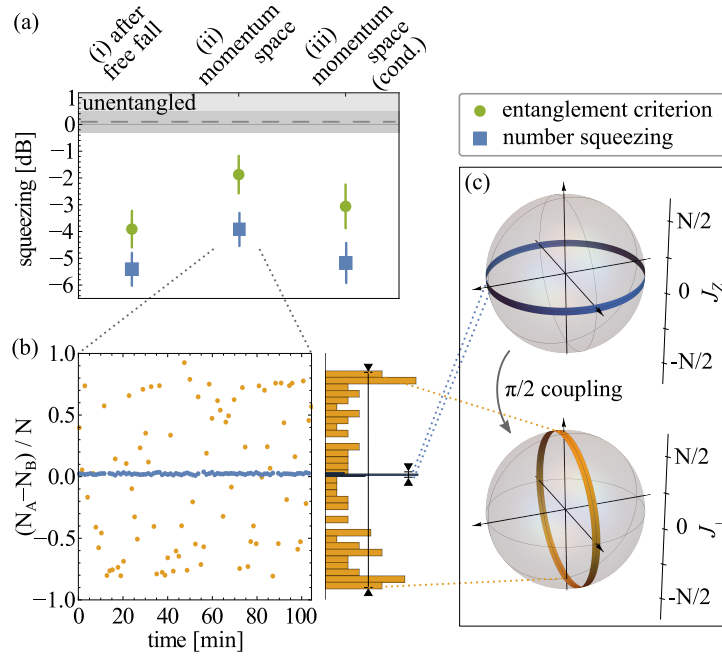


Figure 5.14: Realisation of entangled momentum modes suitable for light-pulse atom interferometry. (a) The measured number squeezing  $4(\Delta J_z)^2/N$  (blue squares) and squeezing parameter  $\zeta^2$  (green dots) measured after free fall and in momentum space with and without taking into account the small fraction of non-accelerated atoms. All values are well below the classical limit of 0 dB (light grey area). This bound is experimentally verified by the measurement of a coherent spin state (grey dashed line, uncertainty as dark grey area) after equal free-fall time. (b) The measured atom number difference after the 1st experimental cycle represents the number squeezing (blue data points and histogram). At the end of the 2nd experimental cycle, the orthogonal spin projection is measured (orange data points and histogram). Each set of data points in (a) is derived from such a series of measurements. (c) The two measured observables are the width and the diameter of the ring representing the twin-Fock state on the Bloch-sphere.

distribution leads to a spin length of  $\langle J_{\perp}^2 \rangle = 0.63(5) \times N/2(N/2 - 1)$  and combines with the number squeezing to a generalised squeezing parameter (Equation 2.22) of (ii)  $-1.9(7)$  dB directly measured and (iii)  $-3.1(8)$  dB conditional on the left-over atoms. After free fall only (i), the measured spin length is slightly larger (69% of the ideal value) which causes a better squeezing value of  $-3.9(7)$  dB. Thus, the reduction of the spin length cannot be explained by the additional noise of the Raman transfer. A plausible explanation, however, is the small displacement of the two atomic clouds upon the minimal waiting time of  $40 \mu\text{s}$  in between the two Raman pulses. During this time, the accelerated cloud moves by  $0.5 \mu\text{m}$ , which can explain the observed reduction in spin length by about 9% (for details see Figure 6.1).

If the independently characterised detection noise is subtracted from the respective results, we achieve (ii)  $-4.4(7)$  dB number squeezing and a generalised squeezing parameter of  $-2.4(8)$  dB. In the conditional case (iii), where the non-transferred atoms are taken into account, the measurement yields  $-5.9(9)$  dB and  $-3.8(9)$  dB respectively.



## DISCUSSION AND OUTLOOK

Entangled atomic ensembles in the spin degree of freedom are currently prepared in many experiments and proved to be useful in a variety of interferometric measurements [25]. However, momentum-entangled ensembles, as required for inertially sensitive atom interferometers beyond the SQL, present a long-standing challenge [40]. In this work, entanglement was generated in the spin degree of freedom of a BEC and successfully transferred to distinct momentum modes by a stimulated Raman transition. The expansion rate of the free-falling ensemble was reduced, enabling a detection noise below the atomic shot noise even after substantial free-fall times. The entangled momentum modes presented in this work constitute a successful proof of principle of transferring entanglement from spin space, where its generation is well-established, to momentum space. As the main technological ingredients of the realised protocol are established tools in the field of atom interferometry, the prepared momentum modes present a viable entangled source to be integrated in existing light-pulse atom interferometers. Upon a few technical improvements and a refining of the source, a full atom interferometer to measure Earth's acceleration  $g$  with sub-SQL sensitivity can be implemented in our apparatus. Furthermore, the presented entangled momentum modes can serve as the basis of other interferometric measurements as for example a Bell test.

In the following, limiting noise sources and possible improvements of the presented entangled source are discussed. Thereon an extension of the realised protocol to an entanglement-enhanced gravimeter is presented. Finally, based on the techniques utilised in this work, a scalable atomic Bell test is sketched.

## 6.1 REFINING THE ENTANGLED SOURCE

There is much potential to realise more squeezing in the momentum modes. Compared to previous results achieved in our group [53], the detected number squeezing of the twin-Fock states in this work is reduced. Reaching a comparably low detection noise after extended free-fall with respect to the earlier experiments, which detected the ensembles directly after the release from the dipole trap, is one of the main achievements of this work. The minimal detection noise was reduced from  $\sigma_{N_{\perp}} \sim 108$  atoms to  $\sigma_{N_{\perp}} \sim 22$  atoms by collimating the ensemble and should in principle allow to detect number squeezing of up to  $-13$  dB with respect to an ensemble size of  $N = 10^4$  after a free fall of 15 ms. Similarly prepared twin-Fock states directly

measured after the release from the dipole trap, as well as twin-Fock states prepared by the usual rapid quench, showed equally reduced number squeezing during the time the experiments in momentum space were conducted. We attribute the reduction in number squeezing to a technical issue before the detection. Probably, the ensemble has not been properly illuminated with light that optically pumps all spin states to  $F = 2$  before the detection. If the ensemble is not completely pumped, atoms would more likely stay in  $|F = 1, m_F = 1\rangle$  than  $|F = 1, m_F = -1\rangle$ , causing more fluctuations in the number difference. In principle, the number squeezing is not expected to deteriorate much during the free fall, and typically observed reductions of about  $\sim 0.5$  dB are well explained by a small change of the detection noise.

The presented quasi-adiabatically prepared twin-Fock states exhibit a reduced spin length of  $\langle J_{\perp}^2 \rangle = 0.69(5) \times N/2(N/2 - 1)$ , which is attributed to the extended holding times in the optical dipole trap, required to realise the state preparation. This effect was observed previously in our experiment [53] and has actually been reduced. The remaining decrease of the spin length could be explained by a heating process that excites atoms to higher trap modes. Thereby, a fraction of the atoms would become distinguishable from the rest of the ensemble in the ground state. As the many-body state is then not fully symmetrised anymore, the maximal spin length would be reduced [54]. However, long holding times without a major reduction in spin length have been demonstrated in a similar system [64], and thus the issue must be of a technical rather than a fundamental origin. A technical approach to solve this problem is to further improve the stability of the optical dipole trap. This can be accomplished by exchanging critical opto-mechanical components to specifically temperature stable devices and by implementing a two-level intensity stabilisation, to enable a specific optimisation to the power range used when holding the atoms. In conclusion, the twin-Fock state before the transfer to momentum space can in principle offer higher generalised squeezing of at least  $-10$  dB and thereby enable a metrological gain of about 4 (6 dB) [53, 64].

The increased number fluctuations recorded in momentum space are explained by the residual noise in the Raman transfer, as the number squeezing conditional on the non-transferred atoms is similar to the result after free-fall only, just slightly increased due to the additional detection noise from the third detection mask. Assuming the number squeezing would only be limited by the realised detection noise, the fluctuations of 0.6% in the Raman transfer efficiency cause the ideal number squeezing to be reduced from  $-13$  dB to  $-9$  dB below shot-noise. This would still be a competitive value and illustrates the quality of the implemented Raman transfer. However, the transfer efficiency usually deteriorated within hours, which we assign to absolute and relative drifts in the intensity of the Raman light. As the intensity

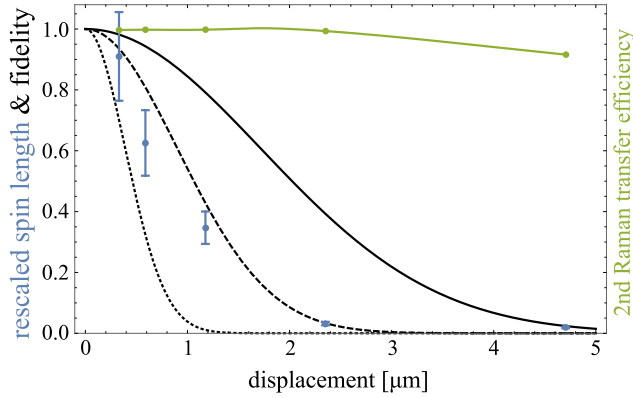


Figure 6.1: Spin length as a measure of the spatial overlap of matter waves. Upon displacement of the two twin modes, the experimentally measured spin length (blue data points) decreases quickly. The result is compared to a prediction which assumes the measured expansion rate (solid line), twice the measured value (dashed line) and the measured expansion without collimation (dotted line). To improve comparability, the spin length is rescaled such that the measured value after  $40\ \mu\text{s}$  is at 91 % of the ideal value (details see text). The frequency of the second Raman pulse was fixed here for simplicity, and thus the Doppler shift due to the slightly extended free fall decreases the transfer efficiency. However, the effect is too small to affect the spin length measurement. The theoretical analysis uses a one-dimensional analytic description of the expanding spatial mode based on the initial extent of the cloud and the residual expansion rate. Theory was kindly provided by Polina Feldmann and is based on Ref. [125].

after the final optical fibre is not stabilised (see Figure 5.3), a drift of the fibre coupling directly causes a common intensity drift. Also the polarisation could have drifted away from the maintaining axes of the optical fibres, which can cause relative intensity fluctuations via the PBS and in turn an imperfect compensation of the relative AC-Stark effect. The limited long-term stability of the existing Raman system also sets a practical limitation on the calibration (AC-Stark shift compensation, determining optimal frequency and pulse length), required to achieve highest transfer efficiencies. Therefore, a major technical improvement to our apparatus will be a new Raman system including a proper intensity stabilisation. The new Raman system has been thoroughly re-designed to meet the requirements of our experiment and showed promising performance in stand-alone characterisation measurements [118].

A proof of entanglement between modes that were completely separated for the measurement of both conjugate observables could be regarded as the next step towards an entanglement-enhanced atom interferometer. As a first measurement into this direction, the spin length  $\langle J_{\perp}^2 \rangle / (N/2(N/2 - 1))$  was recorded for extended waiting times between both Raman pulses, to allow the twin modes to move

apart. The detected spin length is expected to decline with growing separation, as the overlap of the spatial modes reduces and thus the fraction of atoms that are effectively coupled by the  $\pi/2$ -pulse decreases. Without any overlap, the  $\pi/2$ -pulse cannot couple the twin modes anymore and simply transfers half of each into the opposite spin state. Thus, speaking in the Bloch sphere picture, instead of rotating the twin-Fock ring upright, two single Fock states  $|N/2\rangle_A$  and  $|N/2\rangle_B$  are rotated independently from the poles of a half-sized Bloch sphere, towards the equator. The final outcome is similar to a [CSS](#) and shows a residual spin length  $(N/4)/(N/2(N/2 - 1)) \propto 1/N$  if the same measurement as for the twin-Fock state is performed. [Figure 6.1](#) shows the decrease of the measured spin length when extending the time between both Raman pulses, i. e. extending the separation of the twin modes. Here, the measured spin length was rescaled as if the initial value for vanishing separation would be ideal to improve comparability with the theoretical analysis. The measurement agrees qualitatively with a prediction based on a one-dimensional analytic description of the expanding spatial mode, depending on the initial extent of the cloud and the residual expansion rate [125]. The relative displacement of the twin modes causes a fast decline of the spin length which already vanishes at about  $3\ \mu\text{m}$  centre-of-mass separation. Therefore, also the observed reduction of the spin length by 9% in momentum space compared to the result after free fall only, could be explained by the slight displacement of  $0.5\ \mu\text{m}$ . Regarding the application in atom interferometry, an accurate spatial overlap during the final coupling pulse is crucial, not just to obtain a maximum contrast but also to detect with entanglement-enhanced performance.

From another perspective, the relatively high sensitivity of the spin length on the spatial mode overlap can be seen as a tool to precisely measure the fidelity of the spatial modes. Furthermore, in a scenario where interference with atoms in a specific spin state upon a [MW](#) or [RF](#) coupling should be avoided, but simply moving within the eight spin levels of  $^{87}\text{Rb}$  is not sufficient, the atoms could be slightly displaced by two successive Raman transfers to suppress the coupling to the rest of the ensemble. A [MW](#) or [RF](#) pulse would still manipulate the displaced atoms, but interference with the rest of the ensemble is switched off. Upon re-establishing the overlap of the modes, the coupling pulses cause interference again.

## 6.2 TOWARDS ENTANGLEMENT-ENHANCED GRAVIMETRY

Based on the protocol presented in [Figure 5.12](#), a full light-pulse atom interferometer to measure Earth's gravitational acceleration with entanglement-enhanced sensitivity can be realised. The enhancement by entanglement could balance the smaller ensemble size when using



BECs compared to thermal ensembles while at the same time allow to benefit from the excellent mode quality of a BEC. Employing BECs for gravimetry leads to a more precise control of the initial position and momentum of the atomic cloud, which reduces the uncertainty by gravity gradients and the Coriolis force. Furthermore, the Doppler spread and the sensing of phase and intensity gradients of the light fields is reduced.

First, both twin-Fock modes should predominantly populate the clock states during the gravimeter sequence, as otherwise the relative phase due to the gravitational acceleration is easily dominated by a (noisy) phase shift due to magnetic fields. In the realised protocol, one of the twin modes already populates the clock state  $|2,0\rangle$ . For usual magnetic field strengths and MW pulse lengths, a simple MW transfer of the other twin mode in  $|1,1\rangle$  via  $|2,1\rangle$  to the clock state  $|1,0\rangle$  is not possible without driving a relevant transfer on the near-resonant "cross" transition  $|2,0\rangle \leftrightarrow |1,1\rangle$ . An elegant way to avoid the unwanted transition would be the implementation of MW pulses with clean circular polarisation into our apparatus, as it already has been demonstrated with adequate efficiency and suppression of the unwanted transfer in a similar system [126]. The implementation of the required antenna would be in line with an upgrade of the MW source to a new system which has been recently developed in our group [127]. As an alternative, the magnetic field and the MW pulse length could be matched to the given shares of polarisations such that a  $\pi$ -pulse on the desired transfer  $|2,1\rangle \leftrightarrow |1,0\rangle$  exactly corresponds to a non-resonant pulse that drives a full oscillation on the cross transition. Also larger temporal changes of the magnetic field should not harm the entangled state after it has been released to free space. In the following, we call either way to suppress the effect of the "cross" transfer a selective MW pulse and assume this technique to perform on a similar noise level as the usual MW transfers, such that multiple pulses can be utilised without causing a major degradation of the entangled state.

The extension of the implemented protocol from Figure 5.12 to a potential entanglement-enhanced gravimeter is depicted in Figure 6.2. In principle, the first two counter-propagating Raman  $\pi$ -pulses have been implemented. Here, the twin modes are initially prepared in the clock states by one of the abovementioned techniques and undergo the required free fall of  $\sim 5$  ms to separate co- and counter-propagating transfer by the Doppler shift. Before the first counter-propagating pulse, a co-propagating  $\pi/2$ -pulse rotates the twin-Fock state upright such that it becomes phase sensitive.

For a direct extension of the scheme, all counter-propagating Raman pulses should only couple to the purple twin mode (depicted by the orange dots in Figure 6.2). To this end, relatively long and thus frequency selective Raman pulse that resolve the Doppler shift between the momentum transfers in opposite direction  $\pm 2\hbar k$  of  $2 \times 15$  kHz

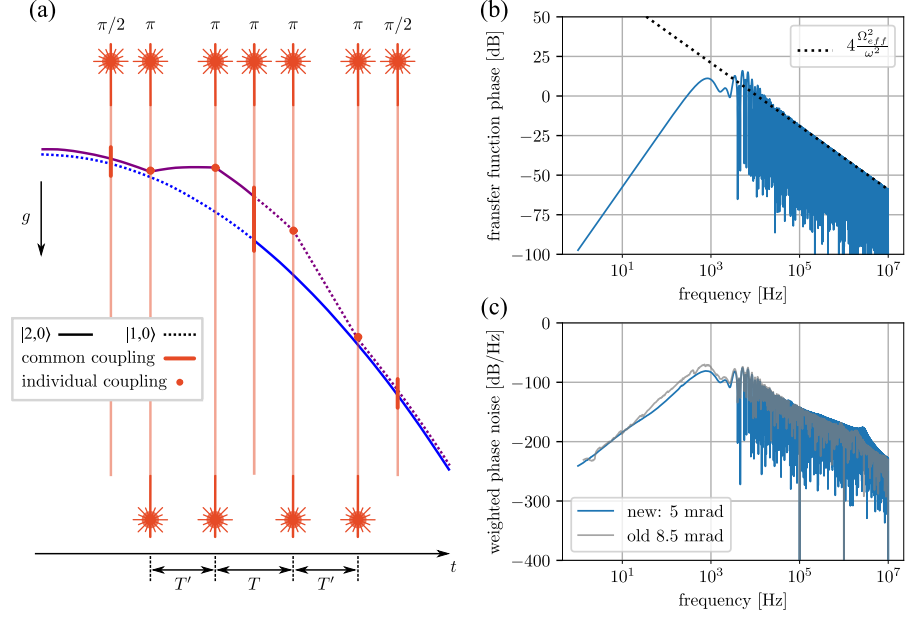


Figure 6.2: The envisaged entanglement-enhanced gravimeter is depicted in (a). Similar to the protocol realised in this work, one of the twin-modes is accelerated (purple trajectory) by counter-propagating Raman transfers to span an area in space-time with respect to the free fall trajectory of the other twin mode (dark blue). Both twin modes populate the clock states and a Raman pulse that resolves the Doppler-shift between opposite momentum transfers accelerates one of the modes. To invert the momentum kick, the internal spin states are commonly changed by co-propagating Raman transfers. The transfer function of this interferometer (b) is similar to a common Mach-Zehnder topology (see text) and the weighted phase noise (c) of the new Raman system integrates to 5 mrad. For comparison, the weighted phase noise for the Raman system employed until now is depicted as well. Here, assumed parameters are  $\tau_\pi = 90 \mu\text{s}$ ,  $T' = 1 \text{ ms}$  and  $T = 0 \text{ ms}$ . Figures (b) and (c) are kindly provided by Christophe Cassens [118].

could be employed. The length of efficient pulses is restricted by the velocity distribution of the atoms to around 3 times the pulse duration that has been implemented. Assuming further reduction of the residual expansion by a factor of  $1/2$  would allow for pulse durations of about  $6 \cdot 15 \mu\text{s} = 90 \mu\text{s}$  without additional losses due to velocity selection. Such pulses resolve  $1/90 \mu\text{s} \approx 11 \text{ kHz}$  and thus should allow to drive the momentum transfer for only one mode though both clock states are populated. The first counter-propagating Raman pulse accelerates the atoms in  $|2,0\rangle$  upwards. For the successive Raman transfers the selection of the mode by the Doppler shift is always possible, as both modes will either be in a different clock state or in a different momentum state.

After the second momentum transfer, which stops the relative motion of the clouds, both twin-modes would travel for a variable time  $T$

on different trajectories. At this point a co-propagating Raman pulse, which is not selective as no Doppler shift separates both possible transfers, interchanges the spin state, such that the following momentum transfer accelerates the purple mode back towards the blue mode. Interference of the modes does not happen here, as they do not spatially overlap yet. A fourth Raman pulse stops the relative motion of the modes at the point of maximal spatial overlap. A final co-propagating  $\pi/2$ -pulse closes the interferometer and maps the relative phase information onto the population imbalance of the clock states.

For completeness, a few possible modifications of the presented scheme should be mentioned. In the case that **MW** pulses are preferred, the co-propagating Raman pulses could in principle be replaced by a **MW** coupling of the clock states. Also could a combination of three **MW** pulses prior to each momentum transfer be employed to temporarily move the blue mode to a spin state which is not coupled to the Raman light (details in [Section A.1.1](#)), which provides an alternative way to achieve momentum transfer to one mode only. Alternatively, both modes could be accelerated symmetrically into opposite directions by a simultaneous resonant coupling of the clock states. In this case, rather short pulses, broad in frequency, have to be used to allow for a resonant driving of both transfers. A relatively broad resonance can also be achieved, if the frequency difference of the Raman lasers is swept to realise an adiabatic passage. This technique has been demonstrated with promising fluctuations of the transfer efficiency of  $\sim 1\%$  [124].

The relative phase imprinted on the twin-Fock modes by the gravimeter sequence depicted in [Figure 6.2](#) is given by [118]

$$\theta = -\frac{4\hbar k}{m}T' - 2kgT'(T' + T) + \phi_1 - \phi_2 - \phi_3 + \phi_4 \quad (6.1)$$

where  $T$  and  $T'$  are the free evolution time and the time between the pairs of counter-propagating Raman beams ([Figure 6.2](#)). The term depending on Earth's gravitational acceleration  $g$  is proportional to the area the two modes span in space-time. The phases  $\phi_{1,2,3,4}$  are the phases of the respective Raman laser pulses and  $k$  corresponds to the transferred photon momentum, which is  $\pm 2\hbar k$  for the counter-propagating Raman pulses. To estimate the limit on the phase sensitivity based on the performance of the new Raman system, the transfer function is computed and weighted with the measured phase noise between the two Raman lasers. [Figure 6.2](#) shows that the transfer function of the twin-Fock gravimeter is quite similar to the transfer function of a usual Mach-Zehnder like scheme (with similar timings and pulse lengths assumed). The gravimeter is sensitive to noise frequencies in a range determined by time  $T'$  between the Raman pulses and the pulse duration  $\tau$ , i. e. in the range from  $1/T' = 10^3\text{Hz}$  and  $1/\tau \approx 10^4\text{Hz}$ . Smaller noise frequencies cause changes which are

too slow for the interferometer to be affected. Noise with higher frequencies is time-averaged within the duration of the measurement. Weighting the phase noise of the new Raman system with this transfer function predicts an integrated phase noise of  $\sigma_{PN} = 5$  mrad for this specific implementation. By comparing to the SQL  $(\Delta\theta_{SQL})^2 / (\sigma_{PN})^2$  of  $10^4$  atoms we estimate to resolve a gain of 6 dB, thus the weighted phase noise might still set a considerable limit to the observable squeezing at the interferometers output. Also the phase noise caused by vibrations of the retro-reflective mirror is expected to set a bound at a comparable level.

Regarding a measurement only limited by the detection noise and the present Raman transfer efficiency and fluctuations, we expect that 93(2) % of the accelerated atoms reach the output state of the gravimeter and exhibit, together with the atoms at rest (in free-falling frame), a residual number squeezing of  $-7$  dB. If the fluctuations of each Raman transfer can be reduced by a conservative factor of  $1/2$  (to 0.3 %), the remaining number squeezing would already exceed  $-10$  dB. The spin length measurement is insensitive to fluctuations on this level and is mainly limited by the final spatial overlap. Summing up, by implementing the presented atom interferometer, a measurement of Earth's gravitational acceleration  $g$  with a sensitivity beyond the SQL is in reach.

The presented protocol is not limited to twin-Fock states but can in principle use all entangled states that can be prepared in the two clock states. For example, a spin-squeezed state could be utilised as input to the above gravimeter as follows. Starting with the initial ensemble coherently split onto the levels  $|1, \pm 1\rangle$  and vacuum in  $|1, 0\rangle$ , spin dynamics at  $q/|\Omega| = -1$  generates the one-mode squeezed vacuum in  $|1, 0\rangle$  as described in Section 3.4.3. The populations in  $|1, \pm 1\rangle$  are then transferred to  $|2, \pm 1\rangle$  and combined in  $|2, 0\rangle$  by an  $F$ -selective RF pulse to realise the squeezed vacuum in the upper clock state. Such selective RF pulses that only couple to a desired spin- $F$  manifold have already been demonstrated [97]. By another MW  $\pi/2$ -pulse on the clock transition with adequate phase, a phase sensitive spin-squeezed state can be prepared and used as entangled input state to the outlined gravimeter.

The absolute sensitivity of inertially sensitive atom interferometers will most likely benefit from entangled sources, if relative measurements are conducted with two or more atom interferometers at the same time. In those protocols, predominant noise sources, such as vibrations of retro-reflective optics, are suppressed by common-noise rejection and thus the sensitivity limit set by the SQL becomes relevant. Exemplary applications are gravity gradiometers [38] or future atomic gravitational wave detectors [128, 129].

## 6.3 SKETCH OF A SCALABLE ATOMIC BELL TEST

The ability to coherently separate highly entangled ensembles in space is also interesting for applications beyond entanglement-enhanced metrology. For example, atom interferometers employing squeezed BECs and spatial separation on the  $\mu\text{m}$  scale have been proposed to probe and potentially rule out collapse models, extensions of quantum mechanics that try to shed some light on the quantum-to-classical transition [130].

Another compelling question is, whether the intriguing features of quantum mechanics are just based on ignorance, i. e. could be avoided by using a classical theory with local hidden variables, or the quantum description is actually necessary. In 1964, John Stewart Bell proposed a setup where the outcome predicted by quantum mechanics is inconsistent with the prediction of any classical local theory, thereby enabling to answer the question by conducting so-called Bell test experiments [3]. Even though the assumption of locality (no interaction faster than light) and realism (the ability to assume properties of a system to exist previous to a measurement) should intuitively hold, many impressive Bell tests showed clear agreement with the quantum description, ruling out local realism to be fundamentally valid. A few years ago, the first Bell tests closing all three major loopholes were reported [4–6]. As most Bell tests so far, these used photonic systems. The realised atomic Bell tests, as sophisticated as they are, only used small systems such as a few ions [131] or single neutral atoms [132]. Larger rather macroscopic atomic systems such as a thermal cloud of atoms or a BEC have been shown to exhibit Bell correlations [133, 134], i. e. the strongest type of entanglement required to conduct a Bell test. However, as typical to these systems, only collective measurements could be performed and no spatial separation of subsystems was realised. Yet, both is required for an actual Bell test.

The techniques presented in this thesis can be used to implement a Bell test with a free-falling BEC of thousands of atoms. In principle, each of the two modes of a twin-Fock state is split and spatially separated. The split portions then meet with their counterpart and undergo a local MW coupling before being measured. The basic idea of such a Bell test using Fock states was formulated by Yurke and Stoler [135] and later extended to independent many particle Fock states by Laloë and Mullin [136]. A possible implementation in our system by using the implemented Raman transfers will be briefly sketched in the following. The envisioned scheme breaks down into five steps:

1. Preparation of a twin-Fock state in the levels  $|1, \pm 1\rangle$ .
2. Successive momentum transfer of 50 % of each twin mode.

3. A variable waiting time defines the spatial separation of the accelerated twin-mode portions and the portions at rest (free-falling frame).
4. Inverse momentum transfer to the firstly accelerated mode to achieve spatial overlap of both accelerated portions.
5. Local readout by MW coupling between the portions in (A) and (B) respectively.

The scheme is sketched in Figure 6.3. A twin-Fock state is prepared by the quasi-adiabatic procedure in the states  $|1, \pm 1\rangle$  and released to free fall, representing the source S. Then, a combination of a MW  $\pi/2$ -pulse and a Raman  $\pi$ -pulse transfers  $2\hbar k$  momentum to half of the twin mode in  $|1, -1\rangle$ . Prior to the next Raman pulse, a sequence of MW pulses is employed to move 50% of the other twin mode to  $|2, 0\rangle$ . As the coupling between displaced modes is switched off (Figure 6.1), the spin state of two modes can be exchanged with a MW  $\pi$ -pulse without causing interference. The full scheme is rather technical and discussed in detail in Section A.1.2. Another Raman pulse transfers momentum to a half portion of the second twin mode, such that now two portions are at rest (blue) and the other two portions separate with  $2\hbar k/m$  (purple). The following MW pulse sequences are used

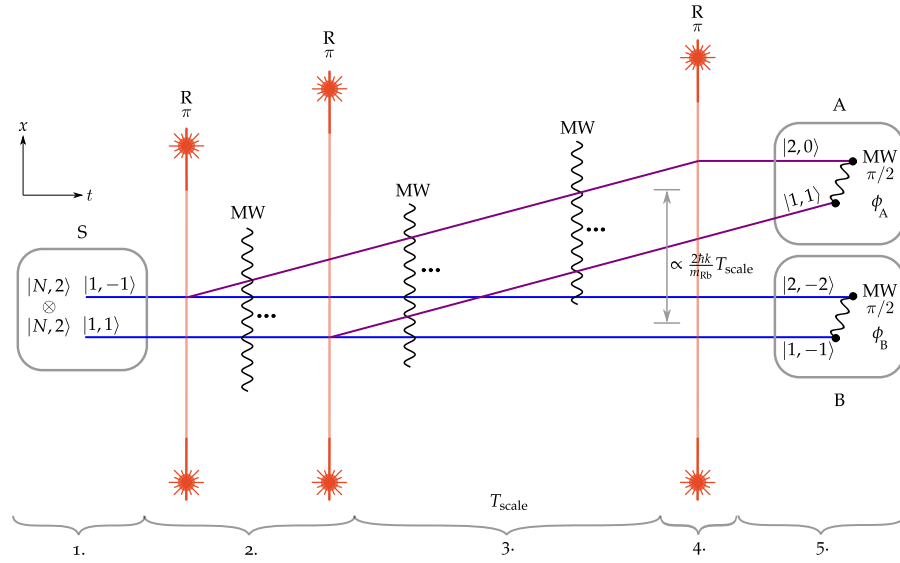


Figure 6.3: Sketch of a scalable atomic Bell test based on the demonstrated techniques. The source S is a clean twin-Fock state in spin space. One half of each twin mode is spatially separated from the other half by a counter-propagating Raman pulse. To this end, the spin states have to be modified by several MW pulses (here only indicated, for details see Section A.1.2). The final states in site A and site B are separated by a scalable distance and allow for independent local readout as they couple to different MW frequencies.

to bring the firstly accelerated atoms to the level  $|1, 0\rangle$ , such that the momentum transfer can be reversed and spatial overlap of both purple portions can re-establish. Also the different modes are transferred by the MW pulses to their final spin configuration. The time when the last Raman pulse is applied determines the final separation between the purple modes in site A and the blue modes in site B. Finally, two independent MW couplings can be applied with individual phases  $\phi_A$  and  $\phi_B$ .

In total, the scheme requires three counter-propagating Raman  $\pi$ -pulses and 15 MW pulses. The number of MW pulses seems ambitious. However, most of the couplings are simple  $\pi$ -pulses which could only add noise via fluctuations in the transfer efficiency, which is typically very low. As an alternative, the protocol can be further reduced in complexity by employing the abovementioned techniques of polarisation-selective MW or  $F$ -selective RF transfers.

Magnetic field noise should not be detrimental to the scheme as the twin-Fock state on the equator is inherently phase insensitive. In doubt about the influence of magnetic field noise, the whole scheme takes less than 1 ms, which is still short enough to be relatively robust to magnetic field noise. In our experiment, the signal of an interferometer between magnetic field sensitive states was observed to retain for at least 2 ms evolution time. However, a thorough noise analysis and based on this, an optimal choice of local operations, observables, the actual inequality to violate and the ability to close loopholes using this scheme should be done, but is beyond the scope of this thesis. Also, the possibility of relaxing the prerequisite for single atom detection (as Alice' and Bob's twin-Fock states are not independent here) remain open questions. Concerning the matter of detection, a two-mode squeezed state [62] might be employed instead of a twin-Fock state to realise a Bell test based on homodyne detection of continuous variables [137–139].

If a Bell test along the line of the presented protocol is implemented in our apparatus, the separation of sites A and B could be scaled up to hundreds of  $\mu\text{m}$ . In the 10 m atomic fountain experiment in Stanford, the coherent separation of two modes of a BEC by more than half a meter and a successive recombination has been demonstrated [140]. Therefore, the spatial separation of the entangled BEC-modes is in principle scalable up to the m scale. Experiments which can bring the non-classical features of many-body entangled quantum states to the macroscopic world are in reach, as the combination of entangled ultra-cold sources and the ability of macroscopic separation is actively pursued at facilities such as the Very Large Baseline Atom Interferometer (VLBAI) in Hannover.





## APPENDIX

## A.1 DETAILS ON ENVISIONED PROTOCOLS

A.1.1 *Alternative implementation of the gravimeter*

To directly extend the realised protocol to a gravimeter where the atoms predominantly populate the clock states, the momentum transfer needs to be restricted to one of the twin modes only. Alternatively to use Raman pulses that resolve the Doppler shift between momentum transfers in opposite directions, one of the two modes could be moved to a spin state that does not couple to the Raman light.

To this end, three MW pulses can be utilised around each momentum transfer as follows. The blue mode has to temporarily leave the clock state by a selective MW transfer from  $|1, 0\rangle$  to  $|2, 1\rangle$ . After the counter-propagating  $\pi$ -pulse transferred the purple mode from  $|0\hbar k; 2, 0\rangle$  to  $|2\hbar k; 1, 0\rangle$ , a simple MW transfer on the clock transition reverts the spin change and gives way to the blue mode to be transferred back to its initial clock state  $|1, 0\rangle$  by another selective MW coupling. To transfer momentum into the opposite direction, the MW transfer on the clock transition is implemented before the Raman transfer. Assuming the typical short pulse times here, the blue mode stays about  $50\ \mu\text{s}$  in a magnetically sensitive state for each procedure. As there are four momentum transfers involved in the scheme, the time in magnetically sensitive states sums up to about  $200\ \mu\text{s}$ , which is 10 % of the minimal envisaged interferometer time and thus should have a relatively small effect on the measured phase.

A.1.2 *Detailed protocol of the sketched Bell test*

The detailed scheme of the envisioned Bell test is visualised in [Figure A.1](#). A twin-Fock state is prepared by the quasi-adiabatic procedure in the states  $|1, \pm 1\rangle$  and released to free fall. Then, a combination of a MW  $\pi/2$ -pulse and a Raman  $\pi$ -pulse transfers  $2\hbar k$  momentum to half of the twin mode in  $|1, -1\rangle$ . As now all desired atoms are in  $F = 1$ , the left-over atoms from the Raman transfer can be removed from the ensemble by a cleaning light-pulse. Then, the accelerated atoms in  $|1, 0\rangle$  are transferred back to  $|2, 0\rangle$ . The accelerated mode (purple) is displaced from the modes at rest (blue) and a MW  $\pi$ -pulse simply interchanges their spin state such that the untouched twin mode populates  $|2, 0\rangle$ . One half of this twin mode is then accelerated and moved back to  $|2, 0\rangle$  similar as for the other twin mode before.

Here, cleaning the potential left-overs from the Raman transfer is not possible by the usual light pulses anymore, as four modes cannot populate the three available levels of  $F = 1$ . However, the left-over atoms will finally end up in otherwise unpopulated spin states or at a different position, such that they do not cause any problem but give extra information about the Raman transfer.

The remaining MW pulses are employed to enable a deceleration of the firstly accelerated twin portion and to move the four modes to spin states that allow for local operations in sites A and B before the final detection. After waiting again for sufficient displacement, the spin state of the just accelerated mode is interchanged with its resting counterpart. Then, two more simple MW  $\pi$ -pulses move the blue modes to their final spin configuration. As the two purple modes are also sufficiently displaced from each other at this point, another spin-state interchanging pulse can be employed here. Another three usual MW  $\pi$ -pulses transfer the firstly accelerated mode to  $|1, 0\rangle$  and the other purple mode to its final spin state  $|1, 1\rangle$ . A final Raman pulse decelerates the atoms in  $|1, 0\rangle$  to allow to establish spatial overlap of the purple modes again. The time when the last Raman pulse is applied determines the final separation of the purple modes in site A and the blue modes in site B. Finally, two independent MW couplings can be applied with individual phases  $\phi_A$  and  $\phi_B$ .

## A.2 AUXILLARY MEASUREMENTS

### A.2.1 Effective quadratic Zeeman shift vs. set voltage

For a proper fit in Figure 4.1, the effective quadratic Zeeman shift upon MW dressing on the transition  $|1, 0\rangle \leftrightarrow |2, 0\rangle$  has to be expressed as a function of the voltage which sets the power of the dressing MW. To this end, the dependence of the dressing MW power on the setpoint voltage of the PI is measured and fitted.

In general, the Rabi frequency is proportional to the power of the MW,  $\Omega_{\text{MW}} \propto \sqrt{P_{\text{MW}}}$ . Here, the above fit function is used to define the Rabi frequency as a function of  $V_{\text{set}}$  and a  $\pi$ -pulse time  $t_\pi$  as

$$\Omega_{\text{MW}}(V_{\text{set}}, t_\pi) = \frac{\pi}{t_\pi} \sqrt{\frac{P_{\text{MW}}(V_{\text{set}})}{P_0}} \quad (\text{A.1})$$

with  $P_0 = P_{\text{MW}}(0.6)$ . The time  $t_\pi$  could in principle be determined experimentally but is left as a fit parameter. Finally, the effective quadratic Zeeman shift writes as

$$q(V_{\text{set}}, t_\pi) = q_B - q_{\text{MW}}(V_{\text{set}}, t_\pi) = \frac{(g\mu_B B)^2}{\Delta\nu_{\text{hf}}} - \frac{\Omega_{\text{MW}}^2(V_{\text{set}}, t_\pi)}{2\pi 4\delta} \quad [\text{Hz}], \quad (\text{A.2})$$

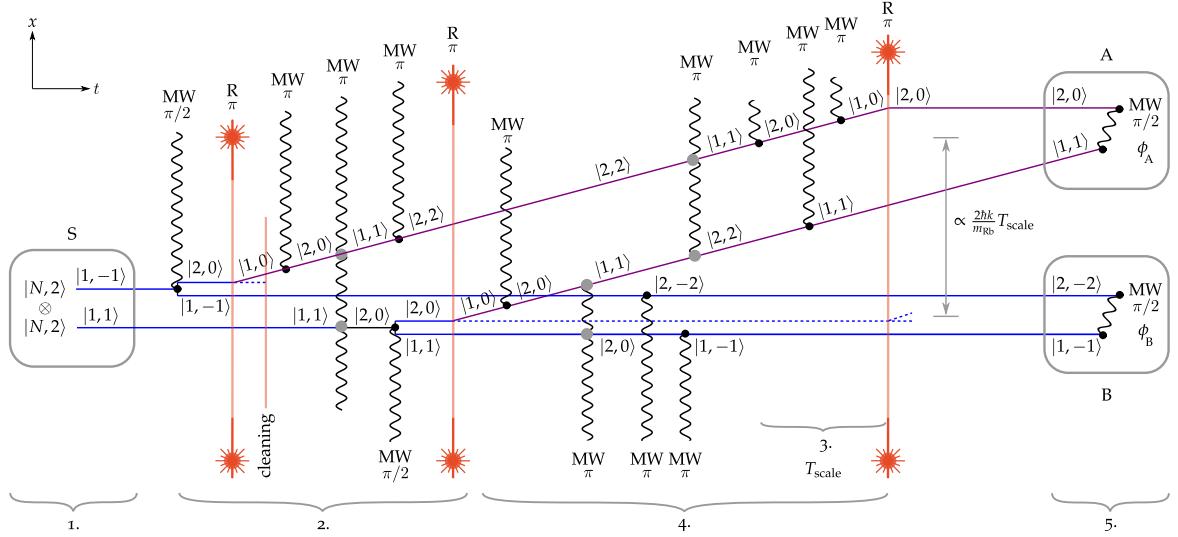


Figure A.1: Detailed sketch of a scalable atomic Bell test based on the demonstrated techniques. The source S is a clean twin-Fock state in spin space. One half of each twin mode is spatially separated from the other half. Here, a key feature is the switched off coupling between displaced modes, which allows to exchange the spin state of two modes with a MW  $\pi$ -pulse without causing interference (the specific transfers are marked with grey dots). The final states in site A and site B are separated by a scalable distance and allow for independent local readout as they couple to different MW frequencies.

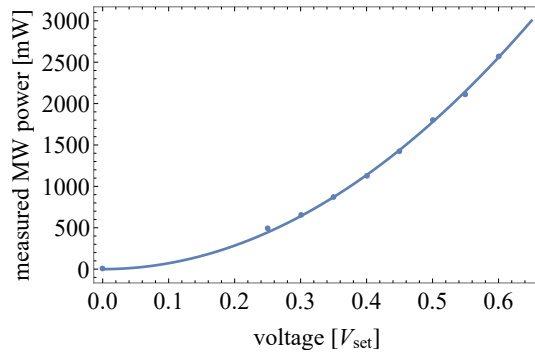


Figure A.2: The power of the dressing MW is measured directly before the antenna as a function of the voltage  $V_{\text{set}}$  that constitutes the actual value of the PI controller. The solid line represents a quadratic fit which gives  $P_{MW}(V_{\text{set}}) = 7105.54 \cdot V_{\text{set}}^2$ .

$$g = -1/2$$

approximate Landé g-factor

$$\mu_B = 1.399\,624\,604 \times 10^6 \text{ Hz/G}$$

Bohr Magneton

where  $B = 0.73 \text{ G}$

absolute magnetic field

$$\Delta\nu_{\text{hf}} = 6.834 \times 10^9 \text{ Hz}$$

frequency of the hyperfine splitting

$$\delta = 400 \times 10^3 \text{ Hz}$$

detuning w.r.t. clock transition

To calibrate  $q/|\Omega|$  in Figure 4.1 we use the fit function

$$f(V_{\text{set}}, t_\pi, \Omega) = \frac{q(V_{\text{set}}, t_\pi)}{\Omega},$$

where  $t_\pi$  and  $\Omega$  are fit parameters. Varying  $\Omega$  results in a different slope of the function, whereas varying  $t_\pi$  shifts the function up and down. Therefore both variables can be independently determined by the fit. The fit of [Figure 4.1](#) gives  $\Omega = 5.6(2)$  Hz and  $t_\pi = 143.4(6)$  ms.

#### A.2.2 Detection noise vs. measured cloud size

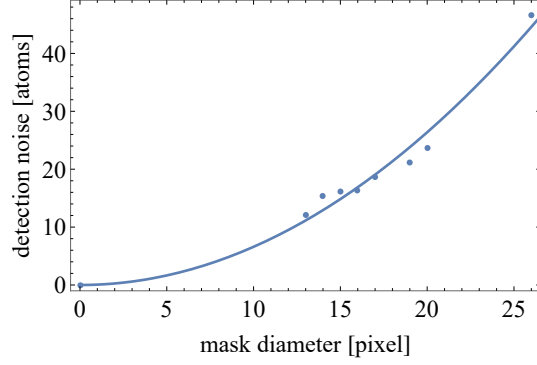


Figure A.3: The dependence of the detection noise per mask as function of the mask diameter is characterised by evaluating empty absorption images. The solid line represents a quadratic fit.

The detection noise per mask is determined by evaluating empty absorption images with detection masks of different size. The data points are fitted with the expected quadratic relation to achieve a continuous mapping from the extrapolated cloud size to the respective detection noise in [Figure 5.8b](#). The fit function in [Figure A.3](#) is given by

$$\sigma_{\text{detection}} = 0.066(2) \left[ \frac{\text{atoms}}{\mu\text{m}^2} \right] d_{\text{mask}}^2. \quad (\text{A.3})$$

In the experiment, we determine the size of the atomic cloud by fitting a Gaussian to the measured 2D-density and computing its standard deviation  $\sigma_{\text{cloud}}$ . To map this cloud size onto a realistic size of the detection mask  $d_{\text{mask}}$  in pixel, we experimentally optimise the mask size for each collimation-pulse duration in [Figure 5.8a](#). The mean translation factor is calculated as

$$f_{\text{cloud to mask size}} = \left( \sum_{i=1}^n \frac{d_{\text{mask}}^{(i)}}{\sigma_{\text{cloud}}^{(i)}} \right) / n = 1.092(6) \frac{\text{pixel}}{\mu\text{m}}. \quad (\text{A.4})$$

In this way, we average over artefacts of the mode preparation that result in slight deformations of the clouds and thus the need for slightly larger detection masks is some cases.

### A.3 DETAILS ON SIMULATIONS AND CALCULATIONS

#### A.3.1 Definition of the Wigner function on the Bloch sphere

The Wigner function shown on the Bloch spheres in [Section 2.1.2](#) are computed using the formula [\[25\]](#)

$$W(\varphi, \vartheta) = \sqrt{\frac{N+1}{4\pi}} \sum_{k,q} \text{Tr} \left( \rho T_{kq}^\dagger \right) Y_{kq}(\vartheta, \varphi) \quad (\text{A.5})$$

where  $Y_{kq}(\vartheta, \varphi)$  are spherical harmonic functions and  $T_{kq}^\dagger$  are spherical tensor operators. The tensor operators are given by Clebsch-Gordan coefficients and Dicke states [\[25\]](#)

$$T_{kq}^{(J)} = \sum_{m,m'=-J}^J (-1)^{J-m'} \langle J, m; J, -m' | k, q \rangle |J, m\rangle \langle J, m'| \quad (\text{A.6})$$

where with  $J = N/2$  we identify  $|J, m\rangle = |N/2 + m, N/2 - m\rangle$ . Since the density operator can be decomposed in the basis of spherical tensor operators  $\rho = \sum_{k,q} \langle T_{kq}^\dagger \rangle T_{kq}$ , the Wigner distribution can be regarded as a one-to-one representation of the state  $\rho$ . The distribution sums up to one  $\int d\varphi \int d\vartheta W(\varphi, \vartheta) = 1$  but in contrast to a real probability distribution it can show negative values. These negative values are often connected to non-classical features and can lead to an intuitive understanding of the phase sensitivity of highly-entangled states.

#### A.3.2 Numerical simulation of spin dynamics

To numerically solve the time evolution with the Hamiltonian [3.3](#) the states and the Hamiltonian are represented in the reduced basis  $|k, N-2k, k\rangle = |k\rangle_{-1} \otimes |N-2k\rangle_0 \otimes |k\rangle_1$  which has the dimension  $N/2 + 1$  instead of  $\binom{N+3-1}{3-1} \propto N^2/2$  for a full three-mode description (similar as in Ref. [\[101\]](#)). By calculating

$$\begin{aligned} & a_0 a_0^\dagger a_{+1}^\dagger a_{-1}^\dagger |k, N-2k, k\rangle \\ &= \sqrt{N-2k} \sqrt{N-2k-1} (k+1) |k+1, N-2k-2, k+1\rangle \quad (\text{A.7}) \end{aligned}$$

$$\begin{aligned} & a_0^\dagger a_0^\dagger a_{+1} a_{-1} |k, N-2k, k\rangle \\ &= \sqrt{N-2k+1} \sqrt{N-2k+2k} |k-1, N-2k+2, k-1\rangle \quad (\text{A.8}) \end{aligned}$$

$$\hat{N}_0 |k, N-2k, k\rangle = (N-2k) |k, N-2k, k\rangle \quad (\text{A.9})$$

$$\hat{N}_{+1/-1} |k, N-2k, k\rangle = k |k, N-2k, k\rangle \quad (\text{A.10})$$

and neglecting terms proportional to  $\hat{N}_{+1} - \hat{N}_{-1}$ , that is restricting the analysis to states with vanishing magnetisation, the Hamiltonian 3.3 is expressed as a  $(N/2 + 1) \times (N/2 + 1)$  dimensional tridiagonal matrix

$$\begin{aligned} H_{ik} &= \delta_{ik} (\lambda(2(N - 2k) - 1) + q) 2k \\ &+ \delta_{i,k+1} \sqrt{N - 2k} \sqrt{N - 2k - 1} (k + 1) \\ &+ \delta_{i,k-1} \sqrt{N - 2k + 1} \sqrt{N - 2k + 2} k. \end{aligned} \quad (\text{A.11})$$

For implementation, sparse matrices of the Python SciPy library are utilised, as this allows to convert the self defined states and operators into QuTip objects and to use the QuTip time evolution solver [141].

Atom loss is modelled by introducing a time-dependence for the spin-dynamics rate  $\Omega$  or the interaction parameter  $\lambda$  respectively via the decreasing total atom number. In our system, the initial decrease in the atom number is mainly caused by three-body losses and experimentally determined to be described by

$$N(t) = 0.62N_0 e^{-t/\tau} + 0.38N_0 \quad (\text{A.12})$$

with a life time of  $\tau = 6.3$  s. The time-dependence of  $\Omega$  and  $\lambda$  are given by their scaling with the total atom number, i. e.

$$\Omega(t) = \Omega_0 \cdot (N(t)/N_0)^{2/5} \quad (\text{A.13})$$

and

$$\lambda(t) = \lambda_0 \cdot (N(t)/N_0)^{-3/5} \quad (\text{A.14})$$

respectively.

### A.3.3 Calculating the AC-Stark shift

The atom-light interaction in a three level system is thoroughly presented in [115]. Here, the resulting formulae for the AC-Stark shift shall be explicitly expressed with the different polarisation components to properly describe the asymmetric laser geometry used in this work.

The differential AC-Stark shift is defined as  $\Delta^{\text{AC}} = \delta_e^{\text{AC}} - \delta_g^{\text{AC}}$ . The individual shifts of the state  $|g\rangle$  and  $|e\rangle$  can be written as

$$\delta_g^{\text{AC}} = \frac{|\Omega_1|^2}{4} \sum_{\sigma_1} \sum_{F'=0}^3 \frac{\sum_{m'_F=-F'}^{F'} |\langle F', m'_F | F=1, m_F=0; 1, \sigma \rangle S_{FF'}|^2}{\Delta - \Delta_{F'}} \quad (\text{A.15})$$

$$+ \frac{|\Omega_2|^2}{4} \sum_{\sigma_2} \sum_{F'=0}^3 \frac{\sum_{m'_F=-F'}^{F'} |\langle F', m'_F | F=1, m_F=0; 1, \sigma \rangle S_{FF'}|^2}{\Delta - \Delta_{F'} - \nu_{\text{hf}}} \quad (\text{A.16})$$

$$\delta_e^{\text{AC}} = \frac{|\Omega_1|^2}{4} \sum_{\sigma_1} \sum_{F'=0}^3 \frac{\sum_{m'_F=-F'}^{F'} |\langle F', m'_F | F=2, m_F=0; 1, \sigma \rangle S_{FF'}|^2}{\Delta - \Delta_{F'} + \nu_{\text{hf}}} \quad (\text{A.17})$$

$$+ \frac{|\Omega_2|^2}{4} \sum_{\sigma_2} \sum_{F'=0}^3 \frac{\sum_{m'_F=-F'}^{F'} |\langle F', m'_F | F=2, m_F=0; 1, \sigma \rangle S_{FF'}|^2}{\Delta - \Delta_{F'}} \quad (\text{A.18})$$

where the Clebsch-Gordan coefficients are defined as explicitly stated in [142]<sup>1</sup>. The range of the sum over the polarisations is  $\sigma_1 = \{1\}$  and  $\sigma_2 = \{-1, 1\}$  for the asymmetric laser configuration and  $\sigma_1 = \sigma_2 = \{-1, 1\}$  for the symmetric setting. The relative hyperfine transition strength factors  $S_{FF'}$  are given by

$$\begin{array}{c|cccc} & F' = 0 & F' = 1 & F' = 2 & F' = 3 \\ \hline F = 1 & \sqrt{1/6} & \sqrt{5/12} & \sqrt{5/12} & 0 \\ F = 2 & 0 & \sqrt{1/20} & \sqrt{1/4} & \sqrt{7/10} \end{array}. \quad (\text{A.19})$$

The  $\Delta_{F'}$  are defined to be the detuning from the  $F' = 1$  level, that is  $\Delta_{F'=0} = -72.218$  MHz,  $\Delta_{F'=1} = 0$  MHz,  $\Delta_{F'=2} = 156.947$  MHz and  $\Delta_{F'=3} = 156.947 + 266.65$  MHz. For the calculation of the differential shift, the Rabi frequencies are estimated to be  $\Omega_1 \approx \Omega_2 \approx 4.5 \times 10^7$  Hz, which via

$$\Omega_0 = \frac{\Omega_1 \Omega_2}{2} \left( \frac{1}{24\Delta} + \frac{1}{8(\Delta - \Delta_2)} \right) \quad (\text{A.20})$$

gives  $\pi$ -pulse times of about 15  $\mu$ s.

The differential shift for the asymmetric laser geometry evaluates to

$$\Delta^{\text{AC}} = \frac{1}{960} \left( 2 \left( \frac{25}{-\Delta + \nu_{\text{hf}}} + \frac{1}{\Delta} + \frac{15}{\Delta - \Delta_2} + \frac{15}{-\Delta + \Delta_2 + \nu_{\text{hf}}} + \frac{24}{\Delta - \Delta_3} \right) |\Omega_2|^2 \right) \quad (\text{A.21})$$

$$+ \left( -\frac{25}{\Delta} + \frac{1}{\Delta + \nu_{\text{hf}}} + \frac{15}{\Delta - \Delta_2 + \nu_{\text{hf}}} + \frac{15}{-\Delta + \Delta_2} + \frac{24}{\Delta - \Delta_3 + \nu_{\text{hf}}} \right) |\Omega_1|^2 \quad (\text{A.22})$$

where the result for the symmetric configuration is attained by simply dropping the single factor 2 and exchanging the pre-factor 1/960 by 1/480.

The differential shift vanishes if the individual shifts are equal. From  $\delta_g^{\text{AC}} = \delta_e^{\text{AC}}$  the desired intensity ratio for the asymmetric geometry explicitly writes as

$$\frac{I_2}{I_1} = \frac{1}{4} \frac{\left( \frac{1}{240(\Delta + \nu_{\text{hf}})} + \frac{1}{16(\Delta - \Delta_2 + \nu_{\text{hf}})} + \frac{1}{10(\Delta - \Delta_3 + \nu_{\text{hf}})} \right) - \left( \frac{5}{48\Delta} + \frac{1}{16(\Delta - \Delta_2)} \right)}{\left( \frac{5}{24(\Delta - \nu_{\text{hf}})} + \frac{1}{8(\Delta - \Delta_2 - \nu_{\text{hf}})} \right) - \left( \frac{1}{120\Delta} + \frac{1}{8(\Delta - \Delta_2)} + \frac{1}{5(\Delta - \Delta_3)} \right)} \quad (\text{A.23})$$

where the solution for the symmetric geometry only differs by a factor 1/2 in the numerator.  $\Delta^{\text{AC}}$  and  $\frac{I_2}{I_1}$  are shown in Figure 5.4 in the main text.

The frequencies of the Raman lasers with respect to the absorption spectrum of Rubidium is shown in Figure A.4.

<sup>1</sup> The Clebsch-Gordan coefficients explicitly shown in the Appendix of reference [115] are a factor 2 larger. If these are used, the above equations must be multiplied by a global factor of 1/2. When calculating the differential shift or intensity ratios, this factor cancels anyway.

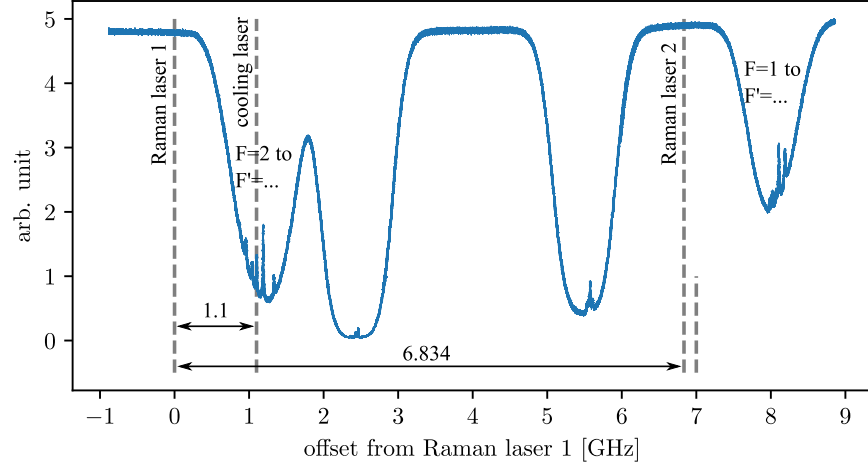


Figure A.4: Absolute position of the Raman laser frequencies within the spectrum of Rubidium. The cooling laser is locked onto the  $^{87}\text{Rb}$  cross-over transition  $|5^2S_{1/2}; F=2\rangle \leftrightarrow |5^2P_{3/2}; F'=c.o.1-3\rangle$  and due to proper frequency shift by two AOMs runs at the frequency of the transition  $|5^2S_{1/2}; F=2\rangle \leftrightarrow |5^2P_{3/2}; F'=3\rangle$ . This laser serves as absolute frequency reference for the Raman system. Raman laser 1 is locked onto the cooling laser with a red detuning of about 1.1 GHz. The phase lock stabilises Raman laser 2 about 6.834 GHz blue detuned with respect to Raman laser 1.

#### A.3.4 Velocity selection of Raman transfers

The frequency distribution of the applied  $\sin^2$  pulses can with good agreement be described by

$$S(\nu, \tau) = P_0 e^{-\frac{\nu^2}{2(0.6/\tau)^2}} \quad (\text{A.24})$$

where  $\tau$  is the pulse time and  $P_0$  the transfer probability for a neglectable velocity width, i. e. for a short pulse time. Alternatively, a fit to an actually measured spectroscopy is used when available. The velocity distribution of the ensemble is describe by a Gaussian function

$$V(\nu, \sigma_\nu) = \frac{1}{\sqrt{2\pi\sigma_\nu^2}} e^{-\frac{\nu^2}{2\sigma_\nu^2}} \quad (\text{A.25})$$

where  $\sigma_\nu$  is the measured velocity width, i. e. the rate of change of the width of a Gaussian fit onto the density profile of the free falling ensemble. The velocity width directly translates into a corresponding frequency width  $D(\nu, \sigma_\nu)$  due to the Doppler effect by using  $\sigma_\nu = -\sigma_v/\lambda$ , where  $\lambda = 780.24 \text{ nm}$  is the wavelength of the Raman lasers.

The distribution of Doppler shifts after a (potentially velocity selective) Raman transfer is given by

$$\sigma_\nu^{\text{selected}} = \int \nu^2 S(\nu, \tau) D(\nu, \sigma_\nu) d\nu \quad (\text{A.26})$$



and the maximum expected transfer probability is

$$P_{\max}(\sigma_v) = \int S(v, \tau) V(v, \sigma_v) dv. \quad (\text{A.27})$$



## BIBLIOGRAPHY

---

- [1] E. Schrödinger. “Die gegenwärtige Situation in der Quantenmechanik.” In: *Naturwissenschaften* 23.48 (1935), pp. 807–812. ISSN: 0028-1042. DOI: [10.1007/BF01491891](https://doi.org/10.1007/BF01491891).
- [2] A. Einstein, B. Podolsky, and N. Rosen. “Can quantum-mechanical description of physical reality be considered complete?” In: *Phys. Rev.* 47.10 (1935), pp. 777–780. DOI: [10.1103/PhysRev.47.777](https://doi.org/10.1103/PhysRev.47.777).
- [3] John S Bell. “On the Einstein-Podolsky-Rosen paradox.” In: *Physics* 1.3 (1964), pp. 195–200.
- [4] Lynden K. Shalm et al. “Strong Loophole-Free Test of Local Realism.” In: *Phys. Rev. Lett.* 115 (25 2015), p. 250402. DOI: [10.1103/PhysRevLett.115.250402](https://doi.org/10.1103/PhysRevLett.115.250402). URL: <http://link.aps.org/doi/10.1103/PhysRevLett.115.250402>.
- [5] Marissa Giustina et al. “Significant-Loophole-Free Test of Bell’s Theorem with Entangled Photons.” In: *Phys. Rev. Lett.* 115 (25 2015), p. 250401. DOI: [10.1103/PhysRevLett.115.250401](https://doi.org/10.1103/PhysRevLett.115.250401). URL: <http://link.aps.org/doi/10.1103/PhysRevLett.115.250401>.
- [6] B. Hensen et al. “Loophole-free Bell inequality violation using electron spins separated by 1.3 kilometres.” In: *Nature* 526.7575 (2015), pp. 682–686. ISSN: 0028-0836. DOI: [10.1038/nature15759](https://doi.org/10.1038/nature15759).
- [7] Marek Żukowski and Časlav Brukner. “Quantum non-locality—it ain’t necessarily so...” In: *Journal of Physics A: Mathematical and Theoretical* 47.42 (2014), p. 424009. DOI: [10.1088/1751-8113/47/42/424009](https://doi.org/10.1088/1751-8113/47/42/424009). URL: <https://doi.org/10.1088/1751-8113/47/42/424009>.
- [8] Adam M. Kaufman, M. Eric Tai, Alexander Lukin, Matthew Rispoli, Robert Schittko, Philipp M. Preiss, and Markus Greiner. “Quantum thermalization through entanglement in an isolated many-body system.” In: *Science* 353.6301 (2016), pp. 794–800. ISSN: 0036-8075. DOI: [10.1126/science.aaf6725](https://doi.org/10.1126/science.aaf6725). eprint: <http://science.sciencemag.org/content/353/6301/794.full.pdf>. URL: <http://science.sciencemag.org/content/353/6301/794>.
- [9] C. Neill et al. “Ergodic dynamics and thermalization in an isolated quantum system.” In: *Nature Physics* 12.11 (2016), pp. 1037–1041. ISSN: 1745-2481. DOI: [10.1038/nphys3830](https://doi.org/10.1038/nphys3830). URL: <https://doi.org/10.1038/nphys3830>.

- [10] Carl A. Kocher and Eugene D. Commins. "Polarization Correlation of Photons Emitted in an Atomic Cascade." In: *Phys. Rev. Lett.* 18 (15 1967), pp. 575–577. DOI: [10.1103/PhysRevLett.18.575](https://doi.org/10.1103/PhysRevLett.18.575). URL: <https://link.aps.org/doi/10.1103/PhysRevLett.18.575>.
- [11] David C. Burnham and Donald L. Weinberg. "Observation of Simultaneity in Parametric Production of Optical Photon Pairs." In: *Phys. Rev. Lett.* 25.2 (July 1970), pp. 84–87. ISSN: 0031-9007. DOI: [10.1103/PhysRevLett.25.84](https://doi.org/10.1103/PhysRevLett.25.84).
- [12] Ludwig Zehnder. "Ein Neuer Interferenzrefraktor." In: *Zeitschrift für Instrumentenkunde* 11.8 (1891), pp. 275–285.
- [13] Vladimir B Braginskii and Yurii I Vorontsov. "Quantum-mechanical limitations in macroscopic experiments and modern experimental technique." In: *Soviet Physics Uspekhi* 17.5 (1975), pp. 644–650. DOI: [10.1070/pu1975v017n05abeh004362](https://doi.org/10.1070/pu1975v017n05abeh004362). URL: <https://doi.org/10.1070/pu1975v017n05abeh004362>.
- [14] Carlton M. Caves. "Quantum-mechanical noise in an interferometer." In: *Phys. Rev. D* 23 (8 1981), pp. 1693–1708. DOI: [10.1103/PhysRevD.23.1693](https://doi.org/10.1103/PhysRevD.23.1693). URL: <http://link.aps.org/doi/10.1103/PhysRevD.23.1693>.
- [15] Min Xiao, Ling-An Wu, and H. J. Kimble. "Precision measurement beyond the shot-noise limit." In: *Phys. Rev. Lett.* 59 (3 1987), pp. 278–281. DOI: [10.1103/PhysRevLett.59.278](https://doi.org/10.1103/PhysRevLett.59.278). URL: <https://link.aps.org/doi/10.1103/PhysRevLett.59.278>.
- [16] P. Grangier, R. E. Slusher, B. Yurke, and A. LaPorta. "Squeezed-light-enhanced polarization interferometer." In: *Phys. Rev. Lett.* 59 (19 1987), pp. 2153–2156. DOI: [10.1103/PhysRevLett.59.2153](https://doi.org/10.1103/PhysRevLett.59.2153). URL: <https://link.aps.org/doi/10.1103/PhysRevLett.59.2153>.
- [17] The LIGO Scientific Collaboration. "A gravitational wave observatory operating beyond the quantum shot-noise limit." In: *Nature Phys.* 7 (2011), pp. 962–965. DOI: [10.1038/nphys2083](https://doi.org/10.1038/nphys2083).
- [18] Luca Pezzé and Augusto Smerzi. "Entanglement, Nonlinear Dynamics, and the Heisenberg Limit." In: *Phys. Rev. Lett.* 102 (10 2009), p. 100401. DOI: [10.1103/PhysRevLett.102.100401](https://doi.org/10.1103/PhysRevLett.102.100401). URL: <https://link.aps.org/doi/10.1103/PhysRevLett.102.100401>.
- [19] D. J. Wineland, J. J. Bollinger, W. M. Itano, F. L. Moore, and D. J. Heinzen. "Spin squeezing and reduced quantum noise in spectroscopy." In: *Phys. Rev. A* 46.11 (1992), R6797–R6800. DOI: [10.1103/PhysRevA.46.R6797](https://doi.org/10.1103/PhysRevA.46.R6797).

- [20] Masahiro Kitagawa and Masahito Ueda. “Squeezed spin states.” In: *Phys. Rev. A* 47 (6 1993), pp. 5138–5143. DOI: [10.1103/PhysRevA.47.5138](https://doi.org/10.1103/PhysRevA.47.5138). URL: <http://link.aps.org/doi/10.1103/PhysRevA.47.5138>.
- [21] J. Estève, C. Gross, A. Weller, S. Giovanazzi, and M. K. Oberthaler. “Squeezing and entanglement in a Bose-Einstein condensate.” In: *Nature* 455.7217 (Oct. 2008), pp. 1216–1219. ISSN: 0028-0836. DOI: [10.1038/nature07332](https://doi.org/10.1038/nature07332).
- [22] J. Appel, P. J. Windpassinger, D. Oblak, U. B. Hoff, N. Kærgaard, and E. S. Polzik. “Mesoscopic atomic entanglement for precision measurements beyond the standard quantum limit.” In: *Proc. Natl. Acad. Sci. U. S. A.* 106.27 (2009), p. 10960. DOI: [10.1073/pnas.0901550106](https://doi.org/10.1073/pnas.0901550106).
- [23] C. Gross, T. Zibold, E. Nicklas, J. Estève, and M. K. Oberthaler. “Nonlinear atom interferometer surpasses classical precision limit.” In: *Nature* 464.7292 (Apr. 2010), p. 1165. ISSN: 0028-0836. DOI: [10.1038/nature08919](https://doi.org/10.1038/nature08919).
- [24] Ian D. Leroux, Monika H. Schleier-Smith, and Vladan Vuletić. “Orientation-Dependent Entanglement Lifetime in a Squeezed Atomic Clock.” In: *Phys. Rev. Lett.* 104 (25 2010), p. 250801. DOI: [10.1103/PhysRevLett.104.250801](https://doi.org/10.1103/PhysRevLett.104.250801). URL: <https://link.aps.org/doi/10.1103/PhysRevLett.104.250801>.
- [25] Luca Pezzè, Augusto Smerzi, Markus K. Oberthaler, Roman Schmied, and Philipp Treutlein. “Quantum metrology with nonclassical states of atomic ensembles.” In: *Rev. Mod. Phys.* 90 (3 2018), p. 035005. DOI: [10.1103/RevModPhys.90.035005](https://doi.org/10.1103/RevModPhys.90.035005). URL: <https://link.aps.org/doi/10.1103/RevModPhys.90.035005>.
- [26] Caspar F. Ockeloen, Roman Schmied, Max F. Riedel, and Philipp Treutlein. “Quantum Metrology with a Scanning Probe Atom Interferometer.” In: *Phys. Rev. Lett.* 111 (14 2013), p. 143001. DOI: [10.1103/PhysRevLett.111.143001](https://doi.org/10.1103/PhysRevLett.111.143001). URL: <http://link.aps.org/doi/10.1103/PhysRevLett.111.143001>.
- [27] I. Kruse et al. “Improvement of an Atomic Clock using Squeezed Vacuum.” In: *Phys. Rev. Lett.* 117 (14 2016), p. 143004. DOI: [10.1103/PhysRevLett.117.143004](https://doi.org/10.1103/PhysRevLett.117.143004). URL: <http://link.aps.org/doi/10.1103/PhysRevLett.117.143004>.
- [28] Edwin Pedrozo-Peñafiel et al. “Entanglement on an optical atomic-clock transition.” In: *Nature* 588.7838 (2020), pp. 414–418. ISSN: 1476-4687. DOI: [10.1038/s41586-020-3006-1](https://doi.org/10.1038/s41586-020-3006-1). URL: <https://doi.org/10.1038/s41586-020-3006-1>.
- [29] David W. Keith, Christopher R. Ekstrom, Quentin A. Turchette, and David E. Pritchard. “An interferometer for atoms.” In: *Phys. Rev. Lett.* 66 (21 1991), pp. 2693–2696. DOI: [10.1103/PhysRevLett.66.2693](https://doi.org/10.1103/PhysRevLett.66.2693).

- PhysRevLett.66.2693. URL: <https://link.aps.org/doi/10.1103/PhysRevLett.66.2693>.
- [30] O. Carnal and J. Mlynek. “Young’s double-slit experiment with atoms: A simple atom interferometer.” In: *Phys. Rev. Lett.* 66 (21 1991), pp. 2689–2692. DOI: [10.1103/PhysRevLett.66.2689](https://doi.org/10.1103/PhysRevLett.66.2689). URL: <https://link.aps.org/doi/10.1103/PhysRevLett.66.2689>.
- [31] Ernst M Rasel, Markus K Oberthaler, Herman Batelaan, Jörg Schmiedmayer, and Anton Zeilinger. “Atom wave interferometry with diffraction gratings of light.” In: *Phys. Rev. Lett.* 75.14 (1995), p. 2633. DOI: [10.1103/physrevlett.75.2633](https://doi.org/10.1103/physrevlett.75.2633).
- [32] F. Riehle, Th. Kisters, A. Witte, J. Helmcke, and Ch. J. Bordé. “Optical Ramsey spectroscopy in a rotating frame: Sagnac effect in a matter-wave interferometer.” In: *Phys. Rev. Lett.* 67 (2 1991), pp. 177–180. DOI: [10.1103/PhysRevLett.67.177](https://doi.org/10.1103/PhysRevLett.67.177). URL: <https://link.aps.org/doi/10.1103/PhysRevLett.67.177>.
- [33] Mark Kasevich and Steven Chu. “Atomic interferometry using stimulated Raman transitions.” In: *Phys. Rev. Lett.* 67 (2 1991), pp. 181–184. DOI: [10.1103/PhysRevLett.67.181](https://doi.org/10.1103/PhysRevLett.67.181).
- [34] B. Canuel et al. “Six-axis inertial sensor using cold-atom interferometry.” In: *Phys. Rev. Lett.* 97.1 (2006), p. 010402. DOI: [10.1103/PhysRevLett.97.010402](https://doi.org/10.1103/PhysRevLett.97.010402).
- [35] T. L. Gustavson, P. Bouyer, and M. A. Kasevich. “Precision Rotation Measurements with an Atom Interferometer Gyroscope.” In: *Phys. Rev. Lett.* 78 (11 1997), pp. 2046–2049. DOI: [10.1103/PhysRevLett.78.2046](https://doi.org/10.1103/PhysRevLett.78.2046). URL: <http://link.aps.org/doi/10.1103/PhysRevLett.78.2046>.
- [36] Achim Peters, Keng Yeow Chung, and Steven Chu. “Measurement of gravitational acceleration by dropping atoms.” In: *Nature* 400.6747 (Aug. 1999), pp. 849–852. ISSN: 0028-0836. DOI: [10.1038/23655](https://doi.org/10.1038/23655).
- [37] Zhong-Kun Hu, Bu-Liang Sun, Xiao-Chun Duan, Min-Kang Zhou, Le-Le Chen, Su Zhan, Qiao-Zhen Zhang, and Jun Luo. “Demonstration of an ultrahigh-sensitivity atom-interferometry absolute gravimeter.” In: *Phys. Rev. A* 88 (4 2013), p. 043610. DOI: [10.1103/PhysRevA.88.043610](https://doi.org/10.1103/PhysRevA.88.043610). URL: <https://link.aps.org/doi/10.1103/PhysRevA.88.043610>.
- [38] M. Snadden, J. McGuirk, P. Bouyer, K. Haritos, and M. Kasevich. “Measurement of the Earth’s Gravity Gradient with an Atom Interferometer-Based Gravity Gradiometer.” In: *Physical Review Letters* 81.5 (1998), pp. 971–974. DOI: [10.1103/physrevlett.81.971](https://doi.org/10.1103/physrevlett.81.971).

- [39] G. Rosi, F. Sorrentino, L. Cacciapuoti, M. Prevedelli, and G. M. Tino. “Precision measurement of the Newtonian gravitational constant using cold atoms.” In: *Nature* 510.7506 (June 2014), pp. 518–521. ISSN: 0028-0836. DOI: [10.1038/nature13433](https://doi.org/10.1038/nature13433). URL: <http://www.nature.com/nature/journal/v510/n7506/abs/nature13433.html>.
- [40] Stuart S. Szigeti, Onur Hosten, and Simon A. Haine. “Improving cold-atom sensors with quantum entanglement: Prospects and challenges.” In: *Applied Physics Letters* 118.14 (2021), p. 140501. DOI: [10.1063/5.0050235](https://doi.org/10.1063/5.0050235). eprint: <https://doi.org/10.1063/5.0050235>. URL: <https://doi.org/10.1063/5.0050235>.
- [41] Robert Bucker, Julian Grond, Stephanie Manz, Tarik Berrada, Thomas Betz, Christian Koller, Ulrich Hohenester, Thorsten Schumm, Aurelien Perrin, and Jorg Schmiedmayer. “Twin-atom beams.” In: *Nature Phys.* 7.8 (Aug. 2011), pp. 608–611. ISSN: 1745-2473. DOI: [10.1038/nphys1992](https://doi.org/10.1038/nphys1992).
- [42] K. V. Kheruntsyan, J.-C. Jaskula, P. Deuar, M. Bonneau, G. B. Partridge, J. Ruauadel, R. Lopes, D. Boiron, and C. I. Westbrook. “Violation of the Cauchy-Schwarz Inequality with Matter Waves.” In: *Phys. Rev. Lett.* 108.26 (2012), p. 260401. DOI: [10.1103/PhysRevLett.108.260401](https://doi.org/10.1103/PhysRevLett.108.260401). URL: <http://link.aps.org/doi/10.1103/PhysRevLett.108.260401> (visited on 03/06/2013).
- [43] J.-C. Jaskula, M. Bonneau, G. B. Partridge, V. Krachmalnicoff, P. Deuar, K. V. Kheruntsyan, A. Aspect, D. Boiron, and C. I. Westbrook. “Sub-Poissonian Number Differences in Four-Wave Mixing of Matter Waves.” In: *Phys. Rev. Lett.* 105.19 (Nov. 2010), p. 190402. DOI: [10.1103/PhysRevLett.105.190402](https://doi.org/10.1103/PhysRevLett.105.190402). URL: <http://link.aps.org/doi/10.1103/PhysRevLett.105.190402> (visited on 03/04/2013).
- [44] A Perrin, H Chang, V Krachmalnicoff, M Schellekens, D Boiron, A Aspect, and C I Westbrook. “Observation of Atom Pairs in Spontaneous Four-Wave Mixing of Two Colliding Bose-Einstein Condensates.” In: *Phys. Rev. Lett.* 99.15 (Oct. 2007), p. 150405. DOI: [10.1103/PhysRevLett.99.150405](https://doi.org/10.1103/PhysRevLett.99.150405).
- [45] D. K. Shin, B. M. Henson, S. S. Hodgman, T. Wasak, J. Chwedeńczuk, and A. G. Truscott. “Bell correlations between spatially separated pairs of atoms.” In: *Nature Communications* 10.1 (2019), p. 4447. ISSN: 2041-1723. DOI: [10.1038/s41467-019-12192-8](https://doi.org/10.1038/s41467-019-12192-8). URL: <https://doi.org/10.1038/s41467-019-12192-8>.
- [46] R. I. Khakimov, B. M. Henson, D. K. Shin, S. S. Hodgman, R. G. Dall, K. G. H. Baldwin, and A. G. Truscott. “Ghost imaging with atoms.” In: *Nature* 540.7631 (2016), pp. 100–103. ISSN: 1476-4687. DOI: [10.1038/nature20154](https://doi.org/10.1038/nature20154). URL: <https://doi.org/10.1038/nature20154>.

- [47] F. Anders et al. "Momentum Entanglement for Atom Interferometry." In: *Phys. Rev. Lett.* 127 (14 2021), p. 140402. DOI: [10.1103/PhysRevLett.127.140402](https://doi.org/10.1103/PhysRevLett.127.140402). URL: <https://link.aps.org/doi/10.1103/PhysRevLett.127.140402>.
- [48] Graham P. Greve, Chengyi Luo, Baochen Wu, and James K. Thompson. *Entanglement-Enhanced Matter-Wave Interferometry in a High-Finesse Cavity*. 2021. DOI: [10.48550/ARXIV.2110.14027](https://doi.org/10.48550/ARXIV.2110.14027). URL: <https://arxiv.org/abs/2110.14027>.
- [49] Luca Pezzè and Augusto Smerzi. "Quantum theory of phase estimation." In: *arXiv:1411.5164v1* (2014).
- [50] Luca Pezzè, Philipp Hyllus, and Augusto Smerzi. "Phase-sensitivity bounds for two-mode interferometers." In: *Phys. Rev. A* 91 (3 2015), p. 032103. DOI: [10.1103/PhysRevA.91.032103](https://doi.org/10.1103/PhysRevA.91.032103). URL: <http://link.aps.org/doi/10.1103/PhysRevA.91.032103>.
- [51] Yi-Quan Zou, Ling-Na Wu, Qi Liu, Xin-Yu Luo, Shuai-Feng Guo, Jia-Hao Cao, Meng Khoon Tey, and Li You. "Beating the Classical Precision Limit with Spin-1 Dicke States of More than 10,000 Atoms." In: *Proc. Natl. Acad. Sci. U.S.A.* 115.25 (June 2018), pp. 6381–6385. ISSN: 0027-8424, 1091-6490. DOI: [10.1073/pnas.1715105115](https://doi.org/10.1073/pnas.1715105115).
- [52] P. Hyllus, W. Laskowski, R. Krischek, C. Schwemmer, W. Wieczorek, H. Weinfurter, L. Pezzè, and A. Smerzi. "Fisher information and multiparticle entanglement." In: *Phys. Rev. A* 85 (2 2012), p. 022321. DOI: [10.1103/PhysRevA.85.022321](https://doi.org/10.1103/PhysRevA.85.022321). URL: <http://link.aps.org/doi/10.1103/PhysRevA.85.022321>.
- [53] Bernd Lücke, Jan Peise, Giuseppe Vitagliano, Jan Arlt, Luis Santos, Géza Tóth, and Carsten Klempt. "Detecting multiparticle entanglement of Dicke States." In: *Phys. Rev. Lett.* 112 (15 2014), p. 155304. DOI: [10.1103/PhysRevLett.112.155304](https://doi.org/10.1103/PhysRevLett.112.155304). URL: <http://link.aps.org/doi/10.1103/PhysRevLett.112.155304>.
- [54] Bernd Lücke. "Multi-particle entanglement in a spinor Bose-Einstein condensate for quantum-enhanced interferometry." PhD thesis. Technische Informationsbibliothek und Universitätsbibliothek Hannover, 2014.
- [55] Giuseppe Vitagliano, Iagoba Apellaniz, Iñigo L. Egusquiza, and Géza Tóth. "Spin squeezing and entanglement for an arbitrary spin." In: *Phys. Rev. A* 89 (3 2014), p. 032307. DOI: [10.1103/PhysRevA.89.032307](https://doi.org/10.1103/PhysRevA.89.032307). URL: <http://link.aps.org/doi/10.1103/PhysRevA.89.032307>.
- [56] M. Riedel, P. Böhi, Y. Li, T. Hänsch, A. Sinatra, and P. Treutlein. "Atom-chip-based generation of entanglement for quantum metrology." In: *Nature* 464.7292 (Apr. 2010), p. 1170. ISSN: 0028-0836. DOI: [10.1038/nature08988](https://doi.org/10.1038/nature08988).



- [57] W. Muessel, H. Strobel, D. Linnemann, T. Zibold, B. Juliá-Díaz, and M. K. Oberthaler. “Twist-and-turn spin squeezing in Bose-Einstein condensates.” In: *Phys. Rev. A* 92 (2 2015), p. 023603. DOI: [10.1103/PhysRevA.92.023603](https://doi.org/10.1103/PhysRevA.92.023603).
- [58] W. Muessel, H. Strobel, D. Linnemann, D. B. Hume, and M. K. Oberthaler. “Scalable Spin Squeezing for Quantum-Enhanced Magnetometry with Bose-Einstein Condensates.” In: *Phys. Rev. Lett.* 113 (10 2014), p. 103004. DOI: [10.1103/PhysRevLett.113.103004](https://doi.org/10.1103/PhysRevLett.113.103004). URL: <http://link.aps.org/doi/10.1103/PhysRevLett.113.103004>.
- [59] Helmut Strobel, Wolfgang Muessel, Daniel Linnemann, Tilman Zibold, David B. Hume, Luca Pezzè, Augusto Smerzi, and Markus K. Oberthaler. “Fisher information and entanglement of non-Gaussian spin states.” In: *Science* 345.6195 (2014), pp. 424–427. ISSN: 0036-8075. DOI: [10.1126/science.1250147](https://doi.org/10.1126/science.1250147). URL: <https://science.sciencemag.org/content/345/6195/424>.
- [60] C. Gross, H. Strobel, E. Nicklas, T. Zibold, N. Bar-Gill, G. Kurizki, and M. K. Oberthaler. “Atomic homodyne detection of continuous-variable entangled twin-atom states.” In: *Nature* 480 (Nov. 2011), p. 219. ISSN: 1476-4687. DOI: [10.1038/nature10654](https://doi.org/10.1038/nature10654).
- [61] C. D. Hamley, C. S. Gerving, T. M. Hoang, E. M. Bookjans, and M. S. Chapman. “Spin-nematic squeezed vacuum in a quantum gas.” In: *Nature Phys.* 8 (Feb. 2012), p. 305. ISSN: 1745-2481. DOI: [10.1038/nphys2245](https://doi.org/10.1038/nphys2245).
- [62] J. Peise et al. “Satisfying the Einstein-Podolsky-Rosen criterion with massive particles.” In: *Nat. Commun.* 6 (2015), p. 8984. DOI: [10.1038/ncomms9984](https://doi.org/10.1038/ncomms9984).
- [63] B. Lücke et al. “Twin matter waves for interferometry beyond the classical limit.” In: *Science* 334.6057 (Nov. 2011), pp. 773–776. ISSN: 0036-8075, 1095-9203. DOI: [10.1126/science.1208798](https://doi.org/10.1126/science.1208798). URL: <http://www.sciencemag.org/content/334/6057/773> (visited on 03/06/2013).
- [64] Xin-Yu Luo, Yi-Quan Zou, Ling-Na Wu, Qi Liu, Ming-Fei Han, Meng Khoon Tey, and Li You. “Deterministic entanglement generation from driving through quantum phase transitions.” In: *Science* 355.6325 (2017), pp. 620–623. ISSN: 0036-8075. DOI: [10.1126/science.aag1106](https://doi.org/10.1126/science.aag1106).
- [65] J. Hald, J. L. Sørensen, C. Schori, and E. S. Polzik. “Spin squeezed atoms: A macroscopic entangled ensemble created by light.” In: *Phys. Rev. Lett.* 83.7 (1999), p. 1319. DOI: [10.1103/PhysRevLett.83.1319](https://doi.org/10.1103/PhysRevLett.83.1319).

- [66] Ian D. Leroux, Monika H. Schleier-Smith, and Vladan Vuletić. “Implementation of cavity squeezing of a collective atomic spin.” In: *Phys. Rev. Lett.* 104.7 (2010), p. 073602. DOI: [10.1103/PhysRevLett.104.073602](https://doi.org/10.1103/PhysRevLett.104.073602).
- [67] M. H. Schleier-Smith, I. D. Leroux, and V. Vuletić. “States of an ensemble of two-level atoms with reduced quantum uncertainty.” In: *Phys. Rev. Lett.* 104 (7 2010), p. 073604. DOI: [10.1103/PhysRevLett.104.073604](https://doi.org/10.1103/PhysRevLett.104.073604). URL: <http://link.aps.org/doi/10.1103/PhysRevLett.104.073604>.
- [68] Z. Chen, J. Bohnet, S. Sankar, J. Dai, and J. Thompson. “Conditional spin squeezing of a large ensemble via the vacuum Rabi splitting.” In: *Phys. Rev. Lett.* 106.13 (2011), p. 133601. DOI: [10.1103/PhysRevLett.106.133601](https://doi.org/10.1103/PhysRevLett.106.133601).
- [69] R. J. Sewell, M. Koschorreck, M. Napolitano, B. Dubost, N. Behbood, and M. W. Mitchell. “Magnetic Sensitivity Beyond the Projection Noise Limit by Spin Squeezing.” In: *Phys. Rev. Lett.* 109 (25 2012), p. 253605. DOI: [10.1103/PhysRevLett.109.253605](https://doi.org/10.1103/PhysRevLett.109.253605).
- [70] Théo Laudat, Vincent Dugrain, Tommaso Mazzone, Meng-Zi Huang, Carlos L Garrido Alzar, Alice Sinatra, Peter Rosenbusch, and Jakob Reichel. “Spontaneous Spin Squeezing in a Rubidium BEC.” In: *New J. Phys.* 20.7 (July 2018), p. 073018. ISSN: 1367-2630. DOI: [10.1088/1367-2630/aac1e](https://doi.org/10.1088/1367-2630/aac1e).
- [71] Boris Braverman et al. “Near-Unitary Spin Squeezing in  $^{171}\text{Yb}$ .” In: *Phys. Rev. Lett.* 122 (22 2019), p. 223203. DOI: [10.1103/PhysRevLett.122.223203](https://doi.org/10.1103/PhysRevLett.122.223203). URL: <https://link.aps.org/doi/10.1103/PhysRevLett.122.223203>.
- [72] Onur Hosten, Nils J. Engelsen, Rajiv Krishnakumar, and Mark A. Kasevich. “Measurement noise 100 times lower than the quantum-projection limit using entangled atoms.” In: *Nature* 529 (2016), p. 505. DOI: [10.1038/nature16176](https://doi.org/10.1038/nature16176).
- [73] Anne Louchet-Chauvet, Jürgen Appel, Jelmer J Renema, Daniel Oblak, Niels Kjaergaard, and Eugene S Polzik. “Entanglement-assisted atomic clock beyond the projection noise limit.” In: *New J. Phys.* 12.6 (2010), p. 065032. DOI: [10.1088/1367-2630/12/6/065032](https://doi.org/10.1088/1367-2630/12/6/065032). URL: <http://iopscience.iop.org/article/10.1088/1367-2630/13/6/065025/meta>.
- [74] Karsten Lange, Jan Peise, Bernd Lücke, Ilka Kruse, Giuseppe Vitagliano, Iagoba Apellaniz, Matthias Kleinmann, Géza Tóth, and Carsten Klempt. “Entanglement between two spatially separated atomic modes.” In: *Science* 360.6387 (2018), pp. 416–418. DOI: [10.1126/science.aao2035](https://doi.org/10.1126/science.aao2035). URL: <http://science.sciencemag.org/content/360/6387/416>.

- [75] Matteo Fadel, Tilman Zibold, Boris Décamps, and Philipp Treutlein. “Spatial entanglement patterns and Einstein-Podolsky-Rosen steering in Bose-Einstein condensates.” In: *Science* 360.6387 (2018), pp. 409–413. ISSN: 0036-8075. DOI: [10.1126/science.aao1850](https://doi.org/10.1126/science.aao1850). URL: <http://science.sciencemag.org/content/360/6387/409>.
- [76] Philipp Kunkel, Maximilian Prüfer, Helmut Strobel, Daniel Linnemann, Anika Frölian, Thomas Gasenzer, Martin Gärtner, and Markus K. Oberthaler. “Spatially distributed multipartite entanglement enables EPR steering of atomic clouds.” In: *Science* 360.6387 (2018), pp. 413–416. ISSN: 0036-8075. DOI: [10.1126/science.aao2254](https://doi.org/10.1126/science.aao2254). URL: <http://science.sciencemag.org/content/360/6387/413>.
- [77] T. Berrada, S. van Frank, R. Bücker, T. Schumm, J.-F. Schaff, and J Schmiedmayer. “Integrated Mach-Zehnder interferometer for Bose-Einstein condensates.” In: *Nat. Commun.* 4 (June 2013), pp. –. DOI: [10.1038/ncomms3077](https://doi.org/10.1038/ncomms3077).
- [78] D K Shin, J A Ross, B M Henson, S S Hodgman, and A G Truscott. “Entanglement-based 3D magnetic gradiometry with an ultracold atomic scattering halo.” In: *New Journal of Physics* 22.1 (2020), p. 013002. DOI: [10.1088/1367-2630/ab66de](https://doi.org/10.1088/1367-2630/ab66de). URL: <https://doi.org/10.1088/1367-2630/ab66de>.
- [79] Benjamin K. Malia, Julián Martínez-Rincón, Yunfan Wu, Onur Hosten, and Mark A. Kasevich. “Free Space Ramsey Spectroscopy in Rubidium with Noise below the Quantum Projection Limit.” In: *Phys. Rev. Lett.* 125 (4 2020), p. 043202. DOI: [10.1103/PhysRevLett.125.043202](https://doi.org/10.1103/PhysRevLett.125.043202). URL: <https://link.aps.org/doi/10.1103/PhysRevLett.125.043202>.
- [80] Leonardo Salvi, Nicola Poli, Vladan Vuletić, and Guglielmo M. Tino. “Squeezing on Momentum States for Atom Interferometry.” In: *Phys. Rev. Lett.* 120.3 (2018), p. 033601. DOI: [10.1103/physrevlett.120.033601](https://doi.org/10.1103/physrevlett.120.033601).
- [81] Remi Geiger and Michael Trupke. “Proposal for a Quantum Test of the Weak Equivalence Principle with Entangled Atomic Species.” In: *Phys. Rev. Lett.* 120 (4 2018), p. 043602. DOI: [10.1103/PhysRevLett.120.043602](https://doi.org/10.1103/PhysRevLett.120.043602). URL: <https://link.aps.org/doi/10.1103/PhysRevLett.120.043602>.
- [82] Athreya Shankar, Leonardo Salvi, Maria Luisa Chiofalo, Nicola Poli, and Murray J Holland. “Squeezed state metrology with Bragg interferometers operating in a cavity.” In: *Quantum Science and Technology* 4.4 (2019), p. 045010. DOI: [10.1088/2058-9565/ab455d](https://doi.org/10.1088/2058-9565/ab455d). URL: <https://doi.org/10.1088/2058-9565/ab455d>.

- [83] Stuart S. Szigeti, Samuel P. Nolan, John D. Close, and Simon A. Haine. “High-Precision Quantum-Enhanced Gravimetry with a Bose-Einstein Condensate.” In: *Phys. Rev. Lett.* 125 (10 2020), p. 100402. DOI: [10.1103/PhysRevLett.125.100402](https://doi.org/10.1103/PhysRevLett.125.100402). URL: <https://link.aps.org/doi/10.1103/PhysRevLett.125.100402>.
- [84] Robin Corgier, Naceur Gaaloul, Augusto Smerzi, and Luca Pezzè. *Delta-kick Squeezing*. 2021. arXiv: [2103.10896](https://arxiv.org/abs/2103.10896) [quant-ph].
- [85] M. Scherer, B. Lücke, G. Gebreyesus, O. Topic, F. Deuretzbacher, W. Ertmer, L. Santos, J. J. Arlt, and C. Klempt. “Spontaneous breaking of spatial and spin symmetry in spinor condensates.” In: *Phys. Rev. Lett.* 105.13 (2010), p. 135302. DOI: [10.1103/PhysRevLett.105.135302](https://doi.org/10.1103/PhysRevLett.105.135302).
- [86] Z. Zhang and L.-M. Duan. “Generation of Massive Entanglement through an Adiabatic Quantum Phase Transition in a Spinor Condensate.” In: *Phys. Rev. Lett.* 111 (18 2013), p. 180401. DOI: [10.1103/PhysRevLett.111.180401](https://doi.org/10.1103/PhysRevLett.111.180401). URL: <http://link.aps.org/doi/10.1103/PhysRevLett.111.180401>.
- [87] P. Feldmann, M. Gessner, M. Gabbrielli, C. Klempt, L. Santos, L. Pezzè, and A. Smerzi. “Interferometric sensitivity and entanglement by scanning through quantum phase transitions in spinor Bose-Einstein condensates.” In: *Phys. Rev. A* 97 (3 2018), p. 032339. DOI: [10.1103/PhysRevA.97.032339](https://doi.org/10.1103/PhysRevA.97.032339). URL: <https://link.aps.org/doi/10.1103/PhysRevA.97.032339>.
- [88] L. Pezzè, M. Gessner, P. Feldmann, C. Klempt, L. Santos, and A. Smerzi. “Heralded Generation of Macroscopic Superposition States in a Spinor Bose-Einstein Condensate.” In: *Phys. Rev. Lett.* 123.26 (2019). DOI: [10.1103/physrevlett.123.260403](https://doi.org/10.1103/physrevlett.123.260403).
- [89] C. Klempt. “Wechselwirkung in Bose-Fermi-Quantengasen.” PhD thesis. Hannover: Leibniz Universität Hannover, 2007.
- [90] Manuel Scherer. “Nichtklassische Zustände in Spinor-Bose-Einstein-Kondensaten.” PhD thesis. Leibniz Universität Hannover, 2012.
- [91] C. Klempt, T. van Zoest, T. Henninger, O. Topic, E. Rasel, W. Ertmer, and J. Arlt. “Ultraviolet light-induced atom desorption for large rubidium and potassium magneto-optical traps.” In: *Phys. Rev. A* 73 (2006), p. 13410. DOI: [10.1103/PhysRevA.73.013410](https://doi.org/10.1103/PhysRevA.73.013410).
- [92] W. Ketterle and N.J Van Druten. “Evaporative cooling of trapped atoms.” In: *Adv. At. Mol. Opt. Phys.* 37 (1996), pp. 181–236.
- [93] Charles S. Adams, Heun Jin Lee, Nir Davidson, Mark Kasevich, and Steven Chu. “Evaporative Cooling in a Crossed Dipole Trap.” In: *Phys. Rev. Lett.* 74 (18 1995), pp. 3577–3580. DOI: [10.1103/PhysRevLett.74.3577](https://doi.org/10.1103/PhysRevLett.74.3577). URL: <http://link.aps.org/doi/10.1103/PhysRevLett.74.3577>.

- [94] Martin Quensen. “Fast Magnetic Field Stabilization Using the Anisotropic Magnetoresistive Effect.” MA thesis. Leibniz Universität Hannover, 2020.
- [95] Fabrice Gerbier, Artur Widera, Simon Fölling, Olaf Mandel, and Immanuel Bloch. “Resonant control of spin dynamics in ultracold quantum gases by microwave dressing.” In: *Phys. Rev. A* 73.4, 041602 (2006), p. 041602. DOI: [10.1103/PhysRevA.73.041602](https://doi.org/10.1103/PhysRevA.73.041602). URL: <http://link.aps.org/abstract/PRA/v73/e041602>.
- [96] Matthew J. Buguslawski. “All-microwave control of hyperfine states in ultracold Spin-1 rubidium.” PhD thesis. Georgia Institute of Technology, 2019. URL: <https://smartech.gatech.edu/handle/1853/62298>.
- [97] Philipp Kunkel, Maximilian Prüfer, Stefan Lannig, Rodrigo Rosa-Medina, Alexis Bonnin, Martin Gärttner, Helmut Strobel, and Markus K. Oberthaler. “Simultaneous Readout of Non-commuting Collective Spin Observables beyond the Standard Quantum Limit.” In: *Phys. Rev. Lett.* 123 (6 2019), p. 063603. DOI: [10.1103/PhysRevLett.123.063603](https://doi.org/10.1103/PhysRevLett.123.063603). URL: <https://link.aps.org/doi/10.1103/PhysRevLett.123.063603>.
- [98] Polina Feldmann. “Generalized quantum phase transitions for quantum-state engineering in spinor bose-einstein condensates.” PhD thesis. Gottfried Wilhelm Leibniz Universität, 2021. URL: <https://www.repo.uni-hannover.de/handle/123456789/10850>.
- [99] C. C. Gerry and P.L. Knight. *Introductory quantum optics*. Cambridge University Press, 2005.
- [100] Yuki Kawaguchi and Masahito Ueda. “Spinor Bose-Einstein condensates.” In: *Phys. Rep.* 520.5 (2012), pp. 253–381. ISSN: 0370-1573. DOI: <http://dx.doi.org/10.1016/j.physrep.2012.07.005>. URL: <http://www.sciencedirect.com/science/article/pii/S0370157312002098>.
- [101] C. K. Law, H. Pu, and N. P. Bigelow. “Quantum Spins Mixing in Spinor Bose-Einstein Condensates.” In: *Phys. Rev. Lett.* 81.24 (1998), pp. 5257–5261. DOI: [10.1103/PhysRevLett.81.5257](https://doi.org/10.1103/PhysRevLett.81.5257).
- [102] D. Stamper-Kurn and M. Ueda. “Spinor Bose gases: Symmetries, magnetism, and quantum dynamics.” In: *Rev. Mod. Phys.* 85 (3 2013), p. 1191. DOI: [10.1103/RevModPhys.85.1191](https://doi.org/10.1103/RevModPhys.85.1191). URL: <http://link.aps.org/doi/10.1103/RevModPhys.85.1191>.
- [103] C. S. Gerving, T. M. Hoang, B. J. Land, M. Anquez, C. D. Hamley, and M. S. Chapman. “Non-equilibrium dynamics of an unstable quantum pendulum explored in a spin-1 Bose-Einstein condensate.” In: *Nat. Commun.* 3 (Nov. 2012), p. 1169. DOI: [10.1038/ncomms2179](https://doi.org/10.1038/ncomms2179). URL: <http://www.nature.com/>

- [ncomms/journal/v3/n10/full/ncomms2179.html](https://ncomms.com/journal/v3/n10/full/ncomms2179.html) (visited on 02/23/2016).
- [104] Q. Guan, G. W. Biedermann, A. Schwettmann, and R. J. Lewis-Swan. “Tailored generation of quantum states in an entangled spinor interferometer to overcome detection noise.” In: *Phys. Rev. A* 104 (4 2021), p. 042415. DOI: [10.1103/PhysRevA.104.042415](https://doi.org/10.1103/PhysRevA.104.042415). URL: <https://link.aps.org/doi/10.1103/PhysRevA.104.042415>.
- [105] Fabian Anders, Luca Pezzè, Augusto Smerzi, and Carsten Klempt. “Phase magnification by two-axis countertwisting for detection-noise robust interferometry.” In: *Phys. Rev. A* 97 (4 2018), p. 043813. DOI: [10.1103/PhysRevA.97.043813](https://doi.org/10.1103/PhysRevA.97.043813). URL: <https://link.aps.org/doi/10.1103/PhysRevA.97.043813>.
- [106] Stuart S. Szigeti, Robert J. Lewis-Swan, and Simon A. Haine. “Pumped-Up  $SU(1,1)$  Interferometry.” In: *Phys. Rev. Lett.* 118 (15 2017), p. 150401. DOI: [10.1103/PhysRevLett.118.150401](https://doi.org/10.1103/PhysRevLett.118.150401). URL: <https://link.aps.org/doi/10.1103/PhysRevLett.118.150401>.
- [107] D. Linnemann, H. Strobel, W. Muessel, J. Schulz, R. J. Lewis-Swan, K. V. Kheruntsyan, and M. K. Oberthaler. “Quantum-enhanced sensing based on time reversal of non-linear dynamics.” In: *arXiv:1602.07505* (2016).
- [108] Marco Gabbrielli, Luca Pezzè, and Augusto Smerzi. “Spin-Mixing Interferometry with Bose-Einstein Condensates.” In: *Phys. Rev. Lett.* 115 (16 2015), p. 163002. DOI: [10.1103/PhysRevLett.115.163002](https://doi.org/10.1103/PhysRevLett.115.163002). URL: <http://link.aps.org/doi/10.1103/PhysRevLett.115.163002>.
- [109] Qi Liu, Ling-Na Wu, Jia-Hao Cao, Tian-Wei Mao, Xin-Wei Li, Shuai-Feng Guo, Meng Khoon Tey, and Li You. “Nonlinear interferometry beyond classical limit enabled by cyclic dynamics.” In: *Nature Physics* 18.2 (2022), pp. 167–171. ISSN: 1745-2481. DOI: [10.1038/s41567-021-01441-7](https://doi.org/10.1038/s41567-021-01441-7). URL: <https://doi.org/10.1038/s41567-021-01441-7>.
- [110] Thai M. Hoang, Hebbe M. Bharath, Matthew J. Boguslawski, Martin Anquez, Bryce A. Robbins, and Michael S. Chapman. “Adiabatic Quenches and Characterization of Amplitude Excitations in a Continuous Quantum Phase Transition.” In: *Proc. Natl. Acad. Sci. U.S.A.* 113.34 (Aug. 2016), pp. 9475–9479. ISSN: 0027-8424, 1091-6490. DOI: [10.1073/pnas.1600267113](https://doi.org/10.1073/pnas.1600267113).
- [111] Shuai-Feng Guo, Feng Chen, Qi Liu, Ming Xue, Jun-Jie Chen, Jia-Hao Cao, Tian-Wei Mao, Meng Khoon Tey, and Li You. “Faster State Preparation across Quantum Phase Transition Assisted by Reinforcement Learning.” In: *Phys. Rev. Lett.* 126 (6 2021), p. 060401. DOI: [10.1103/PhysRevLett.126.060401](https://doi.org/10.1103/PhysRevLett.126.060401).



- URL: <https://link.aps.org/doi/10.1103/PhysRevLett.126.060401>.
- [112] Lin Xin, M.S. Chapman, and T.A.B. Kennedy. “Fast Generation of Time-Stationary Spin-1 Squeezed States by Nonadiabatic Control.” In: *PRX Quantum* 3 (1 2022), p. 010328. DOI: [10.1103/PRXQuantum.3.010328](https://doi.org/10.1103/PRXQuantum.3.010328). URL: <https://link.aps.org/doi/10.1103/PRXQuantum.3.010328>.
- [113] Lin Xin, Maryrose Barrios, Julia T. Cohen, and Michael S. Chapman. “Squeezed Ground States in a Spin-1 Bose-Einstein Condensate.” In: *arXiv:2202.12338 [physics]* (Feb. 2022). arXiv: [2202.12338](https://arxiv.org/abs/2202.12338).
- [114] D.J. Griffiths and E.G. Harris. *Introduction to quantum mechanics*. Vol. 118. Prentice Hall, 1995.
- [115] Patrick Cheinet. “Conception et réalisation d’un gravimètre à atomes froids.” PhD thesis. Université Pierre et Marie Curie - Paris VI, 2006.
- [116] Michael Gilowski. “Quantitative Analyse der Auflösungsbe-  
grenzung eines atomaren Gyroskops.” PhD thesis. Leibniz  
Universität Hannover, 2010.
- [117] Peter Berg. “Analyse und Unterdrückung von Phasenrauschen  
in der Atominterferometrie.” MA thesis. Leibniz Universität  
Hannover, 2009.
- [118] Christophe Cassens. “Ein Raman-Lasersystem für Atominter-  
ferometrie mit verschränkten Ensembles.” MA thesis. Leibniz  
Universität Hannover, 2022.
- [119] C. Di Fidio and W. Vogel. “Damped Rabi oscillations of a  
cold trapped ion.” In: *Phys. Rev. A* 62 (3 2000), p. 031802. DOI:  
[10.1103/PhysRevA.62.031802](https://doi.org/10.1103/PhysRevA.62.031802). URL: [https://link.aps.org/  
doi/10.1103/PhysRevA.62.031802](https://link.aps.org/doi/10.1103/PhysRevA.62.031802).
- [120] S. Abend et al. “Atom-chip fountain gravimeter.” In: *Phys. Rev.  
Lett.* 117.20 (2016), p. 203003. DOI: [10.1103/physrevlett.117.  
203003](https://doi.org/10.1103/physrevlett.117.203003).
- [121] Hubert Ammann and Nelson Christensen. “Delta Kick Cooling:  
A new method for cooling atoms.” In: *Phys. Rev. Lett.* 78 (11  
1997), pp. 2088–2091. DOI: [10.1103/PhysRevLett.78.2088](https://doi.org/10.1103/PhysRevLett.78.2088). URL:  
<http://link.aps.org/doi/10.1103/PhysRevLett.78.2088>.
- [122] David L. Butts, Krish Kotru, Joseph M. Kinast, Antonije M.  
Radojevic, Brian P. Timmons, and Richard E. Stoner. “Efficient  
broadband Raman pulses for large-area atom interferometry.”  
In: *J. Opt. Soc. Am. B* 30.4 (2013), pp. 922–927. DOI: [10.1364/  
JOSAB.30.000922](https://doi.org/10.1364/JOSAB.30.000922). URL: [http://josab.osa.org/abstract.  
cfm?URI=josab-30-4-922](http://josab.osa.org/abstract.cfm?URI=josab-30-4-922).

- [123] Krish Kotru, David L. Butts, Joseph M. Kinast, and Richard E. Stoner. “Large-Area Atom Interferometry with Frequency-Swept Raman Adiabatic Passage.” In: *Phys. Rev. Lett.* 115 (10 2015), p. 103001. DOI: [10.1103/PhysRevLett.115.103001](https://doi.org/10.1103/PhysRevLett.115.103001). URL: <https://link.aps.org/doi/10.1103/PhysRevLett.115.103001>.
- [124] Matt Jaffe, Victoria Xu, Philipp Haslinger, Holger Müller, and Paul Hamilton. “Efficient Adiabatic Spin-Dependent Kicks in an Atom Interferometer.” In: *Phys. Rev. Lett.* 121 (4 2018), p. 040402. DOI: [10.1103/PhysRevLett.121.040402](https://doi.org/10.1103/PhysRevLett.121.040402). URL: <https://link.aps.org/doi/10.1103/PhysRevLett.121.040402>.
- [125] Víctor M. Pérez-García, H. Michinel, J. I. Cirac, M. Lewenstein, and P. Zoller. “Low Energy Excitations of a Bose-Einstein Condensate: A Time-Dependent Variational Analysis.” In: *Phys. Rev. Lett.* 77 (27 1996), pp. 5320–5323. DOI: [10.1103/PhysRevLett.77.5320](https://doi.org/10.1103/PhysRevLett.77.5320). URL: <https://link.aps.org/doi/10.1103/PhysRevLett.77.5320>.
- [126] Matthew J. Boguslawski. “All-microwave control of hyperfine states in ultracold spin-1 rubidium.” PhD thesis. Georgia Institute of Technology, 2019.
- [127] Bernd Meyer, Alexander Idel, Fabian Anders, Jan Peise, and Carsten Klempt. *Dynamical low-noise microwave source for cold atom experiments*. 2020. DOI: [10.48550/ARXIV.2003.10989](https://doi.org/10.48550/ARXIV.2003.10989). URL: <https://arxiv.org/abs/2003.10989>.
- [128] Savas Dimopoulos, Peter W. Graham, Jason M. Hogan, Mark A. Kasevich, and Surjeet Rajendran. “Atomic gravitational wave interferometric sensor.” In: *Phys. Rev. D* 78.12 (2008), p. 122002. DOI: [10.1103/PhysRevD.78.122002](https://doi.org/10.1103/PhysRevD.78.122002).
- [129] S Loriani et al. “Atomic source selection in space-borne gravitational wave detection.” In: *New Journal of Physics* 21.6 (2019), p. 063030. DOI: [10.1088/1367-2630/ab22d0](https://doi.org/10.1088/1367-2630/ab22d0). URL: <https://doi.org/10.1088/1367-2630/ab22d0>.
- [130] Björn Schrinski, Klaus Hornberger, and Stefan Nimmrichter. “How to rule out collapse models with BEC interferometry.” In: *arXiv:2008.13580* (2020).
- [131] B. P. Lanyon, M. Zwerger, P. Jurcevic, C. Hempel, W. Dür, H. J. Briegel, R. Blatt, and C. F. Roos. “Experimental Violation of Multipartite Bell Inequalities with Trapped Ions.” In: *Phys. Rev. Lett.* 112 (10 2014), p. 100403. DOI: [10.1103/PhysRevLett.112.100403](https://doi.org/10.1103/PhysRevLett.112.100403).
- [132] Wenjamin Rosenfeld, Daniel Burchardt, Robert Garthoff, Kai Redeker, Norbert Ortegel, Markus Rau, and Harald Weinfurter. “Event-Ready Bell Test Using Entangled Atoms Simultaneously Closing Detection and Locality Loopholes.” In: *Phys. Rev. Lett.*



- 119.1 (July 2017). ISSN: 0031-9007, 1079-7114. DOI: [10.1103/PhysRevLett.119.010402](https://doi.org/10.1103/PhysRevLett.119.010402).
- [133] Roman Schmied, Jean-Daniel Bancal, Baptiste Allard, Matteo Fadel, Valerio Scarani, Philipp Treutlein, and Nicolas Sangouard. “Bell correlations in a Bose-Einstein condensate.” In: *Science* 352.6284 (2016), pp. 441–444. ISSN: 0036-8075. DOI: [10.1126/science.aad8665](https://doi.org/10.1126/science.aad8665). eprint: <http://science.sciencemag.org/content/352/6284/441.full.pdf>. URL: <http://science.sciencemag.org/content/352/6284/441>.
- [134] Nils J. Engelsen, Rajiv Krishnakumar, Onur Hosten, and Mark A. Kasevich. “Bell Correlations in Spin-Squeezed States of 500 000 Atoms.” In: *Phys. Rev. Lett.* 118.14 (Apr. 2017). ISSN: 0031-9007, 1079-7114. DOI: [10.1103/PhysRevLett.118.140401](https://doi.org/10.1103/PhysRevLett.118.140401).
- [135] Bernard Yurke and David Stoler. “Bell’s-inequality experiments using independent-particle sources.” In: *Phys. Rev. A* 46 (5 1992), pp. 2229–2234. DOI: [10.1103/PhysRevA.46.2229](https://doi.org/10.1103/PhysRevA.46.2229). URL: <https://link.aps.org/doi/10.1103/PhysRevA.46.2229>.
- [136] F. Laloë and W. J. Mullin. “Interferometry with independent Bose-Einstein condensates: parity as an EPR/Bell quantum variable.” In: *The European Physical Journal B* 70.3 (2009), pp. 377–396. DOI: [10.1140/epjb/e2009-00248-6](https://doi.org/10.1140/epjb/e2009-00248-6).
- [137] E. H. Huntington and T. C. Ralph. “Continuous-variable Bell-type correlations from two bright squeezed beams.” In: *Phys. Rev. A* 65 (1 2001), p. 012306. DOI: [10.1103/PhysRevA.65.012306](https://doi.org/10.1103/PhysRevA.65.012306). URL: <https://link.aps.org/doi/10.1103/PhysRevA.65.012306>.
- [138] Daniel Cavalcanti, Nicolas Brunner, Paul Skrzypczyk, Alejo Salles, and Valerio Scarani. “Large violation of Bell inequalities using both particle and wave measurements.” In: *Phys. Rev. A* 84 (2 2011), p. 022105. DOI: [10.1103/PhysRevA.84.022105](https://doi.org/10.1103/PhysRevA.84.022105). URL: <https://link.aps.org/doi/10.1103/PhysRevA.84.022105>.
- [139] Oliver Thearle et al. “Violation of Bell’s Inequality Using Continuous Variable Measurements.” In: *Phys. Rev. Lett.* 120 (4 2018), p. 040406. DOI: [10.1103/PhysRevLett.120.040406](https://doi.org/10.1103/PhysRevLett.120.040406). URL: <https://link.aps.org/doi/10.1103/PhysRevLett.120.040406>.
- [140] T. Kovachy, P. Asenbaum, C. Overstreet, C. A. Donnelly, S. M. Dickerson, A. Sugarbaker, J. M. Hogan, and M. A. Kasevich. “Quantum superposition at the half-metre scale.” In: *Nature* 528.7583 (Dec. 2015), pp. 530–533. ISSN: 0028-0836. URL: <http://dx.doi.org/10.1038/nature16155>.

- [141] J.R. Johansson, P.D. Nation, and Franco Nori. "QuTiP 2: A Python framework for the dynamics of open quantum systems." In: *Computer Physics Communications* 184.4 (2013), pp. 1234–1240. ISSN: 0010-4655. DOI: <https://doi.org/10.1016/j.cpc.2012.11.019>. URL: <https://www.sciencedirect.com/science/article/pii/S0010465512003955>.
- [142] D.A. Steck. "Rubidium 87 D line data." In: *Tech. report, Los Alamos National Laboratory*, (2001). (revision 2.1.4, 23 December 2010). URL: <http://steck.us/alkalidata/>.

## PUBLICATIONS

---

During the time of the PhD studies I contributed to the following publications, which include some ideas, data and figures shown in this thesis.

- **F. Anders**, A. Idel, P. Feldmann, D. Bondarenko, S. Loriani, K. Lange, J. Peise, M. Gersemann, B. Meyer-Hoppe, S. Abend, N. Gaaloul, C. Schubert, D. Schlippert, L. Santos, E. Rasel, and C. Klempt “Momentum Entanglement for Atom Interferometry.” In: Phys. Rev. Lett.127(14 2021), p.140402. DOI: 10.1103/PhysRevLett.127.140402. URL: <https://link.aps.org/doi/10.1103/PhysRevLett.127.140402>.
- Bernd Meyer, Alexander Idel, **Fabian Anders**, Jan Peise and Carsten Klempt “Dynamical low-noise microwave source for cold atom experiments” DOI: 10.48550/arxiv.2003.10989. URL: <https://arxiv.org/abs/2003.10989>.
- **Fabian Anders**, Luca Pezzè, Augusto Smerzi, and Carsten Klempt. “Phase magnification by two-axis countertwisting for detection-noise robust interferometry.” In: Phys. Rev. A97(4 2018), p.043813. DOI: 10.1103/PhysRevA.97.043813. URL: <https://link.aps.org/doi/10.1103/PhysRevA.97.043813>.
- **Fabian Anders** “Magnification of the interferometric phase for noise-robust quantum metrology” Master Thesis (2017)



## ACKNOWLEDGMENTS

---

Großen Dank an Carsten Klempt. Seine hervorragende Vorlesung zur Quantenoptik hat mich für dieses Feld der Physik begeistert und während der letzten Jahre als Masterand und Doktorand konnte ich viel von Ihm lernen. Danke, dass ich die Möglichkeit bekommen habe, mit verschränkten BECs zu spielen. Danke für das entgegengebrachte Vertrauen und ganz besonders für die familienfreundlichen Arbeitsbedingungen.

Vielen Dank an Ernst Rasel für die erfolgreiche Kooperation, und ihm, Augusto Smerzi und Luis Santos herzlichen dank für die Begutachtung meiner Arbeit und die Übernahme des Prüfungsvorsitzes. Vielen Dank auch an Fritz Schulze Wischeler für die freundliche Unterstützung im Rahmen des HSN Doktorandenprogramms (insbesondere auch für den Kaffee und die Kekse).

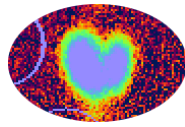
Ganz besonderen Dank an Bernd Meyer-Hoppe für den frischen Wind, den awesome g gauge, die Akzeptanz meiner Launen und seine unermüdliche Tatkraft. Es hätte ruhig mehr Edelbräu geben können! Ebenso sei Christophe Cassens gedankt für seine Unterstützung beim Ausblick dieser Arbeit und die Zählung des Experimentes als Bernd und ich am Schreibtisch waren. Mögen euch die Schweinegeister wohl gesonnen sein!

Vielen Dank an Polina Feldmann, Dmytro Bondarenko und Sina Loriani für die geduldige Unterstützung mit theoretischen Analysen der experimentellen Herausforderungen.

Auch allen anderen direkten und indirekten Kollegen und Mitstreitern sei herzlichst gedankt, insbesondere: Bernd Lücke, Jan Peise, Karsten Lange, Alexander Idel, Mareike Hetzel, Martin Quensen, Cebrail Pür, Jiao Geng, Andreas Hüper, Ilka Kruse, Jens Kruse, Mathias Gersemann, Sven Abend, Christian Schubert und Henning Albers (insbesondere für die Schokoquelle).

Herzlichen Dank an Birgit Ohlendorf für die fantastische Organisation und die aufmunternden Worte in der heißen Schreibphase. Für die generell reibungslose Organisation und freundlichen Worte vielen Dank an Gunhild Faber, Madeleine-Yasmin Miltsch und Stephanie Kaisik und allen weiteren an der Infrastruktur des Institutes Beteiligten.

Meinen Nachbarn Hermann und Franziska gebührt ein herzlicher Dank für das Büro und Manfred für den leckeren Kaffee. Meiner Partnerin Julia und meiner Tochter Mira danke ich für Liebe, Geduld und gutes Essen.



## DECLARATION

---

Hiermit versichere ich, diese Arbeit selbstständig verfasst und keine weiteren als die angegebenen Hilfsmittel und Quellen verwendet zu haben. Alle Stellen dieser Arbeit, die wörtlich oder sinngemäß aus diesen Quellen übernommen wurden, sind als solche kenntlich gemacht. Die Arbeit wurde noch keiner anderen Prüfungsbehörde vorgelegt.

*Hannover, 2022*

---

Fabian Anders





## CURRICULUM VITAE

---

### PERSONAL INFORMATION

Name	Fabian Anders
Date and place of birth	25.07.1989 Magdeburg (German Democratic Republic)

### EDUCATION

2017-2022	PhD student – Institut für Quantenoptik and Hannover School for Nanotechnology – Leibniz Universität Hannover (Germany)
2014-2017	Master of Science (Physics) – Leibniz Universität Hannover (Germany)
2015	term abroad – Chalmers tekniska högskola, Göteborg (Sweden)
2011-2014	Bachelor of Science (Physics) – Leibniz Universität Hannover (Germany)
2010-2011	undergraduate studies (Industrial Engineering) – Fachhochschule Hannover (Germany)
2000-2009	Abitur – Gymnasium Porta Westfalica (Germany)